PUBLIC HEALTH INFORMATICS - STRATEGY AND DECISION MODELING

A Dissertation
Presented to
The Academic Faculty

by

Haozheng Tian

In Partial Fulfillment
of the Requirements for the Degree
Doctor of Philosophy in Bioinformatics in the
School of Biological Sciences

Georgia Institute of Technology
December 2019

PUBLIC HEALTH INFORMATICS - STRATEGY AND DECISION MODELING

Approved by:

Dr. Eva K. Lee, Advisor
H. Milton Stewart School of Industrial and Systems Engineering
Georgia Institute of Technology

Dr. Jung H. Choi
School of Biological Science
Georgia Institute of Technology

Dr. King Jordan
School of Biological Science
Georgia Institute of Technology

Dr. Concettina Guerra
College of Computing
Georgia Institute of Technology

Dr. John F. McDonald
School of Biological Science
Georgia Institute of Technology

Dr. Peng Qiu
Department of Biomedical Engineering
Georgia Institute of Technology

Date Approved: August 8th, 2019

To My Parents, Yunpeng Tian and Xiaoqi Tan,

Love you.

ACKNOWLEDGEMENTS

It has been a long, tough, challenging, yet fruitful, adventurous and exciting journey. First and foremost, I would like to give my deepest gratitude to my advisor Dr. Eva Lee for the opportunity, guidance, encouragement and achievement. With the support of Dr. Lee, I have had the opportunity to expose myself to various topics of research and really pushed my limit beyond what I was capable of.

I want to express my sincere gratitude to Professor King Jordan, who is one of the first professors that I met in the initiation of my master's study. Professor Jordan opened up the gate of bioinformatics for me with his unique way of conveying concepts and knowledge. Through the hands-on experience and discussion of his class, I acquired more knowledge than I could imagine. As a humorous and knowledgeable professor, Professor Jordan is always able to guide us through confusions and also hopes for the best for all the students. I also want to give my gratitude to Professor Jung Choi. Professor Choi is also one of the first professors that I met when I first came. Professor Choi has been very considerate and kind to us all and helped me in a successful adaption to the graduate study. By taking the class of Professor Choi, I learnt many of the fundamental concepts, algorithms and techniques of bioinformatics.

I also want to thank Professor John McDonald and Professor Peng Qiu for joining my thesis committee. Throughout my whole PhD study, I have admired the dedication, devotion and contributions of yours in scientific research. I want to thank Professor Concettina Guerra. The class that I have taken with her was fun and inspiring, which prepared me for my future research with solid background. Being the TA for Professor

Guerra is also an unforgettable experience, in which I truly enjoyed helping younger students and was deeply touched by the devotion and consideration of Profess Guerra for the students.

Finally, I want to thank my dad and mom for the unconditional support along the way. The deepest love for you beyond words.

TABLE OF CONTENTS

LIST OF TABLES

LIST OF FIGURES

LIST OF SYMBOLS AND ABBREVIATIONS

A* PS	A* with post-smoothed paths
ABM	Agent-based model
ABS	Agent-based simulation
AP Theta*	Angle-Propagation Theta*
CC	WHO Collaborating Center
CNN	Convolutional neural network
CPG	Clinical practice guidelines
DES	Discrete-event simulation
EBM	Equation-based model
EMR	Electronic medical record
GIS	Graphic information system
GISN	Global Influenza Surveillance Network
HA	Hemagglutinin
HI	Hemagglutinin inhibition
MDS	Multi-dimensional scaling
NA	Neuraminidase
NIC	National Influenza Centers
POI	Point of interest
PSO	Particle swarm optimization
SD	System dynamics
WHO	World Health Organization

SUMMARY

We are constantly facing newly emerged challenges in the protection of public health and safety. The challenges may come from the increasingly complicated social activities, the conflict of higher demand of medical care and limitation of medical resources and technology, and the severity of diseases. We should not only aim to solve problems of large size, but also should be able to provide solutions in a fast and even real-time manner. Given the circumstance, it is necessary to develop decision support and analytical systems that are flexible, scalable and interpretable.

Computer models and computational methods are utilized extensively in many areas of systems management. They are particularly useful in providing insight into the operation of a system and predicting the outcome given a change of strategy. The advantages of such approaches become more obvious with increasingly large scale of problem, complex interactions and heterogenicity of participating entities. Computational approaches have been widely used in decision support, mathematical modeling, system dynamics and simulation modeling. Specifically, the technique of simulation has been considered appropriate for performance evaluation and strategy validation of logistics systems [1, 2]. Though, discrete-event simulation has been the most widely used modeling technique of logistics and health care systems for more than 40 years [3, 4], agent-based simulation has been gaining attention with innovations and advantages that are highly applicable to operation research. Agent-based simulation can explicitly model the complexity arising from the diversity of population and multi-level interactions. In my PhD dissertation research, novel and efficient algorithms are proposed for improvement of

agent-based models, including advances in pathfinding, collision avoidance, emotional modeling and optimization.

Practice guidelines regarding pain management for surgical and non-surgical purposes are being constantly updated and systematically reviewed as warranted by the advances of knowledge, practice and technology. Obstetric anesthesia has become the standard procedure in the medical care of parturient women and numerous improvements have been proposed to achieve better outcome. Nonetheless, limited researches thoroughly examined the efficacy of the catheter-based epidural anesthesia technique versus the innovative needle-based approach. Additionally, with current recommendation of procedures, there is still a lot of practice variance of anesthesiologists, which requires further investigation to reveal the impact on outcome and side effects.

Faster than average mutation rate [5-7] and genome reassortment [8-11] are the two major mechanisms that enable influenza A virus for cross species transmission and pandemics. Seasonal influenza is an acute viral infection and is estimated to cause 3 to 5 million cases of severe illness and around 250,000 to 500,000 deaths worldwide [12]. Vaccination is the most effective way to prevent the outbreak of epidemics. To produce a qualified vaccine, the composition virus is proposed and examined for similarity to the circulating strains of the upcoming pandemic season. The rapid evolution of influenza virus poses a severe challenge for successful medical care [13]. Therefore, it is usually necessary to conduct the evaluation annually to ensure the capture of antigenic variation and optimal protection of the public. The “gold standard” for evaluating the efficacy of vaccine and characterization of virus strains is the hemagglutination inhibition assay (HI assay) [14, 15]. However, the process of conducting HI assay is labor and economic intensive. Hence,

a wide range of sequence-based methods have been proposed to infer the antigenicity of influenza virus [16-21]. The development of *in silico* modeling of influenza antigenicity provides a cost-effective and fast approach in the annual analysis. A better modeling will improve the quality of vaccine recommendation and thus result in better protection of public health.

The algorithms, analysis and methodologies proposed in this PhD dissertation provide improvement of existing tools and novel solutions for the above-mentioned topics. The specific contributions of this dissertation are summarized as follows:

Research advance 1: A multi-purpose computational platform for crowd control and public safety. The development of such a system is composed of a) an improved pathfinding algorithm (Flood Theta* pathfinding algorithm) that eliminates the artificial effect of 45-degree course in a grid environment, b) a novel collision avoidance algorithm with realistic behavior modeling, c) emotion modeling, propagation and behavior integration, d) optimization component integrated with the simulation platform.

Research advance 2: Understand practice variance and factors influencing obstetric epidural anesthesia outcome. The systemic study of the obstetric epidural anesthesia investigates has the following parts: a) investigate the safety and efficacy of a large-dose, needle-based epidural technique in obstetric anesthesia, b) prediction of the incidence of hypotension and outcome using machine learning framework, c) quantification of practice variance and medicine usage that affects outcome.

Research advance 3: Antigenicity prediction and vaccine recommendation of human influenza virus A/H3N2. First, the systematic analysis of the feasibility of using

AAindex as the feature is conducted, followed by a heuristic search to find the best combinations for predictive model. Second, based on the nature of the feature space of the task, it is hypothesized that convolutional neural network is able to extract and summarize the non-linear and spatial relationship between distant amino acids along the protein sequence and thus provide good prediction accuracy. Third, particle swarm optimization (PSO) algorithm is applied to optimize the hyperparameters of the convolutional neural network, which produces superior result compared to hand crafted neural networks.

CHAPTER 1 INTRODUCTION

This chapter provides an introduction of the knowledge, technology, concepts, practice and research advances that are related to the three studies in this dissertation. Later, the chapter is concluded with brief summaries of the contributions achieved in the research work.

1.1 Agent Based Simulation

1.1.1 Overview of Agent-Based Simulation

Agent-based simulation (ABS) is an approach to model systems that are composed of actions and interactions of autonomous agents, with visualization and statistics to assess the effect on the system as a whole. ABS systems make it possible to implement an environment with specific features, explore and forecast the future scenarios, assess the efficacy of alternative strategies, and measure the changes in outcome given various decision variables. ABS has been widely used in the study of biology [22, 23], ecology [24], finance [25], operation research [26], emergency management [27, 28] and social behaviors [29]. At an aggregated level, it is advantageous to use ABS to understand the general pattern and properties of the underlining scenario, which is not easy to be deduced or calculated by simply observing the individual agent, due to the complexity introduced by the interactions in the system.

Agent-based modeling (ABM) and equation-based modeling (EBM) take fundamentally disparate perspectives when modeling a system, which can be characterized as bottom-up (ABM) versus top-down (EBM). Compared to ABM, EBM has a longer

history of application in social science [30] and epidemiology [31]. However, the advantage of ABM resides in the capability of modeling heterogeneity both in individual and network of interaction, while EBM assumes perfect mixing and homogeneity [32]. Additionally, ABM is most naturally applied to systems that are characterized by a high degree of localization and dominated by discrete decisions. EBM is most appropriate for systems that can be modeled centrally, in which the dynamics and interactions are formulated by physical laws rather than individual decision making [33]. A typical application of EBM is SIR model [34, 35] and its variants (SI, SIC, SIS, SEI, SEIR, SEIQS, SEIQV) [36-41] in modeling the spread of infectious disease, where the agents (virus) are usually considered homogeneous.

There has been a large collection of simulation techniques, including discrete-event simulation (DES) [42], system dynamics (SD) [43, 44], Monte Carlo simulation [45], continuous simulation [46] and combined DES/continuous simulation [47]. Specifically, DES has been the main stream modeling approach in the operation research community for over 40 years [4]. However, ABS has gaining attention and the research community has used ABS more often than DES in the last decade [48]. While DES is more applicable in scenarios that consist of queuing simulations, or complex network of queues, ABS allows researchers to model real-world systems in ways that is either not possible or not preferable using traditional modeling approach such as DES or SD. Specifically, ABS is suitable for problems that have features such as 1) agents have dynamic relationships with each other, 2) the goal is to model the collective behavior of individual agents, 3) agents have behaviors that interact with the space, 4) agents engage in strategic decision, adaption and learning, 5) cooperation, colluding and forming organizations are expected from the agents, 6)

agents are heterogeneous in terms of characteristics, 6) complicated status such as emotions are necessary in the modeling, 7) scalability or extensibility is important.

1.1.2 Components in An Agent-Based Simulation Model

An agent-based model usually has three major components that are pre-defined before implementation:

1) The agent, its attribute and behaviors.
2) The relationships and definitions of interaction.
3) The environment.

Subsequently, a computational engine is needed to simulate the behavior and interaction of agents. The computational engine also regulates the dissemination of information, emotion and resolve collision of paths.

Though, there is no universal definition of what an agent is, it is commonly agreed that an agent represent a type of independent component, which execute behaviors ranging from primitive reactive responses to intelligent decision making. An example agent with its properties and interactions is shown in Figure 1.1.

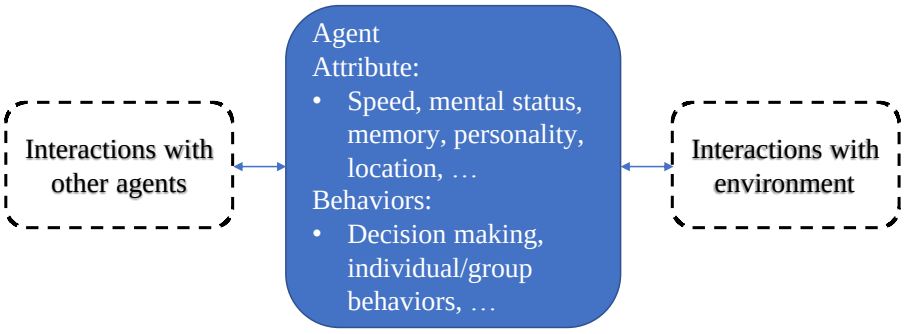

Figure 1.1 – An agent in agent-based simulation models.

In ABS, an agent can represent various entities, including a person, a vehicle, a software, and even a system. An agent is usually considered to have the characteristics as follows:

1) Identity. An agent is required to be identified as an individual, which contains a set of properties and decision-making capability. This requirement implies that there is a clear boundary of each agent, and it is easy to determine if an element is part of the agent or the system.
2) Autonomy. The decision making and behavior execution of an agent is based on the independent processing of information and a reflection of the individual's properties and characteristics.
3) Objective. An agent is goal-oriented, and its collective behavior should result in closing in or achieving its objective.
4) Adaptation. An agent is able to modify and adapt its behavior over time based on experience or memory.

The environment in which the agents live can be either spatial or relational [49]. The spatial environment refers to the physical locations where the agent resides in. The common approach to model spatial environment includes grid, lattice, continuous space and graphic information system (GIS). The relational environment refers to the connections of agents, including social interactions, communication network, and emotional propagation network.

The implementation of the environment is one of the fundamental factors that affect the behavior and interaction of agents. The conventional way to construct a grid of cellular

automata is to place cells of the same size along the two or three-dimensional space. The model with a grid space, such as cellular automata, assumes the schema of one agent per cell. The schema is extremely convenient in representing real-life situations, which captures the overall path of movement and is not hard for resolving collision. People also proposed models with finer grids in which one agent occupies multiple cells to model smoother movement and various speed of pedestrians [50, 51]. Continuous space models that eliminate the artificial effects inherited with grid space models use even finer grids achieve a more realistic representation of the details of pedestrian interaction [52, 53]. However, the improvement in resolution limits its use in large scale representation of ensemble of multiple simulations, given the significantly increased computational burden.

1.2 Obstetric Epidural Anesthesia

Epidural anesthesia is a way to deliver anesthetics to the lumbar area so that it reduces the functionality of spinal nerve and stops the pain signal from reaching the brain. The procedure is widely applied in parturient women. 61% of women who had a singleton birth in a vaginal delivery in the 27 states of the US in 2008 received epidural or spinal anesthesia [54]. The procedure involves the injection of a certain amount of anesthetic into the epidural space of laboring women (Figure 1.2). Epidural space surrounds the spinal cord and is filled with fluid. The medicine in the epidural space penetrates the epidural membrane and adjusts the functionality of the spinal nerves.

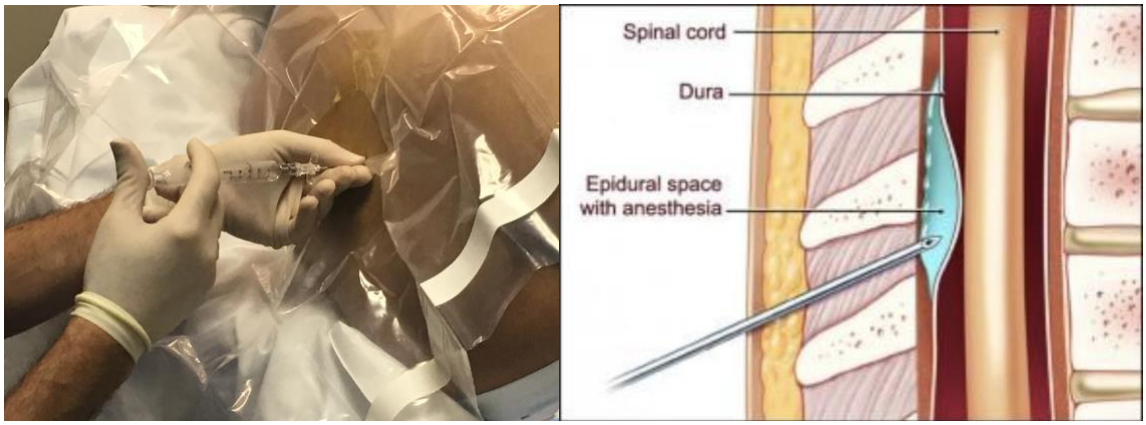

Figure 1.2 – Practice of epidural anesthesia.

If the injection of medicine works properly, the patient loses her sense of pain in the lower part of the body. During the procedure of epidural anesthesia, a catheter is installed, which connects to the epidural space. The catheter is pushed through the needle until a certain length of it is in the epidural space. The catheter is connected to a pump and utilized by administering additional medicine through it when there is a lack of effect of the previous dosage. The patient also uses it throughout the whole delivery procedure when she feels in need of pain relief.

Epidural anesthesia and the choices of medication could lead to side effects depending on the characteristics of patients and anesthesiologists' operation. The most common side effect is hypotension, primarily caused by blockade of the sympathetic nervous system leading to arterial and venous vasodilation [55]. Opioids may cause pruritus depending on the dosage, while epidural opioids have a less occurrence rate than intrathecal opioids [56]. Puncture of the epidural space during injection can lead to side effects such as headache, and usually require immediate treatment [57]. Additionally, dura puncture can cause the leaking of spinal fluid, which results in severe headaches for days.

Though, conflicting evidence [58, 59] is found regarding whether epidural anesthesia affects breastfeeding, a randomized study involving 1054 nulliaparae concludes that epidural fentanyl is not likely to affect breastfeeding initiation [60]. The administering of medicine via epidural needle may cause intravascular injections. Such inadvertent event may result in a wide range of side effects: dizziness, disorientation, muscle twitching, unconsciousness, and even coma [57]. The procedure of injection is inherited with risk of damaging vessels and thus could result in hematoma. However, the instance rate of epidural hematoma is reported to be less than 1 in 150,000 patients [61].

Currently, American Society of Anesthesiologists[62] and American College of Obstetricians and Gynecologists [63] are known to publish practice guideline for epidural anesthesia. The practice guideline that is updated with the evolution of knowledge, practice and technology serves as an efficient approach of medical care improvement. This dissertation is intended to supplement the practice guideline with the analysis on the needle-based epidural technique using a data-driven and machine learning approach.

1.3 Influenza Vaccine Recommendation

Seasonal Influenza is an acute viral infection and is estimated to cause 3 to 5 million cases of severe illness and around 250,000 to 500,000 deaths worldwide [12]. Influenza viruses are divided into three genera: A, B and C. Influenza A and B viruses are known to cause severe respiratory infections in human, while influenza C viruses only causes mild symptoms and are less common in circulation [64]. Vaccination is the most effective way to prevent Influenza outbreaks and epidemics. The widely used trivalent influenza vaccine contains three strains which represent one from A/H1N1, one from A/H3N2, and one from

B. Since 1970s, two antigenically distinct virus lineages of influenza B (Yamagata and Victoria) have emerged [65]. The difficulty in the prediction of the circulating strain from the two lineages of influenza B reinforced the development of quadrivalent influenza vaccines, which cover both lineages [66].

Due to the constant and rapid change of circulating influenza viruses, vaccine strains are being updated annually for both northern and southern hemispheres in order to be representative of the antigenicity of circulating virus strains. Antigenic drift is known as the mechanism of rapid evolution of influenza viruses [67]. The process of antigenic drift involves the accumulation of point mutations on the antibody binding sites in the HA (hemagglutinin) and NA (neuraminidase) proteins, which help the virus to evade the detection of human immunity [68, 69]. Genetic reassortment is an additional mechanism that introduces more mutations to influenza virus, especially for A/H3N2 [70]. Seventy percent of A/H3N2 strains isolated in 1998-1999 were characterized with completely different genome composition, while frequent reassortment in NA, PB1, PB2 and NP genes are also observed [71]. Genetic reassortment (antigenic shift) is also possible between co-infecting influenza A subtypes from multiple species, a process that has the potential to create new strains capable of cross-species and inter-human transmission [72].

Currently, World Health Organization (WHO) is coordinating the combat against influenza pandemic through a global collaboration network (Global Influenza Surveillance Network – GISN) of surveillance, response, clinical study and vaccine recommendation. To date GISN comprises 143 National Influenza Centers (NICs), 6 WHO Collaborating Centers (CC), 4 Essential Regulatory Laboratories and 13 WHO H5 reference laboratories. More than 500,000 respiratory specimens are screened at these NICs annually, of which

approximately 8,000 are then sent to regional CCs for more extensive genetic and antigenic characterization [73]. The characterization of antigenicity is primarily done through hemagglutinin inhibition (HI) assays using post-infection ferret antisera, and human serologic analyses using pre and postvaccination serum samples. Strain sequence analysis, prevalence rate, and geographic distribution of variants are also determinant factors in vaccine recommendation [74]. WHO holds meetings twice a year before the start of the winter seasons for the northern (February) and southern (September) hemispheres and makes decision for the annual vaccine recommendation. Despite the global endeavor, a poor match of between the vaccine strain and circulating variants still lead to vaccine failure. For example, in the 2014-2015 flu season, vaccine failure is found to have an effective rate of 19% in the US (10% for 2004-2005) [75]. The difficulty in effective vaccine recommendation resides in three folds, 1) The time gap of at least six months between vaccine recommendation and large-scale distribution introduces extra difficulty to capture the characteristics of the rapid mutations in the viruses, 2) multiple circulating strains carrying different components makes it hard for one vaccine strain to be effective in a general manner, 3) antigenic characterization using ferret antisera may lead to different conclusions compared with using human antisera.

1.4 Convolutional Neural Network

Convolutional neural network (CNN) is a class of deep neural network models, primarily applied in the analysis of visual information. Similar to artificial neural networks, CNN are also inspired by biological processes [76]. Despite variations in structure, CNN is usually composed of stacked modules that include convolution layers (convolution and

pooling) and single or multiple fully-connected layers. Eventually, the structure is connected to an output layer which outputs the class label.

The convolutional layer extracts the features from input images by applying convolution to the pixels with multiplication of the kernel in the layer. This is followed by sending the result through a nonlinear activation function. The results are regarded as the representations of the input image. There are usually multiple kernels in a convolutional layer, whereas one kernel is dedicated to learning one specific feature of the image. Formally, the ith output of the kernel can be written as:

$$Y_i = f(W_i \cdot x) \tag{1.1}$$

where Y_i represents the output, W_i is the weights of the ith kernel and x is the input image. The result is the dot product of the weights of kernel and the image, followed by processing using the non-linear activation function $f(\cdot)$. The choices of activation functions include sigmoid, hyperbolic tangent. Recently, researchers have shifted the focus to rectified linear unit (ReLU) [77], observing improved performance of the neural network. Variants of ReLU includes leaky rectified linear unit (Leaky ReLU), parametric rectified linear unit (PReLU) and randomized leaky rectified linear units (RReLU). Experiments suggest that incorporating a non-zero slope for negative section in ReLU could consistently improve performances [78].

Pooling layer is added in order to reduce the resolution of information and thus achieve invariance to image distortion [79]. Specifically, average pooling layer calculate the average of all input values and sent it to the next layer, whereas max pooling layer uses

the maximum value. Empirical result suggests that a mixture of average and max pooling outperforms average pooling and max pooling, while max pooling is marginally superior to average pooling [80].

CNN is widely applied in image processing, including facial recognition, denoising, image compression. Variants of CNN also expand its application in text processing, such as recurrent CNN [81] and generative neural network, such as variational autoencoder [82]. To our best knowledge, the research described in Chapter 4 is the first to apply CNN in the prediction of influenza antigenicity and vaccine recommendation.

1.5 Overview of the Thesis Dissertation

1.5.1 Chapter 2

This chapter presents the multi-purpose agent-based simulation platform for crowd control. This study is a collaborative work with Georgia Aquarium, Georgia Tech police and emergence response team and Georgia Tech student athletic center with the aim to understand the people flow, operational logistics and emergency situations in public venues, and to understand of the capacity and bottleneck of operations in a facility. The deliverable of the study is to develop a decision support system (agent-based simulation platform) that ensures service is delivered with maximum efficiency and the highest satisfaction.

This chapter introduces five major innovations of the simulation platform. First, Flood Theta* algorithm is proposed as a solution of the problem of 45-degree effect of movement in a grid environment and is proved with improved performance compared to Basic Theta* algorithm. Second, a Projection Based Interactive Velocity Avoidance Model

is described, which models human-like avoidance behavior in the situation of navigating through incoming traffic or obstacles. Third, the system is equipped with the flexibility for various situation designing, multilevel simulation capability, accurate descriptor of the time-flow relationship of pedestrians, global control of pedestrians' decision-making process. Forth, emotional model is introduced with emotion propagation and crowd behavior adjustment. Fifth, an optimization component is integrated with the platform that allows optimizing the distribution of pedestrian flow and minimizing total congestion and operation time.

1.5.2 Chapter 3

This chapter investigate and discuss the significant factors that affect the efficacy of the obstetric epidural anesthesia. This study is in collaboration with the Northside Hospital of Atlanta which delivers the largest number of babies annually in the US. The contributions of this work are three folds. First, using a data-driven informatics approach, the study investigates the safety and efficacy of a large-dose, needle-based epidural technique in the administering of obstetric anesthetics. Second, machine learning framework is used in the prediction of the incidence of hypotension and outcome of treatment. Key factors that are significant in a successful delivery of medical care are identified. Third, this study provides quantification of practice variance and medicine usage. The conclusions drawn from the analysis assist in the development of better clinical practice guideline and provide insight on tackling the abuse of pain medicine.

1.5.3 Chapter 4

This chapter aims at providing an accurate and efficient *in silico* approach for modelling antigenicity change of human influenza virus A and vaccine strain recommendation. First, systematic analysis is performed on the feasibility of using AAindex as the feature, from which the best metrics are found using a heuristic search for the predictive model. Second, with the feature matrix built up using AAindex, it is hypothesized that convolutional neural network is able to extract and summarize the non-linear and spatial relationship between amino acids that are distant on the protein sequence and thus provide good prediction accuracy. Third, particle swarm optimization algorithm is applied to optimize the hyperparameters of the convolutional neural network, which produces superior result compared to hand crafted neural networks.

1.5.4 Chapter 5

This chapter is the conclusion of the thesis, in which the current work is summarized, and the research of the future is discussed.

CHAPTER 2 A MULTI-PURPOSE COMPUTATIONAL PLATFORM FOR CROWD CONTROL AND PUBLIC SAFETY

2.1 Abstract

2.1.1 Objective

To address the need of understanding the flow of people in large event, operational logistics and emergent situations, we developed the Crow Control Planning Platform. The operators of a facility that provides service to a large group of attendants require the understanding of capacity and bottleneck of operation, such that the service is delivered with maximum efficiency and the highest satisfaction. Agent based simulation is an approach that can model the heterogeneity and complexity of a large crowd. In order to realistically model the group behavior, we develop a series of algorithms regarding path finding, collision avoidance and emotional modeling. Overall, the platform provides the capability of large scale, realistic, fast and flexible simulation execution.

2.1.2 Method

We provide a new implementation of path finding algorithm which integrates Basic Theta* with Flood Algorithm and solves the problem of 45-degree effect of movement in a grid environment. The elimination of such artificial effect drives Agent Based system on grid coordinates one step further toward realistic simulation. Second, we propose a new collision avoidance algorithm. The algorithm implements avoidance behavior in an interactive manner, which mimics the phenomena that people react to other people's avoidance behavior and adapt their own accordingly. The algorithm successfully solves

several drawbacks of social force model, being able to resolve complicated collision avoidance situations smoothly with low computational cost. Third, the system is equipped with the flexibility for various situation designing, multilevel simulation capability, accurate descriptor of the time-flow relationship of pedestrians, global control of pedestrians' decision-making process. Forth, emotional modeling is incorporated with the decision making and behavior planning of the agent, with which emotion propagation and crowd behavior could be realistic modeled.

2.1.3 Result

Our system was applied on several event planning cases including Georgia Aquarium daily operation simulation, Bobby Dodd stadium game day operation, Atlanta Marta station evacuation, operation of San Ysidro port, etc. While bottlenecks were identified with simulations, strategic improvement and recommendation were made for each case computed using the built-in optimization component. Our simulation revealed that after implementing the recommendations for both Aquarium and Football stadium, the density of people inside the structure decrease significantly over the course of operation, thus proving that the tourists had better than usual experience.

2.2 Introduction

Computational method is becoming an increasingly important aspect of modern scientific research. Computational method is advantageous in problems where 1) the analytical solution is too hard to obtain, 2) approximation of theoretical result is not reliable, 3) it is necessary to validate the result via another approach, and 4) experiment is not feasible [83]. The method is primarily composed of two major areas of applications: 1)

ordinary or partial differential equation [84] and 2) computational representation of systems, such as agent-based models (ABM) [85, 86]. Advances in computational capacity have allowed the application of agent-based simulation in various disciplines such as biology [87], operation research [88], finance [25], emergency management [27, 28] and social behaviors [29]. Compared to ABM, equation-based modeling (EBM) has a longer history of application in social science [30] and epidemiology [31]. However, the advantage of ABM resides in the capability of modeling heterogeneity both in individual and network of interaction, while EBM assumes perfect mixing and homogeneity [32]. EBM is most appropriate for systems that can be modeled centrally, in which the dynamics and interactions are formulated by physical laws rather than individual decision making [33]. However, ABM is most naturally applied to systems that are characterized by a high degree of localization and dominated by discrete decisions. Specifically, ABM is suitable for problems that have features such as 1) agents have dynamic relationships with each other, 2) the goal is to model the collective behavior of individual agents, 3) agents have behaviors that interact with the space, 4) agents engage in strategic decision, adaption and learning, 5) cooperation, colluding and forming organizations are expected from the agents, 6) agents are heterogeneous in terms of characteristics, 6) complicated status such as emotions are necessary in the modeling, 7) scalability or extensibility is important.

Agent-based simulation platforms can be distinguished by the implementation of the field of movement and collision avoidance approach. Cellular automata model is characterized by discretizing the movement field into 40cm by 40cm grids, which represents the size of a person and adopts the one person per cell schema [89]. The one person per grid schema provides convenience in using the grid to define the movement of

agent through space and solving collision avoidance. Models with finer grids are also proposed to model smooth movement and various speed of pedestrians [50, 51]. Continuous space models use even finer grid with the potential to achieve finer geometric resolution and a more realistic representation of the details of pedestrian interaction than the grid-based approach described above [52, 53]. However, the improvement in resolution comes with an obvious disadvantage of significantly increased computational cost, which can limit its use in large scale representation or ensemble of multiple simulations.

Motion planning for multiple agents is a challenging problem in the simulation of virtual environment. Usually, motion planning in agent-based simulation integrates optimal path finding, collision avoidance, emotion and behavior modeling and objective optimization. Generally, pathfinding goes beyond a single-agent pathfinding problem on a fully observed map, which includes situations like multiagent pathfinding search, adversarial pathfinding, dynamic changes in the environment, heterogeneous terrain, mobile units, and incomplete information [90]. A* [91] is the best known algorithm for games and simulations and many improvement and variants are inspired by it [92-94]. Hierarchical pathfinding algorithm [95] is proposed to overcome the drawbacks of grid based algorithms, of which the consumptions of memory and search space increase when scaling up. However, hierarchical algorithms only find suboptimal paths. Algorithm such as jump points algorithm [94] that is specific for grid topology is proposed with no memory overhead and guarantees optimal result. Algorithms like A* and its variants could not find the optimal grids path, since their paths are artificially constrained to multiplies of 45 degrees. In a grid simulated environment, it is a common practice to implement a potential field, which is used to guide the pedestrian to find the destination by descending through

the field [96]. Three implementations of flood algorithm that generates the potential field are introduced by P. Stucki [97], in which the algorithm expands a cell with a certain value if it is not an obstacle. Flood algorithm is efficient in computing, but the path is also constrained with the 45-degree phenomena. The urgent need of generating paths that resemble real human's choice inspired the development of any-angle path-planning algorithms [98-100]. A* with post-smoothed paths (A* PS) [101] smooths the paths generated by A*, which often shortens the total length at an increased computational cost. Field D* (FD*) [99] is the an variant of A* that achieve any-angle path generation by linear interpolation. Basic Theta* [98] generate paths that are slightly longer than the optimal path with similar computational cost to A*. A variant of it, Angle-Propagation Theta* (AP Theta*) [98], improves worst case computational complexity by maintaining an incremental angle range prior to vertex expansion. But the mechanism makes it more complex and less superior in overall computation time and path length, compared to Basic Theta*. Incremental Phi* [102], an incremental version of Basic Theta*, speeds up the path planning significantly with the mechanism of free space assumption and angle range, but produces slightly longer paths. A comparison study [100] reveals that Basic Theta* finds shorter paths at lower computational cost on various level of random obstacles, compared to A* PS, FD* and AP Theta*. However, the state-of-art Basic Theta* fails at producing the optimal path given certain obstacles placement in the terrain and is only a single-agent path planning algorithm, which hinders its application in large scale agent-based simulation.

Collision avoidance for multiple moving agents is the key component of an agent-based simulation system. Social force model [103-105] adopts the concept of physical laws

of force and speed, where the agent is treated as an object and the repulsive forces introduced by neighboring agents and obstacles shapes its trajectory. The motion of an agent is the combinatorial effect of forces that provide thrust, stopping and steering. Static or dynamic obstacle avoidance is achieved by the repelling forces between the obstacle and the agent, which decrease proportionally to the distance between the two. Though, social force model is intuitively easy to understand, the inherited problems are oscillation, unnatural steering behavior and not being able to move along obstacles. A study [106] showed that social force model could not resolve situations such as antipodal, bidirectional opposed movement and thus results in failure of representation of human behavior. Predictive and cooperative models for pedestrians are pro-active model in which the agents actively interact and predict potential collision [107-110]. Synthetic vision based collision avoidance is the state of the art as it mimics the avoidance behavior guided by human vision [106, 111]. Long range collision avoidance is a model that optimize the resolution of avoidance behavior according to distance [112]. Other collision avoidance approaches are proposed, including vector-field histogram [113, 114], and velocity obstacle and its variants [107, 115-122]. Compared to other algorithms, the simple assumptions of social force model make it efficient in large-scale computation and thus suited for simulation of large crowd. One of our motivations is to propose a collision avoidance model based on social force methodology and achieve realistic simulation that is limited in the original social force model.

Our contributions of in this study includes: 1) the Flood Theta* path planning algorithm that achieve better performance compared to Basic Theta* algorithm with the extension of multi-agent path planning; 2) the collision avoidance model, Projection Based

Interactive Velocity Avoidance Model, that realistically simulates human avoidance behavior at similar computational cost of social force model; 3) integration of simulation with emotional modeling, propagation and individual behavior adjustment; 4) a decision support framework that provides optimization of flow of pedestrian based on operation time approximation by neural network, aimed at minimization of total operation/evacuation time; 5) an agent-based simulation platform that integrates the above-mentioned components, which is suited for large event simulation and emergence evacuation (Figure 2.1).

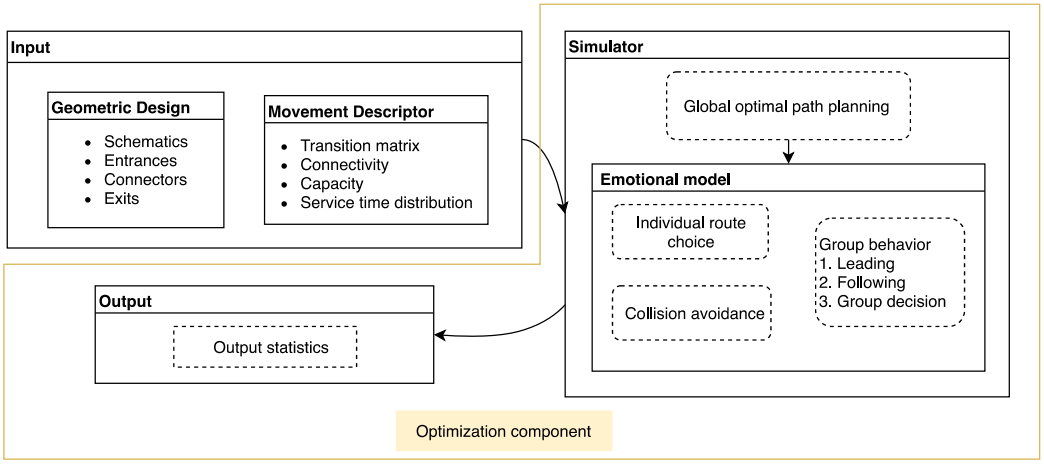

Figure 2.1 – Framework of the agent-based simulation platform.

2.3 Flood Theta* Algorithm

Flood Theta* algorithm is the integration of Flood algorithm and Basic Theta* and thus the algorithm is capable of any-angle path planning for multiple agents. Flood algorithm is used to create the potential field in a grid environment, which guides the agent to its destination. The potential field is created by assigning values to cells starting from

the destination, representing the distance from the cell to it with the consideration of all obstacles that the agents need to avoid. The potential field is generated before the simulation takes place and serves as a mechanism for global path planning. Multiple potential fields are needed if there are several destinations.

2.3.1 Flood Algorithm

In a regular grid environment (the shape of cells is square), the algorithm initiates the calculation from the destination by assigning the distance value to be zero and all the rest of the cells to be the maximum value. Then the destination is added to a priority list in which one cell is processed according to the ascending order of their distance value. The algorithm checks the eight neighboring cells of the destination or the cell under exploration for an update of distance value if the route connecting the underling cell and the neighbor will result in a decrease in the distance value. The updated neighbors are subsequently added to the priority list for further processing. The Flood algorithm assigns distance value according to the octile distance, where vertical and horizontal paths between cells are 1 unit and diagonal path is $\sqrt{2}$ unit. P. Stucki [97] demonstrates that Flood algorithm with priority queue significantly improves computational cost compared to algorithm without a queue or with unsorted queue. In addition to priority queue, we introduce the mechanism of boundary checking. The mechanism ensures that the cells in the priority queue are the ones that are immediately adjacent to unprocessed cells. The contrast of the Flood algorithm in this study and the one with priority queue of P. Stucki's [97] shows significant improvement of computational time (Figure 2.2).

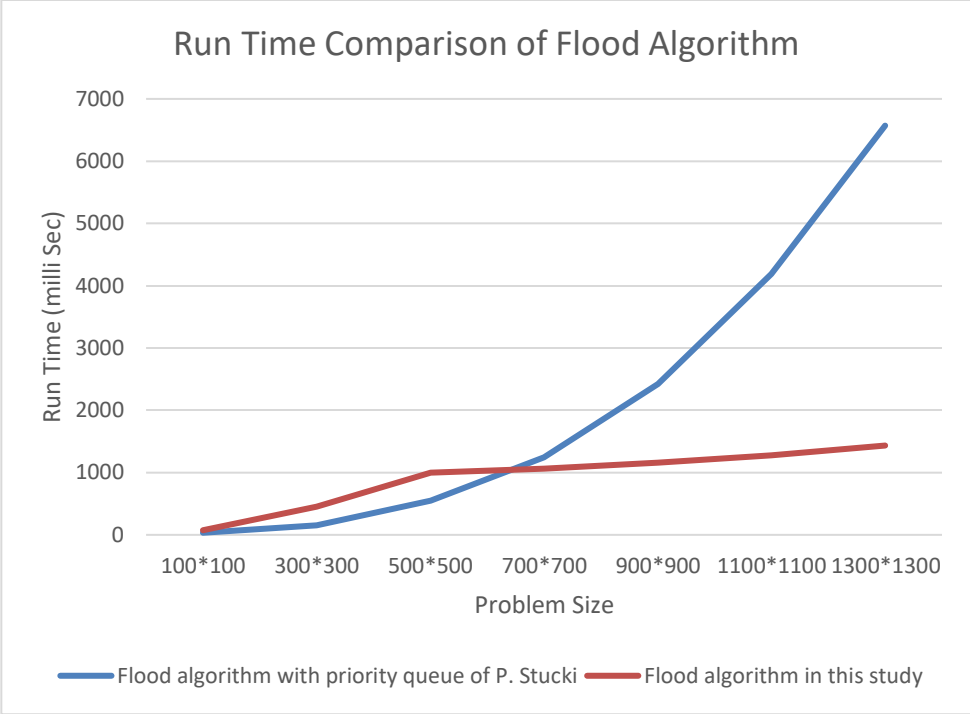

Figure 2.2 – Run time comparison of Flood algorithm in this study and in P. Stucki's [97].

2.3.2 Basic Theta Algorithm*

Basic Theta* algorithm is a variant of A*, which relaxes on the requirement of constructing paths along the edges, thus achieving any-angle path planning. Basic Theta* uses a heuristic function $h(s)$ to estimate the distance between the destination and the vertex $s \in S$. Additional two values are maintained for each vertex s: 1) g-value, $g(s)$, the true shortest length from the starting point to s, 2) $parent(s)$, the parent of vertex s, which is used to extract the optimal path after the whole map is explored. Basic Theta* also stores two global values, which are the open and close list. The open list stores the vertices that are to be processed, while the close list stores the ones that are done processing. The algorithm updates $g(\cdot)$ and $parent(\cdot)$ of an immediate neighbor s' of s by evaluating whether a decrease of $g(s')$ can be achieved by establishing a route from starting vertex to

s'via s, with the new g-value represented by $g(s) + c(s, s')$ ($c(s, s')$ is the straight line distance between s and s'). In cases where the parent of vertex s is visible to s', Basic Theta* allows sharing of parent by s and s' if a decrease of $g(s')$ is obtained. Thus, Basic Theta* achieves any-angle path planning.

2.3.3 Flood Theta Algorithm*

In contrary to Basic Theta*, Flood Theta* algorithm reverses the process of vertex expansion and initiates the calculation from the destination, reserving the capability of any-angle path construction (Figure A.1, Figure A.2). Though, the Basic Theta* has the best tradeoff between path length and runtime in any-angle algorithms, it is not guaranteed to find the optimal path [100] and could be further improved in efficiency. By bundling Theta* with flood algorithm, the above-mentioned problems are inherited. To address them, we implemented the several improvements to the original Basic Theta* when bundling with Flood algorithm and present Flood Theta* algorithm (Algorithm 2.1, Algorithm 2.2).

```
1: procedure PathPlanning()
2:     s_goal # initiate goal
3:     map # initiate map with barrier information
4:     open.append(s_goal) # open list
5:     close = φ # close list
6:     s_goal.child = s_goal
7:     s_goal.cost = 0
8:     while open is not empty do
9:         s = open.LeastCost()
10:        open.remove(s)
11:        for 8 or 24 neighbors of s: n do
12:            if InSight(child(s), n) then
13:                s_tmp = s
14:                while True do
15:                    s_tmp = child(s_tmp)
16:                    if InSight(s_tmp, n) and s_tmp.cost + c(s_tmp, n) < n.cost then
17:                        n.cost = s_tmp.cost + c(s_tmp, s)
18:                        n.child = s_tmp
19:                    end if
20:                    if s_goal is reached then
21:                        break
22:                    end if
23:                end while
24:            else
25:                if s.cost + c(n, s) < n.cost then
26:                    n.cost = s.cost + c(n, s)
27:                    n.child = s
28:                end if
29:            end if
30:            if n not in open and n not in close then
31:                open.append(n)
32:            end if
33:        end for
34:        close.append(s)
35:    end while
36: end procedure
```

Algorithm 2.1 – Flood Theta*.

```
1:  procedure InSight()
2:      x_0 = s.x
3:      y_0 = s.y
4:      x_1 = s'.x
5:      y_1 = s'.y
6:      d_y = y_1 − y_0
7:      d_x = x_1 − x_0
8:      if d_x < 0 then
9:          d_x = −d_x
10:         s_x = −1
11:     end if
12:     if d_y < 0 then
13:         d_y = −d_y
14:         s_y = −1
15:     end if
16:     α = d_y/d_x
17:     β = d_x/d_y
18:     if d_x ≥ d_y then
19:         f = 0.5 + 0.5α
20:         while x_0 ≠ x_1 do
21:             if f ≥ 1 then
22:                 if grid[x_0][y_0] is blocked then
23:                     return False
24:                 end if
25:                 y_0 = y_0 + s_y
26:                 f = f − 1
27:             end if
28:             if f ≠ 0 AND grid[x_0][y_0] is blocked then
29:                 return False
30:             end if
31:             f = f + α
32:             x_0 = x_0 + s_x
33:         end while
34:     else
35:         f = 0.5 + 0.5β
36:         while y_0 ≠ y_1 do
37:             if f ≥ 1 then
38:                 if grid[x_0][y_0] is blocked then
39:                     return False
40:                 end if
41:                 x_0 = x_0 + s_x
42:                 f = f − 1
43:             end if
44:             if f ≠ 0 AND grid[x_0][y_0] is blocked then
45:                 return False
46:             end if
47:             y_0 = y_0 + s_y
48:             f = f + β
49:         end while
50:     end if
51:     return True
52: end procedure
```

Algorithm 2.2 – InSight. The algorithm tests if two vertices on the map are free of obstacle in the straight line that connects them.

2.3.3.1 Deep Looking

In Basic Theta*, the child of the vertex must be either a visible neighbor or a visible child of its neighbor. However, this usually results in the construction of suboptimum path. Figure 2.3 is an example that Basic Theta* fails to identify the optimal path which is denoted in orange. The optimal visible child of vertex B9 is E1, which is the goal itself. The path to B9 is established by expanding B8 of which B9 is a visible neighbor. However, since the child of B8 is C6, it is not possible to obtain the optimal path for B9.

This problem can be addressed by implementing Deep Looking mechanism. Deep Looking is the procedure that the algorithm keeps updating the child of a vertex to be the child of its current child until reaching the destination or blocked by an obstacle. If the candidate child results in a better cost, the path will be established between the two vertexes. In Figure 2.3, after setting the child of B9 to be C6, the Deep Looking algorithm continues to check whether the child of C6 is visible to B9 and whether it results in better cost. And in this case, the algorithm finds that E1 is visible to B9 and the route cost is smaller than going through C6. Therefore, the optimal path B9-E1 is found instead of going through B9-C6-E1 as Basic Theta* would suggest.

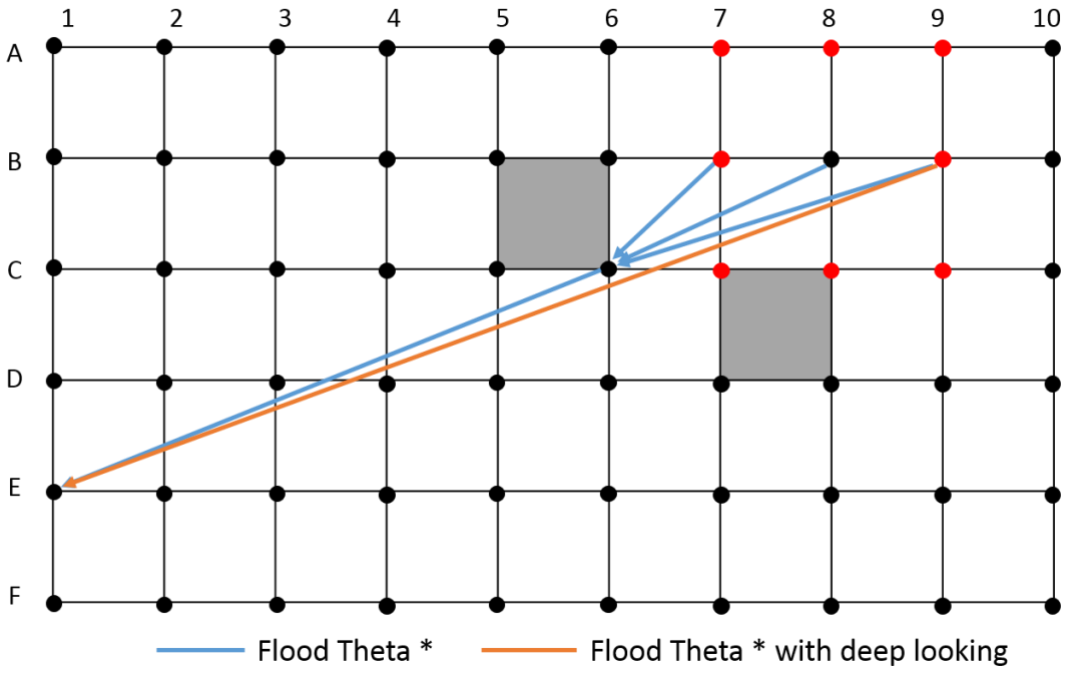

Figure 2.3 – An example of demonstrating the difference of applying deep looking vs non-deep looking. By applying deep looking, the shortest path is returned by the algorithm. The blue and orange lines represent the suboptimal and optimal paths, respectively. Total path length is 0.04%.

2.3.3.2 Larger Neighborhood Looking

In some situations, Basic Theta* reports suboptimal path because the child of vertex in expansion is not in the optimal path of its neighboring vertex (Figure 2.4). In Figure 2.4, C10 is expanded by C9 and thus has child C7. However, the path C10 – C7 – E1 is not optimum. To address this problem, the Flood Theta* algorithm should check extra layer of neighboring vertices during expansion. In the previous example, the optimal path C10-C7-E1 is obtained by expanding the 24 neighbors of D8 with the child of D8 being the goal itself. Suboptimal paths from such scenario could be completely avoided if the algorithm checks the maximum possible number of neighbors of all vertices during expansion, with a computational cost at $O(n^3)$. Alternatively, a smaller neighborhood for expansion results

in a computational cost at $O(k^2n)$ (k is the size of one side of the neighborhood). In Flood Theta* algorithm, a trade-off between path length and computational cost is made and we adopt the scenario where a maximum 24 neighbors will be processed during expansion.

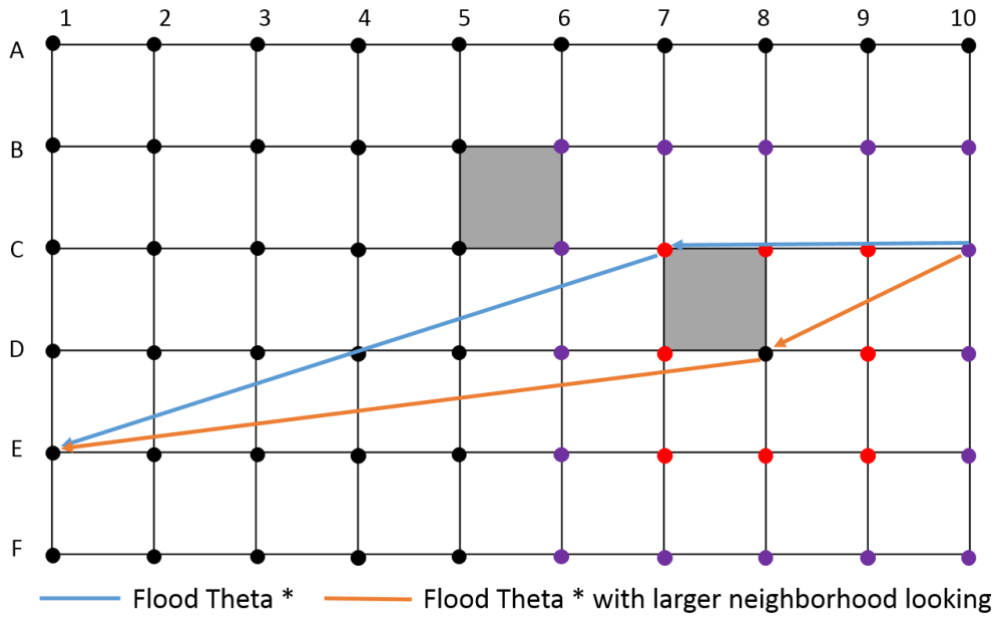

Figure 2.4 – Larger neighborhood looking. Red dots indicate neighborhood of distance 1, and purple represent neighborhood of distance 2. Total path length reduction is 0.19%.

2.3.3.3 Close Child Policy in Tie Breaking Scenario

There are situations in which the cost of a path that goes through a child of a particular vertex is equal to going directly through that vertex (Figure 2.5). In such a case, there are usually multiple choices of child for the node in expansion with the same path length cost. Instead of applying the mechanism of Deep Looking, we favor the closer child. Figure 2.5 shows a situation in which vertex D4 has two options to choose its child, either A1 (the goal) or C3. In a situation that we favor the far away child (A1 in this case), the child of D5 must be D4, which is not the optimal path. However, if we favor the close child

(C3) of D4, the child of D5 will be C3 and the optimal path is obtained. In this particular example, we won't lose the optimal path of D5 because it can be established when expanding vertex C4. But by favoring closer child, the algorithm is one step ahead in getting the optimal path and guarantees optimality in similar situations. With a large problem size, the computational time reduction could accumulate to a substantial amount.

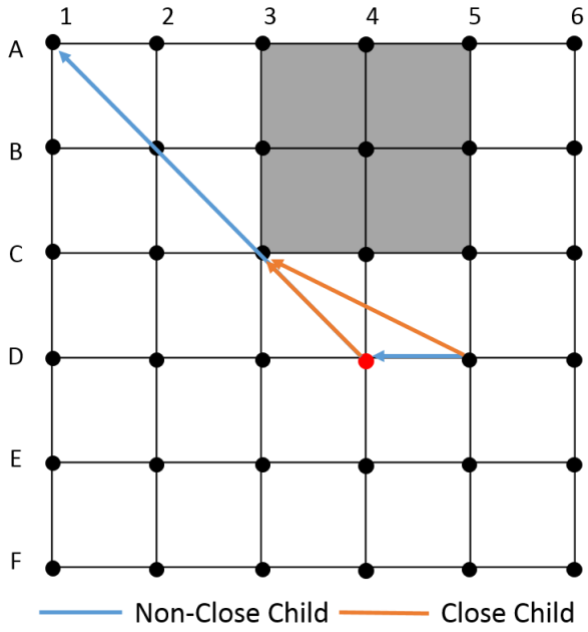

Figure 2.5 – Tie break on the choice of child. If D4 choose C3 as its child, D5 would be able to expand to the best route. If D4 choose A1 as its child, D5 would be find the best path.

2.3.3.4 Run Time and Path Improvement Analysis

To quantify the effectiveness of the above-mentioned improvements of Flood Theta* algorithm, comparison tests have been made by contrasting the computational time and path length reduction in scenarios that implements each of the three policies individually against a Flood Theta* algorithm that does not implement any improvement.

Each of the three improvements are tested on a series of maps (100*100) with randomly generated obstacles occupying 10% to 80% of the total area. To guarantee the robustness of the test, 1000 trials are conducted for each improvement, and results are summarized by averaging all data.

Flood Theta* algorithm costs less computational time with the increase of obstacle percentage, due to the decrease of free space for search (Figure 2.6). Figure 2.7 shows that with 30% obstacles, Deep Looking reaches the highest path length reduction compared to without Deep Looking (Difference: 33.79 units). Though Deep Looking mechanism cost 16.23% ($\pm$2.86%) more in computational time, the increase is acceptable. Deep Looking is effective with a wide range of obstacle percentage ranging from 0% to 60%, which covers the majority of scenarios that a researcher would need in a simulation study.

The policy of Larger Neighborhood introduces a significant amount of path reduction (Difference: 131.63 units) with 147.83% ($\pm$47.73%) increase in computational runtime (Figure 2.8). The extra burden of the computation is linearly associated with the number of neighbors for processing. Thus, a trade-off between better path planning and runtime should be made according to the purpose and scenario of the application.

Figure 2.9 shows the reduction of path length and computational time of Close-Child policy. Though the reduction of path length is not as significant as the previous two policies, the improvement is obtained at no additional computational cost. Further, adopting this policy results in better computational time for all levels of obstacle percentage. As discussed previously, favoring close child in certain situations provides

more route choices for the algorithm to construct the optimal path during vertex expansion, thus the algorithm runs faster.

All three policies appear to generate the highest path length reduction when the percentage of obstacles range from 20% to 40% (Figure 2.10). While the improvement introduced by Larger Neighborhood is significantly greater than the other two, the Deep Looking policy has a better gain to cost ratio (Deep Looking vs Larger Neighborhood: 8.71 vs 6.52).

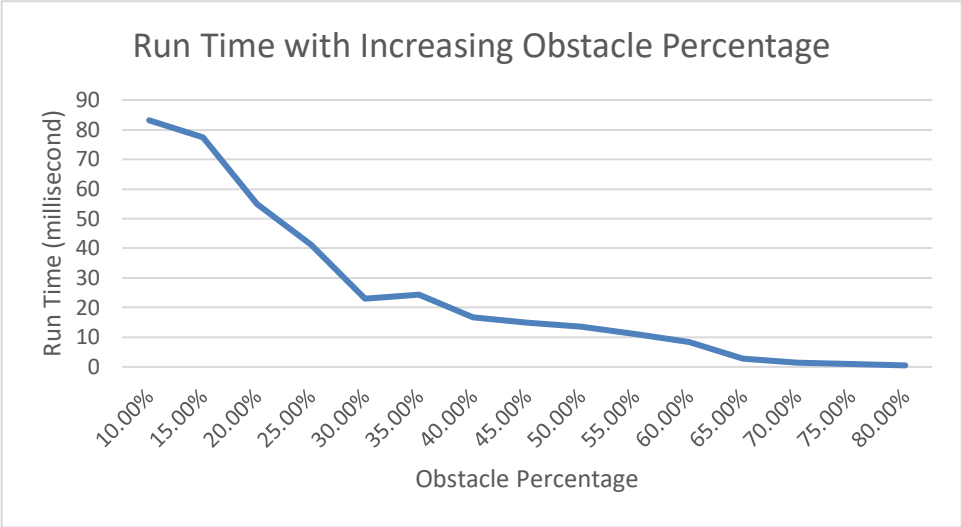

Figure 2.6 – The relationship between obstacle percentage and runtime of Flood Theta* algorithm. With increasing number of obstacles on the map, there are less and less walkable space for the algorithm to traverse. Therefore, the runtime decreases.

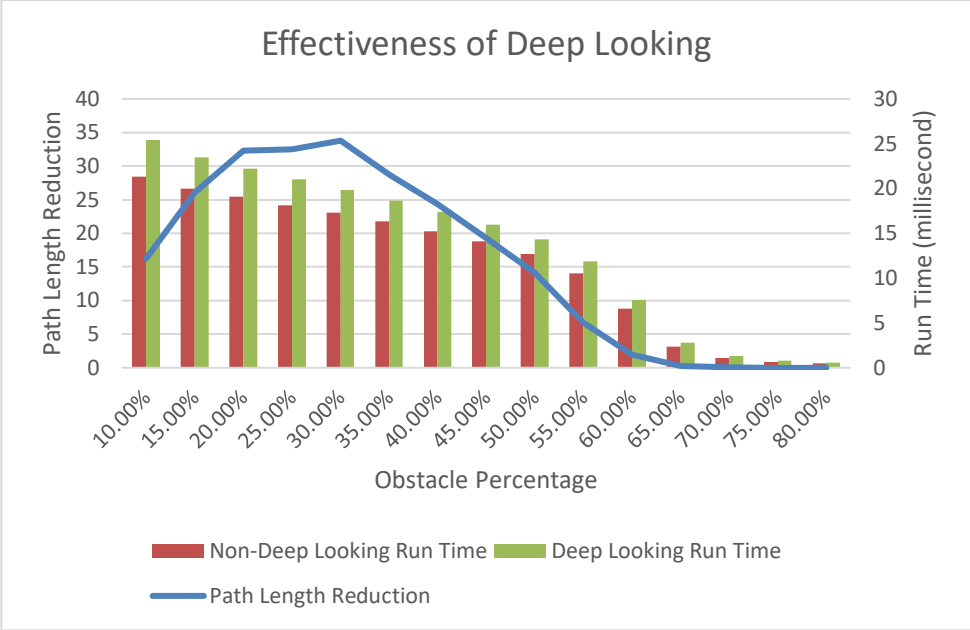

Figure 2.7 – Total path length reduction of Deep Looking, averaged on 1000 100*100 random maps. The runtime of deep looking is slightly more than non-deep looking and the most amount of path reduction occurs at 30% obstacles.

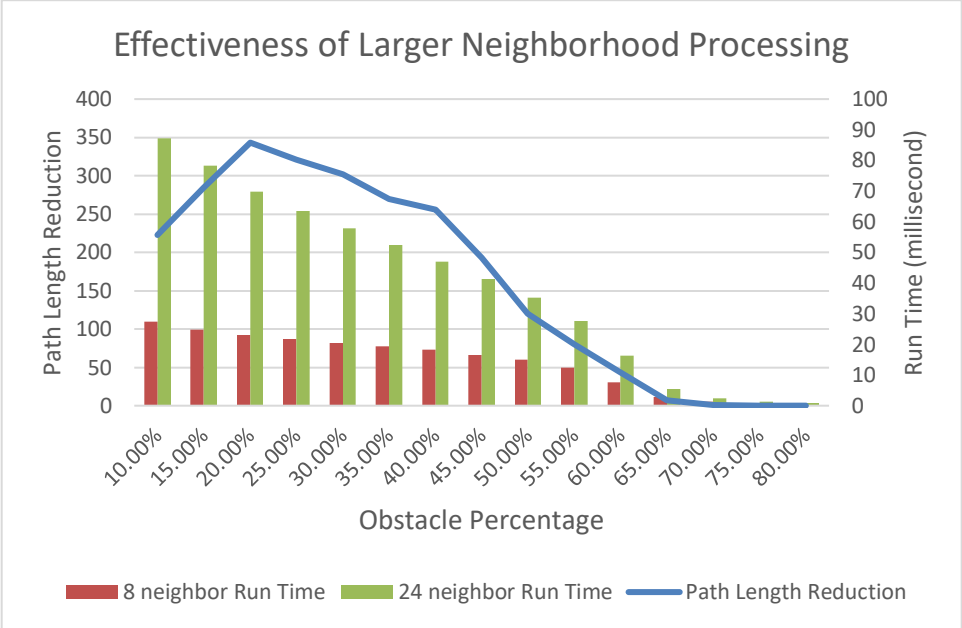

Figure 2.8 – Total path length reduction of Larger Neighborhood Looking.

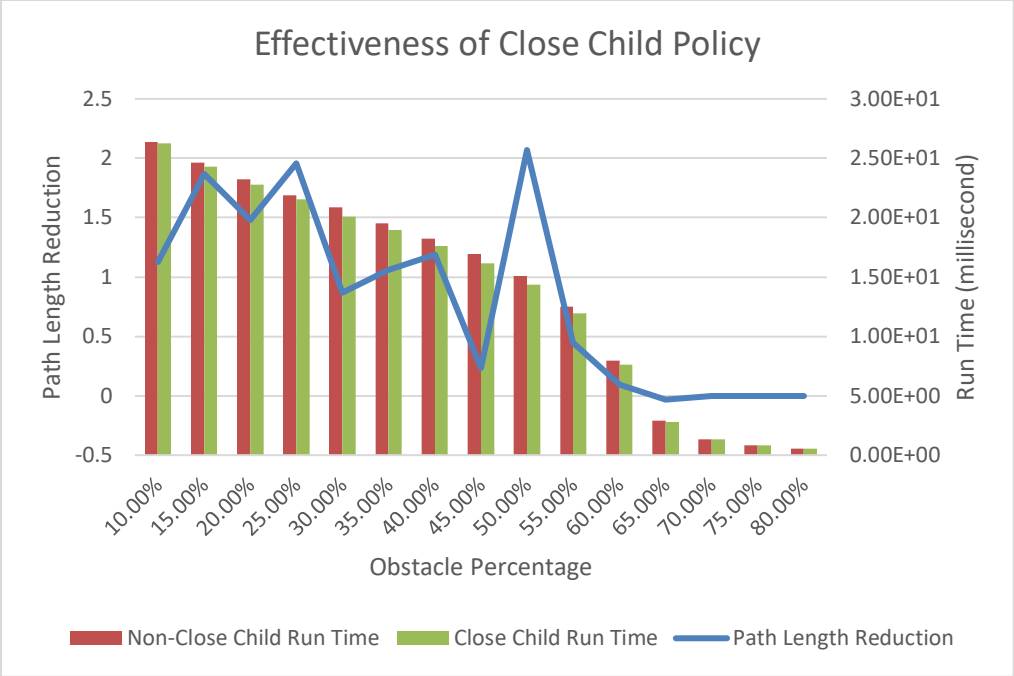

Figure 2.9 – Total path length reduction of close-child VS non-close child averaged on 1000 100*100 random maps. Close-Child policy achieves reduction in path length and computational time at the same time.

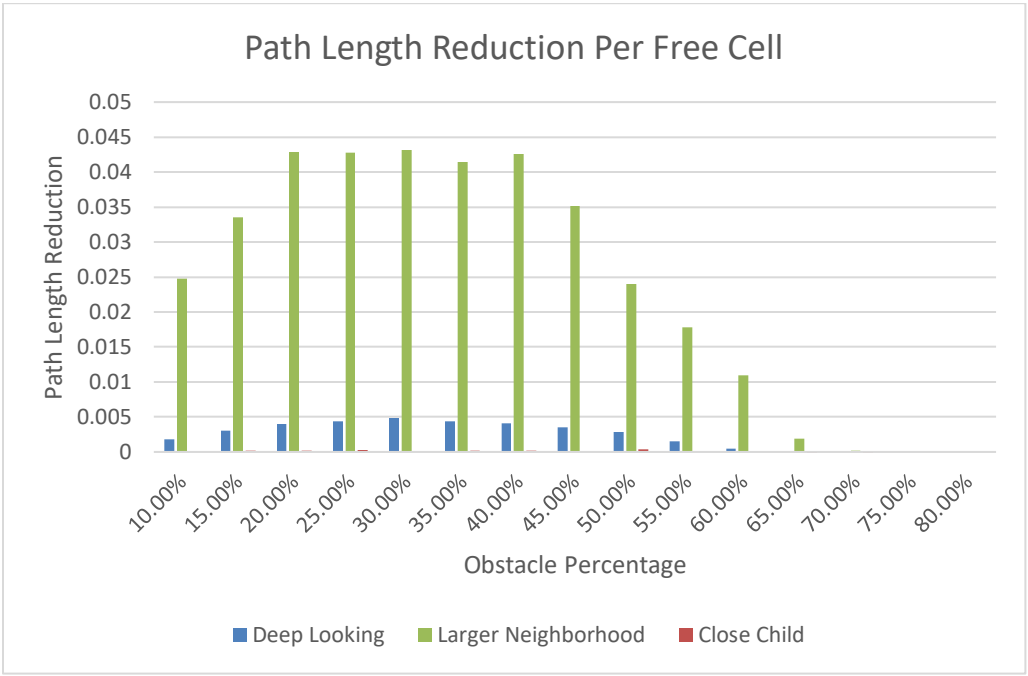

Figure 2.10 – Path length reduction per free cell for the three policy: Deep Looking, Larger Neighborhood and Close Child.

2.4 Projection Based Interactive Velocity Avoidance Model

2.4.1 Limitations of Social Force Model

The traditional social force model is consisted of the force applied by the destination, static obstacles, walls and dynamic obstacles. The movement of an agent i ($F_i^{To}[n]$) is the collective effect of moving along desired direction ($F_i^{At}[n]$), avoidance of walls w (F_{wi}^{Wa}), obstacles k ($F_{ki}^{Ob}[n]$) and other agents j ($F_{ji}^{Ot}[n]$) (2.1).

$$F_i^{To}[n] = F_i^{To}[n-1] + F_i^{At}[n]w_i^{At} + \sum_w F_{wi}^{Wa}[n]w_i^{Wa} + \sum_k F_{ki}^{Ob}[n]w_i^{Ob} + \sum_{j \neq i} F_{ji}^{Ot}[n]w_i^{Ot} \quad (2.1)$$

However, the repulsive force generated by obstacles may not result in realistic collision avoidance behavior. As in shown Figure 2.11, pedestrian A applies repulsive force to both pedestrian B and C, as they are closing in to A. Ideally, C should make a more dramatic change of course compared to B, since A and C have a much larger overlap of projection and are in imminent expectation of collision. But the combined force F_{new1} and F_{new2} calculated by the social force model do not reflect the actual need of course changing as indicated in Figure 2.11. In the particular example, B will make a turn of course much faster than C, which is not a true representation of real human behavior.

Additionally, social force model applies the repulsive forces whenever obstacles are in vicinity of agents regardless of the direction of movement. As shown in Figure 2.11, pedestrian B does not need to avert from A, since the projection of the route of B will not intersect with A's. J. Ondrej, et al. [106] also point out that social force model fail to resolve collision avoidance in diametrically opposed and bidirectional opposed movement. To

address the above issues and to make the collision avoidance more realistic while maintaining a reasonable burden of computation, we propose the Projection Based Interactive Velocity Avoidance Model.

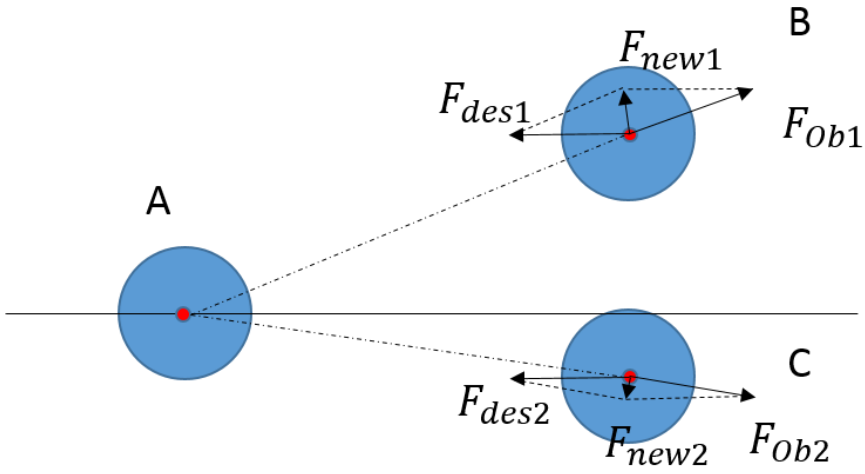

Figure 2.11 – Avoidance force applied by dynamic obstacles in a social force model.

Projection Based Interactive Velocity Avoidance Model resembles social force model in the application of combining forces but differs in two ways. First, the model applies avoidance velocity to the agent based on the projection of collision, instead of applying forces when agents are in vicinity as social force model will do. Second, the direction of avoidance velocity imposed on agents is interactive. Thus, it guarantees that the agents' behavior is more proactive and realistic in terms of achieving collision avoidance.

2.4.2 Projection of Collision of Agents with Negligible Size

Figure 2.12 shows a generalized situation where agent A and B with negligible size may collide as they proceed with their original setting of movement. The velocity $\vec{V}_A$ and

$\vec{V}_B$ can be decomposed onto x and y axis as $\vec{V}_A = \vec{V}_{Ax} + \vec{V}_{Ay}$ and $\vec{V}_B = \vec{V}_{Bx} + \vec{V}_{By}$. $\vec{P}_{Ax}$ and $\vec{P}_{Bx}$ represent the positions of A and B projected on x-axis. If $\exists \tau > 0$, such that $\vec{P}_{Bx} - \vec{P}_{Ax} + (\vec{V}_{Bx} - \vec{V}_{Ax})\tau = 0$, the two agents will collide at time $t = \tau$ when $\vec{V}_{Ay} = \vec{V}_{By}$.

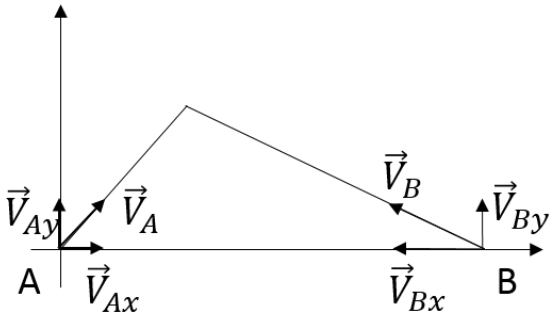

Figure 2.12 – Decompose of velocity on a collision triangle.

2.4.3 Projection of Collision of Agents with Non-negligible Size

In our simulation model, the agent is represented as a circle with a certain radius and the size of an agent should be considered in the projection of collision. To predict the occurrence of collisions, the following equation should be solved for t:

$$\left|\vec{P}_{BA} + (\vec{V}_A - \vec{V}_B)t\right| \geq r_a + r_b \tag{2.2}$$

$\vec{P}_{BA}$: vector pointing from position of B to A. $\vec{P}_{BA} = \vec{P}_A - \vec{P}_B = (P_x, P_y)^T$

$\vec{V}_A$: velocity of agent A. $\vec{V}_A = (V_{Ax}, V_{Ay})^T$.

$\vec{V}_B$: velocity of agent B. $\vec{V}_B = (V_{Ax}, V_{By})^T$.

r_a: radius of agent A.

r_b: radius of agent B.

Assume

$$\begin{cases} \Delta V_x = V_{Ax} - V_{Bx} \\ \Delta V_y = V_{Ay} - V_{By} \end{cases}$$

The equation (2.2) has a non-negative solution when the following conditions satisfy:

$$\left(\Delta V_x^2 + \Delta V_y^2\right)(r_a + r_b)^2 - P_x^2 \Delta V_y^2 \geq 0 \tag{2.3}$$

$$P_x \Delta V_x + P_y \Delta V_y \leq 0 \tag{2.4}$$

2.4.4 Three Situations of Potential Collisions

A collision triangle can be formed in observance of a potential collision (Figure 2.12). The triangle is consisted of an edge between point A and B, and two edges in line with the direction of velocity of A and B. Collision scenarios can be generalized into three categories (Figure 2.13). The first is that the collision triangle is consisted with a third point which is being pointed to by both $\vec{V}_A$ and $\vec{V}_B$, where the two agents are moving toward the same direction (Figure 2.13a). The second scenario is that the two agents are moving in opposite direction of each other and the projection of paths have overlap (Figure 2.13b). In this scenario, the third point of the triangle is pointed to by only one of the velocities. The third situation is that no collision triangle can be formed where the velocities are parallel to each other or the edges of the triangle are merged (Figure 2.13c, d).

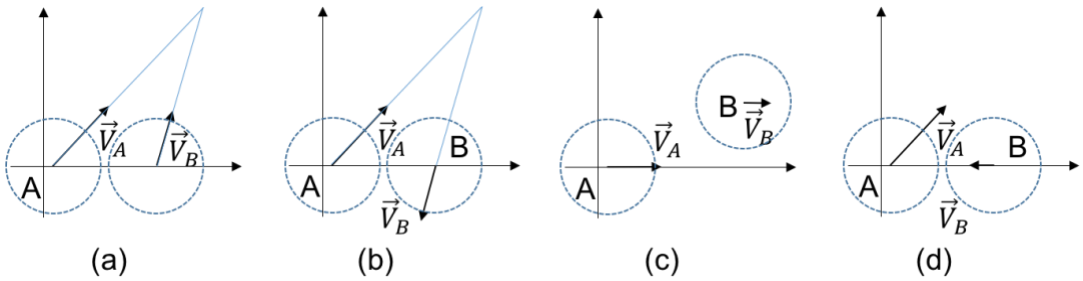

Figure 2.13 – Three scenarios of collision triangles. a). Velocities of A and B point to the third point of the collision triangle. b). Only one of the two velocities point to the third point of collision triangle. c) and d). No collision triangle can be formed.

In observance of collision, divergent velocity will be added to the agents to update the course of agents. The solutions space of divergent velocity $\vec{\mathrm{V}}_{\mathrm{r}}$ in the above-mentioned situations are explored as follows. The addition of $\vec{V}_r$ only need to affect the magnitude of $\Delta\vec{V}_y$. Therefore, to determine $\vec{V}_r$, we only need to set (2.5) to be zero after addition of $\vec{V}_r$ to (2.3).

$$\left[\Delta V_x^2 + \left(\Delta V_y + 2V_r\right)^2\right](r_a + r_b)^2 - \left(\Delta V_y + 2V_r\right)^2 P_x^2 = 0 \tag{2.5}$$

Where, $V_r = |\vec{V}_r|$

The solution of (2.5) is:

$$V_r = \frac{-[\Delta V_y^2(r_a + r_b)^2 - \Delta V_y \Delta P_x^2] \pm \sqrt{[\Delta V_y^2(r_a + r_b)^2 - \Delta V_y \Delta P_x^2]^2 - [(r_a + r_b)^2 - \Delta P_x^2][(\Delta V_x^2 + \Delta V_y^2)(r_a + r_b)^2 - \Delta P_x^2 \Delta V_y^2]}}{2[(r_a + r_b)^2 - \Delta P_x^2]} \tag{2.6}$$

Lemma 1:

*According to (*2.6*),* $\vec{V}_r$ *is guaranteed to have solutions when (*2.3*) is not negative.*

Lemma 1 guarantees that when there is a potential collision, we can always find solutions for the divergent velocity. And since $(r_a + r_b)^2 - \Delta P_x^2$ is always negative, the solution space of V_r is the value that makes (2.4) non-positive.

With the collision triangle in situation Figure 2.13a, the two solutions of $\vec{V}_r$ have equal norm. In situation shown as in Figure 2.13b, the two solutions have different norms (Figure 2.14, Figure 2.15). Intuitively, it is easier for agent A to turn to its left rather than its right to avoid collision. Thus, the norm of $\vec{V}_r$ is smaller in situation of Figure 2.14a than in situation of Figure 2.14b. When no collision triangle can be formed, the solutions of divergent velocity do not have the same norm (Figure 2.16 - Figure 2.19). In such situations, there is always one direction for the agent to turn to, which requires much less effort than the other. The calculation from the above equations is in accordance with the phenomena.

Since $(r_a + r_b)^2 - \Delta P_x^2$ is always negative, it can be concluded that the solution space of $|\vec{V_r}|$ is ranging from two critical values to either positive infinity or negative infinity. The property of the solution space of $|\vec{V_r}|$ provides us with more maneuverability in simulation. For example, when applying the divergent velocity to the agent, we could set the magnitude of the velocity to any desired level such that the magnitude is positively correlated with the urgency of the collision avoidance.

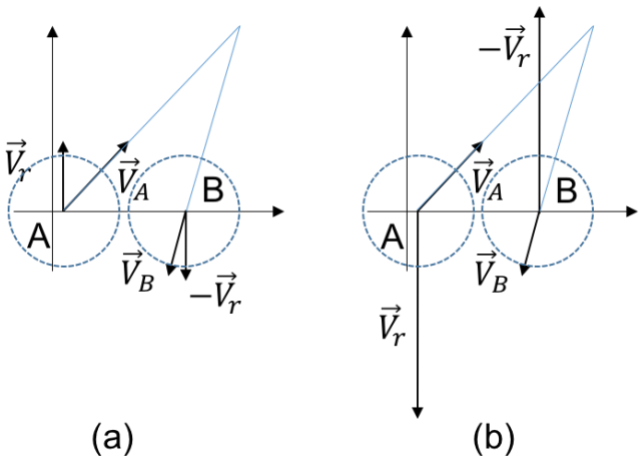

Figure 2.14 – Solutions of divergent velocity of the situation Figure 2.13b.

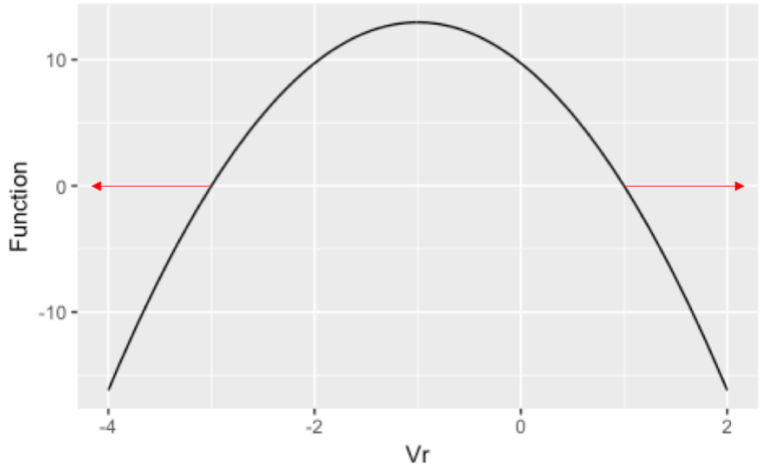

Figure 2.15 – Solution space of divergent velocity for situation Figure 2.13b, indicated by red arrows.

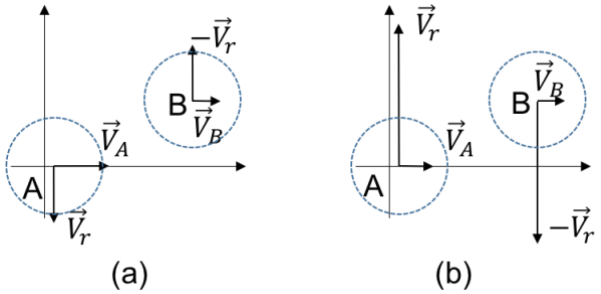

Figure 2.16 – Solutions of divergent velocity for situation Figure 2.13c.

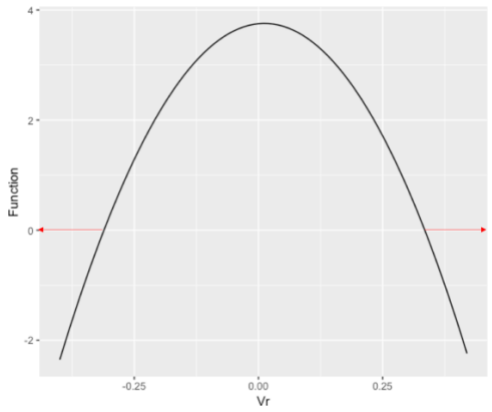

Figure 2.17 – Solution space of divergent velocity for situation Figure 2.13c, indicated by red arrows.

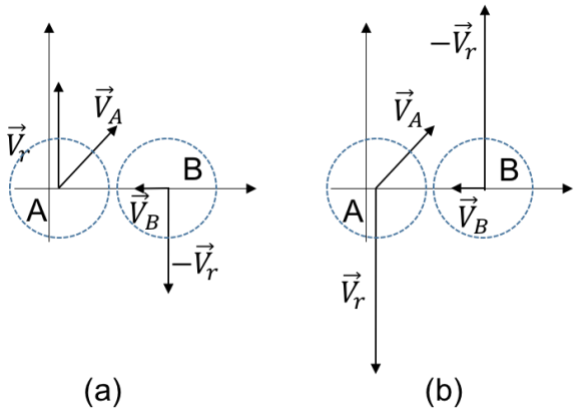

Figure 2.18 – Solutions of divergent velocity for situation Figure 2.13d.

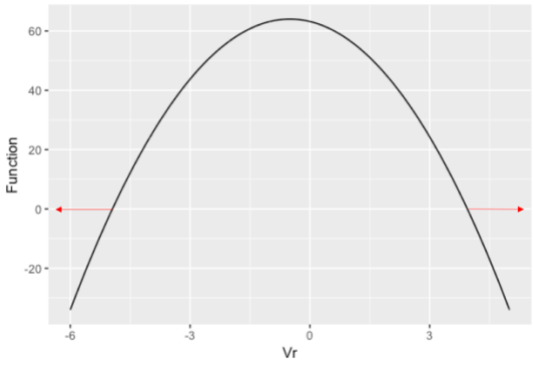

Figure 2.19 – Solution space of divergent velocity for situation Figure 2.13d, indicated by red arrows.

2.4.5 Optimization of Avoidance Velocity

Equation (2.5) provides two choices of divergent velocities $\vec{V_r}$ in all scenarios shown in Figure 2.13. A decision strategy is in need to determine which of the choices should be adopted during the simulation. Though the addition of proper scaled divergent velocity $\vec{V_r}$ in opposite directions guarantees the avoidance of collision, the two choices of divergent velocities result in different cost and crowd behavior. With the aim to resolve collision avoidance with the least change of original behavior, the cost of divergent velocities should be compared before implementation. Therefore, we propose the measurement of cost to be the weighted summation of the change of direction and magnitude of the velocity.

$$C = p\Delta\theta + q\Delta v \tag{2.7}$$

p, q: coefficients

$\Delta\theta$: change of velocity direction

Δv: change of velocity magnitude

As shown in Figure 2.20, we construct the model to test the cost of adding divergent velocity under different situations where a collision triangle is formed. The cost of the two divergent solution is obtained by moving the collision point alone the arc from point D to E with the coefficient being $p = 0.7, q = 0.3$ (Figure 2.21). Figure 2.22 shows four segments of the distribution of cost over the two choices of divergent velocity, in which each of the two divergent velocities become more efficient alternatively as the collision

point changes. In the implementation of the simulation platform, the choice of divergent velocity is based on the principle of the minimization of cost.

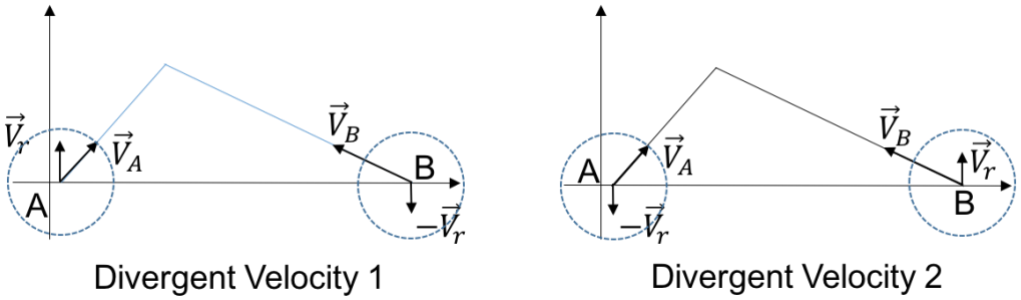

Figure 2.20 – Two scenarios of adding divergent velocity to agents.

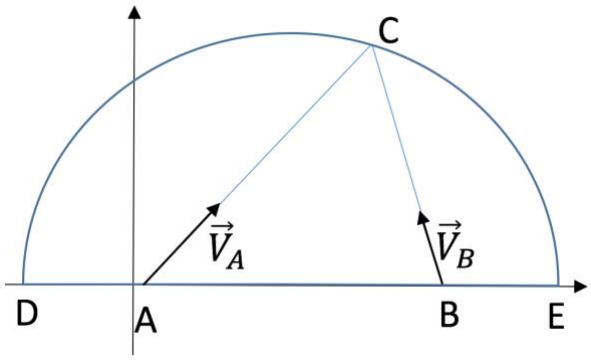

Figure 2.21 – Experiment setting of exploring the cost of adding divergent velocity. The cost of divergent velocity is measured with the collision point going from point D to E along the half circle formed by the two points.

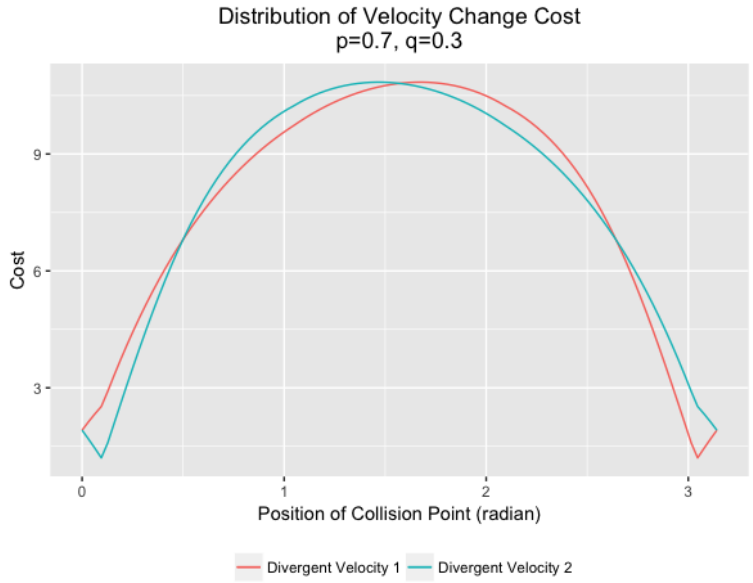

Figure 2.22 – Distribution of velocity change cost given two scenarios of divergent velocity.

2.4.6 Validation of the Performance of Collision Avoidance

Formation of self-organized behavior has been widely used to evaluate the performance of ABM [123, 124]. The most important behaviors include:

1) Lane formation [125]: in bidirectional movement in a narrow corridor, pedestrians automatically start forming two lanes of traffic with people in each lane moving in the same direction.
2) Intersecting flows [123]: two or four intersecting flows of pedestrians should be able to move through the intersection without additional guidance except for the pedestrian's own avoidance decision.
3) Faster-is-slower effect [126]: when pedestrians move up to a bottleneck and cause congestion, the overall speed of the crowd will slow down due to the

frictions. In an alternative situation where pedestrians walk slower, the congestion will be less severe, and the crowd movement will be faster.

4) Turbulence [127]: In a high density crowd, the movement of pedestrians is beyond the control of their decision. Rather, they are pushed around due to the forces applied to them.

We illustrate the performance of our collision avoidance model in four scenarios. First, we test lane formation in a narrow corridor, in which the flows of traffic move bidirectionally against each other. After initialization of the simulation, the agents quickly converge to one side of the corridor upon meeting in the center, followed by smooth flow of traffic afterwards (Figure 2.23). Second, the test scenario is built on an intersection with two way traffics that meets perpendicularly in the center of the cross (Figure 2.24). Third, a similar scenario on an intersection is built with four way traffics, in which the avoidance problem is more complex (Figure 2.25). In the above two simulations, agents are able to wait and seek gaps in the other crowd and reach their destination with a reasonable route. Pushover and oscillation are also observed, resembling real human behaviors (Figure 2.24, Figure 2.25). Forth, we test collision avoidance behavior in antipodal movement, in which the agents form a circle in initialization and move diametrically to the opposite side of the map. In the simulation, 5000 thousand agents meet in the center and rotate clockwise while agents start leaving the crowd as they reach their destination (Figure 2.26). In contrast to social force [105] and RVO [107] models, our model is able to resolve collision avoidance problems in complex situations, providing realistic modeling of human group behavior.

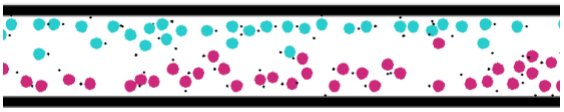

Figure 2.23 – Lane formation of virtual people. People with different destinations resolve collision by merging into two flows by either side of the narrow corridor.

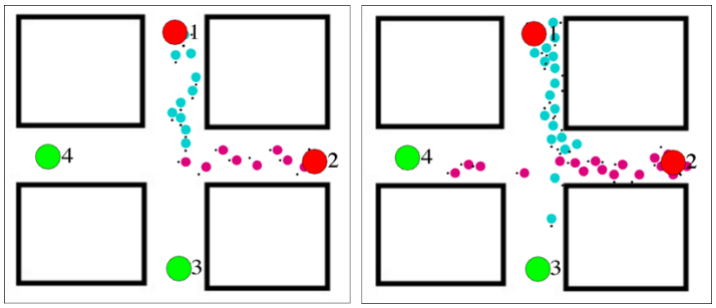

Figure 2.24 – 2000 people from two entrances make through the cross.

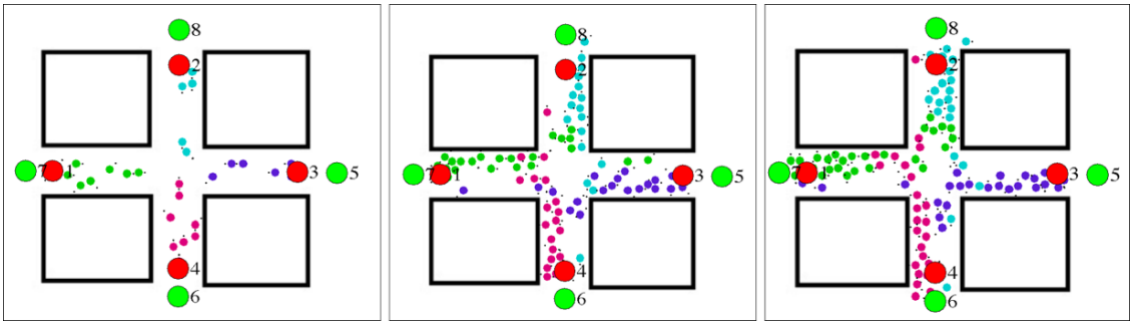

Figure 2.25 – 2000 people coming from the four direction of the cross and move to the exit on the opposite side.

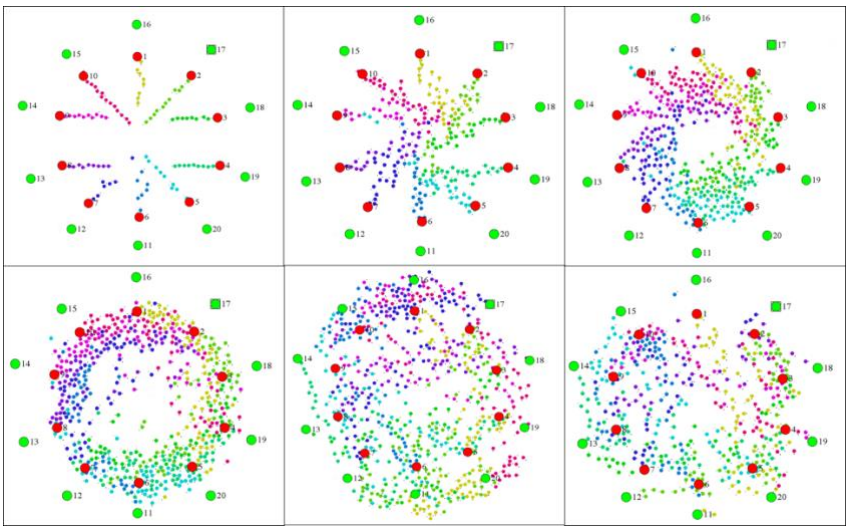

Figure 2.26 – Simulation of 5000 people moving toward antipodal position. The virtual people meet in the center and form a spiral movement and resolve the collision problem.

2.5 Grouping Rules and Dynamic Leadership

In many situations, people in crowds form small groups, such as friends of family, and a collective decision and behavior is presented as a consequence. In our simulation, we implement rule-based group behaviors. Virtual people form groups with sizes chosen by the simulator, and then follow the predefined rules of groups. The rules include: 1) Adjacency: members of the group stay close to each other; 2) Waiting behavior: when some member is far behind, other members stop and wait. 3) Retrieving behavior: when some member stays too far away from the group, the other members walk back to get the lost one; 4) Group decision: A group decides and moves to the same destination.

Except for emergency evacuation, people who visit an entertainment facility are simply regular people as a family or group of friends. Usually, there is no explicit leader or follower in the group. The decision making and following behavior is more complicated, where people switch between the roles of leading and following constantly. The decision

of the group is usually not installed by a specific person, rather it is a result of team work. Therefore, we propose the mechanism of dynamic leadership, in which all group members participate and contribute in leading. When a group of people engage in movement, people choose the leader which result in minimum steering from his/her original path.

2.6 Emotion Modeling

Emotion is one of the key factors in describing the action of a person and a crowd. We implement an emotion model that integrates personality, dynamic emotion and emotion contagion, associated with a function that project the status of emotion to the actions of the simulated agents. In this study, we present a similar design of personality and emotion model as F. Durupınar [128] suggests, where OCEAN (openness, conscientiousness, extroversion, agreeableness, neuroticism) [129] and PAD (Pleasure, Arousal, Dominance) [130] models are integrated. And we present a novel implementation of emotional contagion model described in later section. The emotion model updates the emotion status of individuals according to the process of event information and emotion propagation from other agents and subsequently transmits the status to decision making of agents (Figure 2.27).

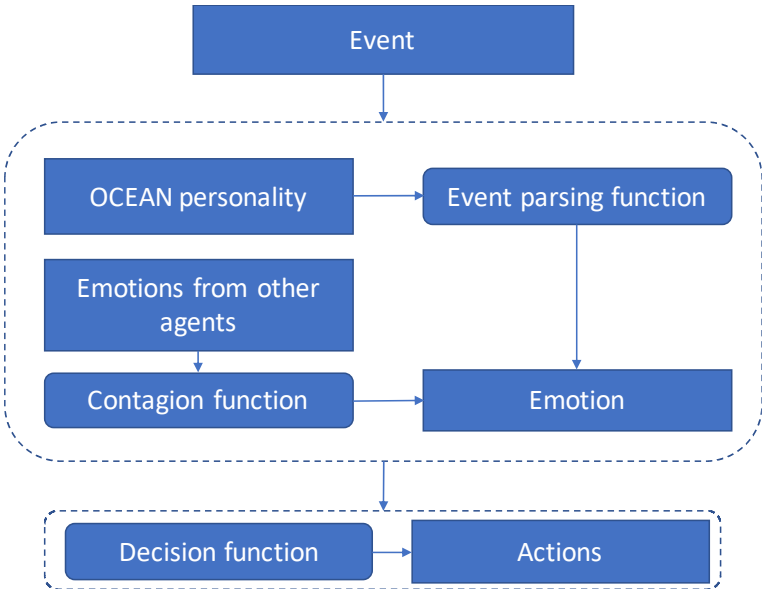

Figure 2.27 – Flowchart of personality and emotion model.

2.6.1 Personality model

Modeling crowd with heterogenicity is the key for realistic and accurate simulation, where a reasonable personality distribution could be utilized to represent the underlining population. The OCEAN personality is composed of openness, conscientiousness, extroversion, agreeableness and neuroticism, which are orthogonal axes in describing the phycological characteristics of a person. In the simulation, we use vector $\boldsymbol{p} = [P_O, P_C, P_E, P_A, P_N]^T$ to represent the personality space of simulated agents. The value of the elements in the vector range between 0 and 1. Table 2.1 describes the component of OCEAN model and provided a brief explanation.

Table 2.1 – OCEAN personality model and explanation.

Factor	Positive value	Negative value

Openness	Curious, Imaginative, Individualist	Conventional
Conscientiousness	Conscientious, Organized	Impulsive, Distracted
Extroversion	Gregarious, Enthusiastic	Not social
Agreeableness	Friendly, Popular, Altruist	Aggressive, Intransigent
Neuroticism	Emotionally stable, Calm	Anxious, Angry, Self-conscious

2.6.2 Emotion model

The emotional status of an agent is determined initially with its personality and the initial emotion serves as the baseline which the later emotion status decays to. In the process of simulation, the emotion is updated with self-perception and environmental contagion. Above all, the emotion of agent i at time t is defined as:

$$\boldsymbol{e}_{i,t} = \beta \boldsymbol{e}_{i,0} + (1-\beta)\boldsymbol{e}_{i,t-1} + [f(event, \boldsymbol{p}_i) + g(\boldsymbol{p}_i, \boldsymbol{a}_i)] \quad (2.8)$$

$\boldsymbol{e}_{i,t} = [pleasure, arousal, dominance]^T$ is the emotion vector at time t, β is the decaying factor between 0 and 1, which carry out the decaying to the initial level (the reflection of the underline personality), $\boldsymbol{p}_i$ is the personality vector of agent i, $f(event, \boldsymbol{p}_i)$ is the perception function of agent i in observance of event, $g(\boldsymbol{p}_i, \boldsymbol{a}_i)$ is the emotional contagion function and $\boldsymbol{a}_i$ is the population excluding agent i. The initial emotion status is determined by the personality traits using the following formula [131]:

- Pleasure = 0.21*Extraversion + 0.59*Agreeableness + 0.19*Neuroticism
- Arousal = 0.15*Openness + 0.30*Agreeableness - 0.57*Neuroticism
- Dominance = 0.25*Openness + 0.17*Conscientiousness + 0.60*Extraversion - 0.32*Agreeableness

Table 2.2 describe the octant of PAD space with adjective of the emotional status.

Table 2.2 – Octants of PAD space.

Positive	Negative
+P+A+D Exuberant	-P-A-D Bored
+P+A-D Dependent	-P-A+D Disdainful
+P-A+D Relaxed	-P+A-D Anxious
+P-A-D Docile	-P+A+D Hostile

2.6.3 Emotion Contagion Model

Previous researchers have noticed the resemblance between emotion transmission and disease contagion and thus proposed the classic SIR model and its variants [132, 133]. The SIR model describes the contagion of emotion similarly to the contagion of disease, in which a person stays in one of the three states, susceptible, infected and recovered. Variates of this model may include a threshold to regulate the contagion. In our model, we address several critical issues towards realistic emotion modelling. First, we view emotion status

as continuous distributed on certain measurement rather than a discrete process that thresholds can be assigned to. Second, emotion interaction differs from disease contagion in that recovered individuals can easily be reactivated given enough stimuli. Third, there exist interactions between recovered and infected individuals, where recovered individuals may translate others into recovered state. Forth, an infected state in SIR model prevents the agent from being elevated to a higher level, however, we presume the opposite. In our application, we argue that people's emotion could be continuously elevated with constant or increased stimuli. The definition of the emotion contagion model is:

$$g(\boldsymbol{p}_i, \boldsymbol{a}_i) = \boldsymbol{w} \cdot \boldsymbol{p}_i \frac{1}{n} \sum_s C \alpha_{sr} \boldsymbol{e}_s \tag{2.9}$$

where $\boldsymbol{e}_s$ is the sender's emotion vector, n is the total number of agents in the vicinity of agent i, α_{sr} is the strength of connection depending on distance, $C = \omega_c P_C + \omega_E P_E + \omega_A P_A$ ($\omega_c = 0.8,\ \omega_E = 1,\ \omega_A = 0.7$) is the expressiveness of the sender, $\boldsymbol{w} = [1, 0.2, 0.1, 0.6, 0.7]^T$ is the perception vector of the receiver, $\boldsymbol{p}_i$ is the personality vector of the receiver i. The strength of connection α_{sr} is the measurement between 0 and 1, determined by the distance of two agents. The expressiveness of the sender is determined by his/her personality. It is reasonable and natural to assume that people with different personality would express emotions with different degree. Perception of emotion depends on the personality of the receiver. For example, a person with strong conscientiousness would not easily adjust himself to a panic state while a person with strong neuroticism would do.

2.6.4 Perception of Event

The descriptors of event in the simulation model include: crowdedness, goal achieving and hazard, defined as $\boldsymbol{\psi} = [\psi_c, \psi_g, \psi_h]^T$. In our model, crowdedness and hazard contribute to negative emotion activation while goal achieving contribute positively. Specifically,

$$f(\boldsymbol{\psi}, \boldsymbol{p}_i) = (\boldsymbol{w} \cdot \boldsymbol{p}_i)(\boldsymbol{v} \cdot \boldsymbol{\psi}) \tag{2.10}$$

where $\boldsymbol{v} = [-0.5, 0.8, -0.9]^T$ is the vector to transform the event vector to emotion. In our simulation, positive emotion will generate normal actions while anxious emotion due to emergent situations will impede the movement of pedestrians.

2.7 Optimization in Simulation

Using optimization technique in simulation to study emergency evacuation scenarios has become an major aspect in the research community of agent-based simulation [134-137]. In an emergency scenario, we seek to minimize the overall evacuation time of a facility and identify the optimal flow of pedestrian. Specifically, the flow of traffic in our simulation platform is defined using a transition matrix, which dictates the number of pedestrians travelling between points of interests. The optimization procedure with this simulation platform is consisted of six major steps (Figure 2.28). First, certain variables in the transition matrix should be selected as the variables to be optimized. Second, the simulation should be run several times with random initialized variables. Third, the objective value of the previous simulations should be calculated. Forth, the function of variables is approximated using a neural network to fit the objective value. A customized level of mean square error (MSE) should be assigned according to the specificity of the

case. Fifth, use the trained neural network as the objective function and solve for optimized solution. Sixth, simulate using the optimized variable for validation.

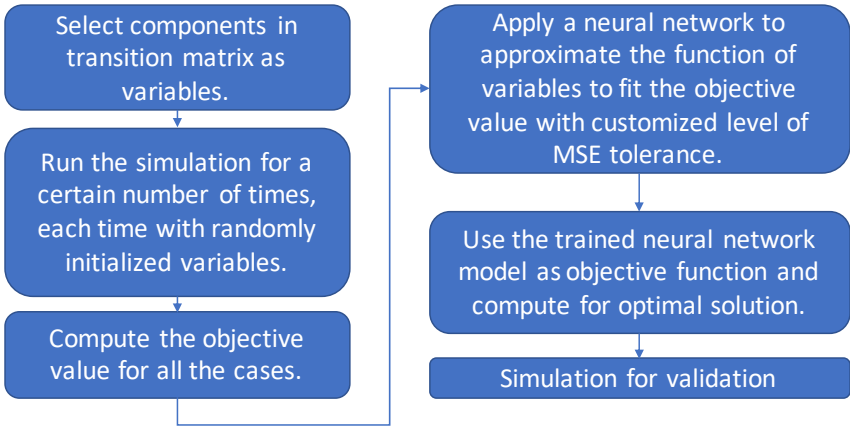

Figure 2.28 – Optimization procedure in the simulation platform.

2.8 Experiment and Result

2.8.1 Georgia Aquarium

The Georgia Aquarium is the largest aquarium in the US with over 8.5 million gallons of water and 120,000 animals. The Georgia Aquarium is gaining popularity over the years (Figure 2.29) and the management group of the facility seeks to understand the capacity of operation and install upgrades in order to cater for more tourists. The daily maximum number of guests in 2014 reached as high as 14156 people, which causes serious pressure to the daily operation. Operation research methodologies have long been applied as a consulting approach for tourist-attraction leaders and advance their decision-making capabilities. Agent-based simulation has been an important approach in facility design [138], operation logistics [139, 140] and risk management [141]. In the collaboration with Georgia Aquarium, we demonstrate the capability of the simulation platform in

incorporating the logistic data, capturing the stochastic nature of large event, optimizing the resource allocation and modeling human decision making. Our objective is to 1) understand the guests flow and bottlenecks in operation, 2) implement optimized operations and resource allocation aiming at improved guest experience, 3) reduce the risk in an emergency situation with guided evacuation routes optimized by the platform.

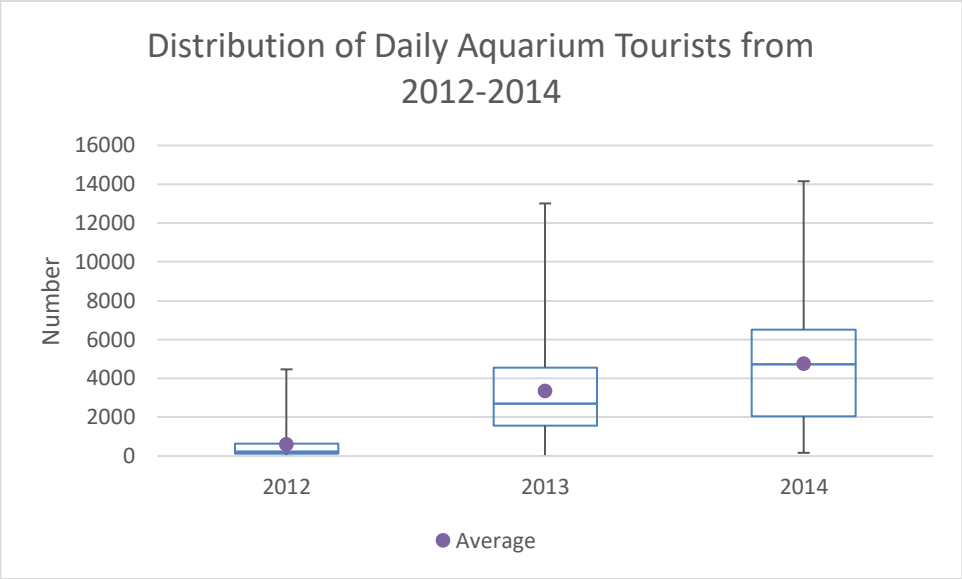

Figure 2.29 – Distribution of daily tourists of Georgia Aquarium from 2012 – 2014.

2.8.1.1 Data Collection and Analysis

In the collaboration with Georgia Aquarium, we collected 183, 365 and 209 days of records of admission for 2012, 2013 and 2014 respectively. To provide additional data for accurate modeling of the guest flow and operation characteristics, our team observed the movement within the aquarium from May to August 2014. We identified 11 points of interest (POIs), spread across two floors, at which performed time and motion study. The POIs include Coldwater Quest, Ocean Voyager, Tropical Diver, Georgia Explorer, River Scout, Dolphin Tale, Monster and 3D theater, Café, walking area, entrance and gift shop

(exit) (Figure 2.33). We collected the data on interarrival times of people for all POIs, guests' choices of POIs, travel time in the walking area between POIs and visiting time within POIs. We designed and handed out the customer timestamp card to record the visiting time of each exhibit. The card was handed to guests when they entered and was collected after they left. To approximate the service time of each POI, we either use probability distributions or construct a complex formula (combinations of polynomial and exponentiation) to fit the visit time. The number of tourists generally reaches its highest number on Saturday (Figure 2.30, Figure A.3). And the busiest month is usually overlapped with a national holiday, such as Independence Day and Christmas (Figure 2.31). Being able to successfully handle the highest number of guests and get ready to accept continuously increasing popularity has been become the priority of the management of the aquarium. In our simulation, we simulate the scenario in which the aquarium receives the maximal number of tourists of 2014 and identify bottlenecks and propose recommendations given the limited variables that the aquarium can manipulate.

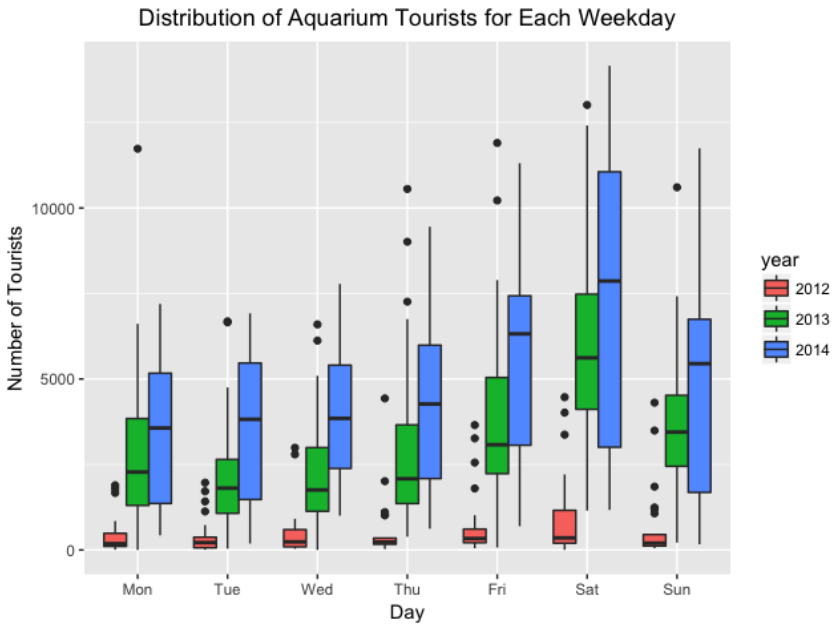

Figure 2.30 – Distribution of aquarium tourists for weekday from 2012 - 2014.

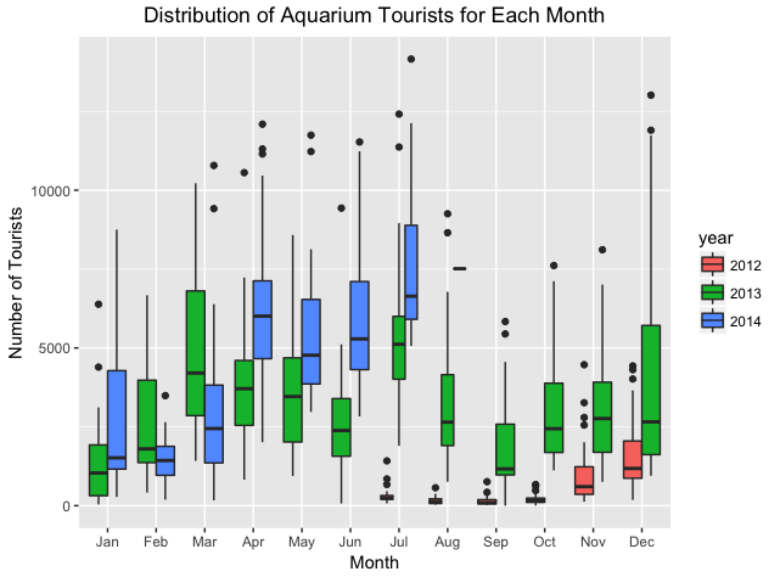

Figure 2.31 – Distribution of aquarium tourists for each month from 2012 - 2014.

2.8.1.2 Aquarium Simulation Settings

To investigate the limit of the aquarium, we simulate the scenario with a total of 14,156 guests entering throughout the day. To accommodate the largest flow of people, the operating hour of the Aquarium was extended from 10am-5pm to 9am-9pm and number of the Dolphin show was increased from twice a day to four times a day. In our simulation, four scenarios were implemented. The first scenario represents the real situation of the busiest day of July 2014. In this scenario, the Dolphin show commences at 11:00am, 1:30pm, 3:30pm, and 5:30pm. The second, third and fourth scenarios only differ in the time of dolphin shows compared to the first. In the second scenario, the time of dolphin show is at 11:30am, 1:30pm, 4:00pm and 5:30pm. In the third scenario, the time is at 10:00am, 12:00pm, 3:30pm and 5:30pm. And in the fourth scenario, the time is at 10:00am, 11:40am, 3:30pm and 5:30pm. By implementing these simulations, we seek to explore the effect brought by the change the time of Dolphin and investigate its impact on the overall logistics and tourists' experience. Figure 2.32 describes the guests' cognitive decision procedure of entertaining themselves in the aquarium. Figure 2.33 illustrates the layout and POI placement of the simulation.

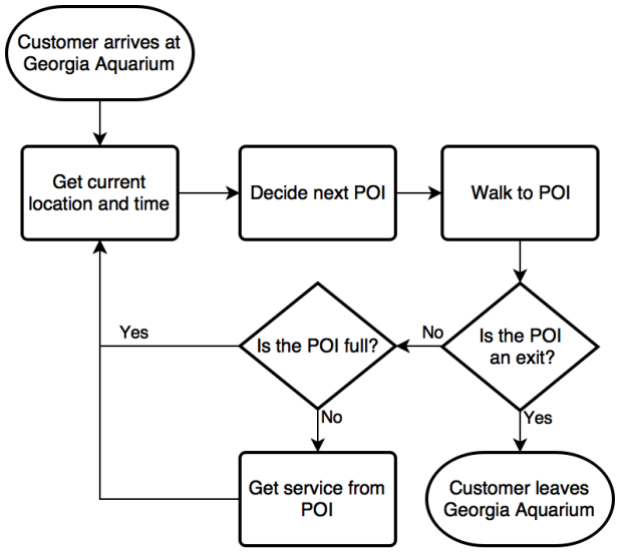

Figure 2.32 – Tourists' logistic planning in Georgia Aquarium.

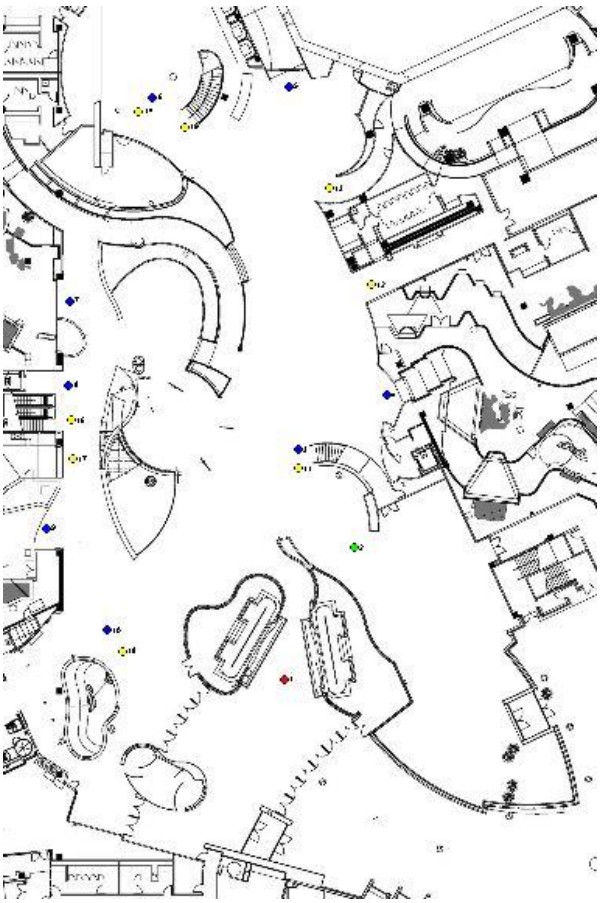

Figure 2.33 – Layout of the simulation of Georgia Aquarium.

2.8.1.3 Aquarium Simulation Result

The number of people inside the aquarium rises fast in the morning and reaches maximum around 11:30am. After dropping to a low point round 2:00 pm, the number of people rises again around 4:00pm. While the general shapes of the four distributions share a high degree of similarity, scenario 2-4 are showing a decreased maximal number around 11:30pm in contrast to the first scenario (Figure 2.34). The exact amount of decreases is as follow: the second scenario, 488; the third scenario, 427; the fourth scenario, 551.

Additionally, all the alternative scenarios show delayed increase of people in waking area, while scenario 3 and 4 show significant decrease around 11:45am (Figure 2.35). A decrease of the maximum number of people inside the facility indicates better guest experience and a less severe situation of emergency response. The four scenarios with various Dolphin show's time had no significant impact on the attendance of POIs except for the Dolphin show itself (Table 2.3). The number of tourists for the Dolphin show decreased by 237, 702 and 404 for the second, third and fourth scenario, respectively.

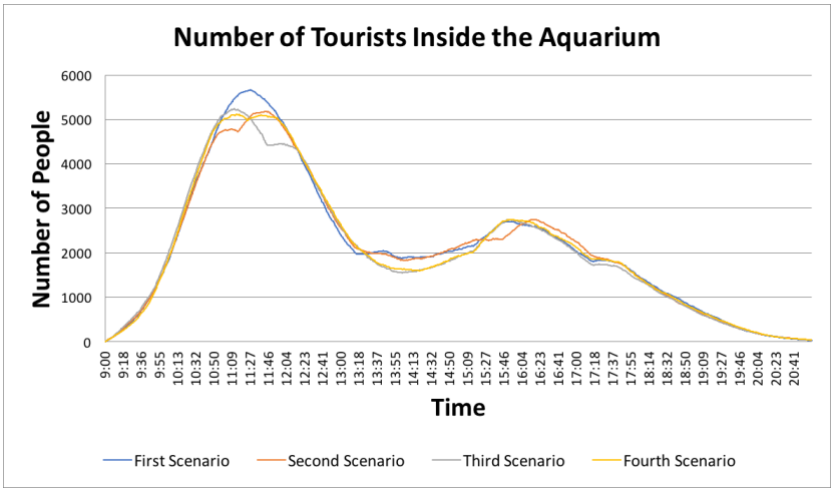

Figure 2.34 – Number of tourists inside the aquarium. The second, third and fourth scenarios are all showing a decreased maximal number compared with the first scenario around 11:30am. The reduction implies an improvement of the tourists' experience.

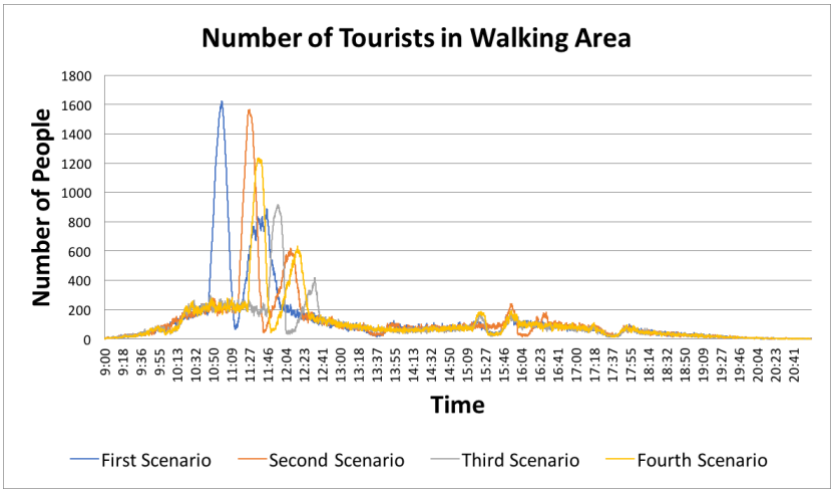

Figure 2.35 – Number of guests in the walking area.

Table 2.3 – Attendance in percentage of total tourists. The attendance of all POIs is calculated as a percentage of total tourists. A Chi-square test is performed to measure if there is a difference across the four scenarios. The attendance of Dolphin show shows a significant decrease of attendance as the scenario was changed from the original one.

	First Scenario	Second Scenario	Third Scenario	Fourth Scenario	Chi-square test p-value
Monsters	74.77%	74.03%	73.92%	74.14%	0.352031176
Tropical Divers	86.68%	86.75%	86.93%	86.73%	0.933176856
Ocean Voyager	80.50%	80.28%	79.97%	80.18%	0.728482098
Cafe	74.59%	74.66%	74.06%	74.19%	0.587535606
Coldwater Quest	89.86%	89.29%	89.27%	89.23%	0.267780112
Dolphin Show	55.19%	53.52%	50.23%	52.34%	5.75184E-16
River Scout	85.48%	85.61%	85.31%	85.45%	0.912190999

Georgia Explorer	80.47%	80.62%	80.83%	80.16%	0.541064776

Besides the fluctuation in admission, the drastic changes of people in POIs also pose a challenge to the operation management. As Figure 2.36 indicates, due to the limited access and high popularity, Dolphin Tale attracts more than half of all people in the facility with some of the POIs being almost emptied. Afterwards, a large amount of people pours out when the show is concluded and cause serious congestions to the walking area and other POIs immediately. For example, in Figure 2.36 scenario 1, the number of tourists of Ocean Voyager increased dramatically as outgoing people of Dolphin Tale entered it. In the second scenario, the postponed Dolphin Tale successfully reduced the maximum number of Ocean Voyager from 1271 to 1173. Placing the third Dolphin Tale in the second scenario at 4:00pm instead of at 3:30pm reduced the number of guests of the fourth dolphin show. In the third and fourth scenarios, we place two shows in the morning. The fourth scenario is better than the third one in two aspects. First, the percentage of participation in dolphin show was higher. Second, the maximal number of tourists of Ocean Voyager is not only lower, but also kept at maximum for a very short time instead forming a plateau as in the third scenario (Figure 2.36, third and fourth scenarios). In conclusion, to ensure a high participation of Dolphin Tale, it is critical to ensure at least a two-hour gap between sessions. To improve customer's experience and reduce the risk associated with large crowd, mitigation of traffic could be achieved by rescheduling the overlap of flow leaving Dolphin Tale and the flow from admission. We argue that the fourth scenario is the best implementation because of overall balanced pressure on the facility and high guest

participation. Though, the fourth scenario comes at a cost of lower participation in the dolphin show compared to the original situation (Figure 2.41, less 366 people), it reduces the maximal number of people in the facility, the walking area, and POIs (Figure 2.37, Figure 2.38, Figure 2.39, Figure 2.40). Meanwhile, it reduces the blocking of entrances of other POIs when people line up to attend the dolphin show.

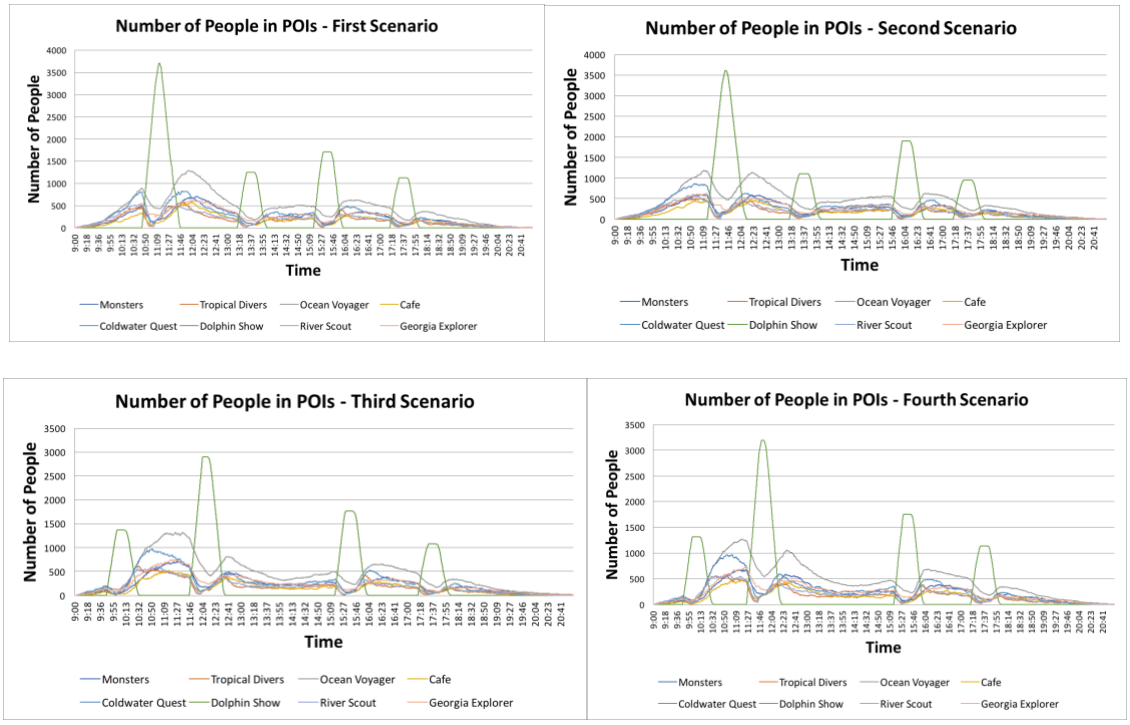

Figure 2.36 – Number of tourists of POIs over time of the first scenario.

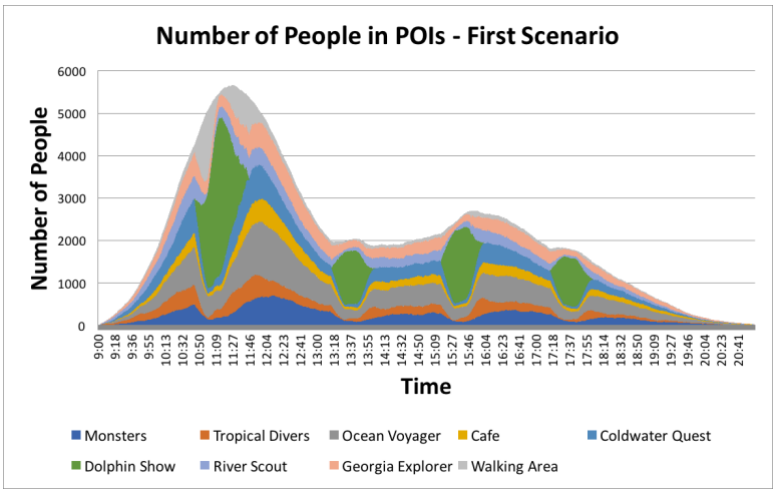

Figure 2.37 – Stacked number of tourists of POIs over time of the first scenario.

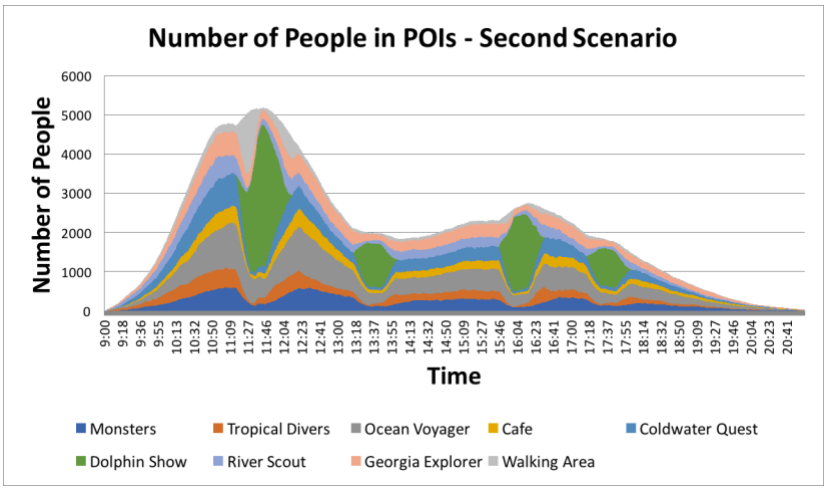

Figure 2.38 – Stacked number of tourists of POIs over time of the second scenario.

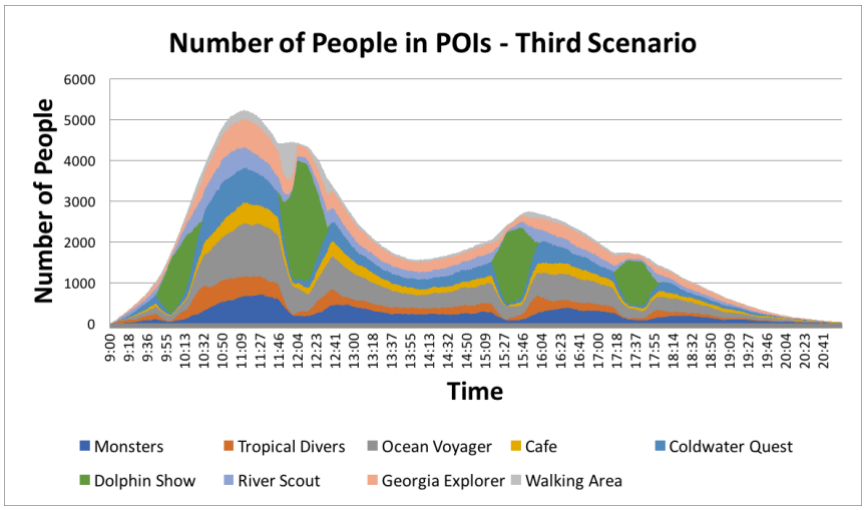

Figure 2.39 – Stacked number of tourists of POIs over time of the third scenario.

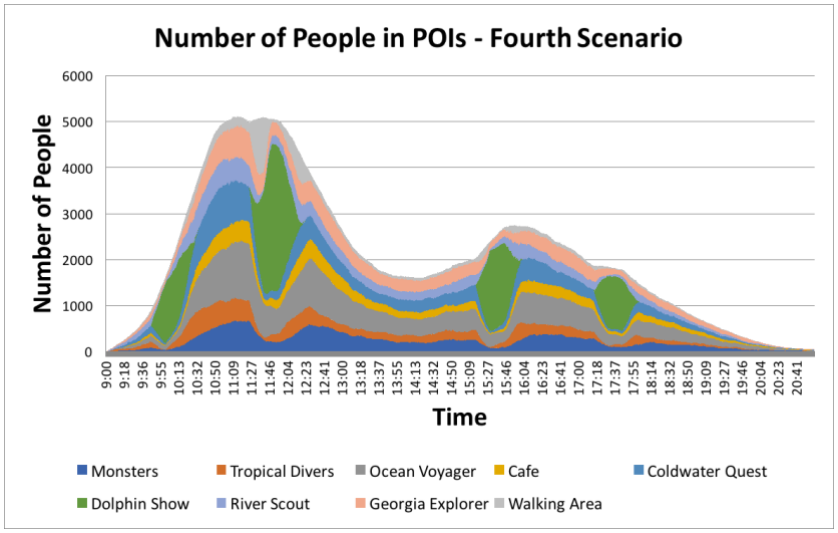

Figure 2.40 – Stacked number of tourists of POIs over time of the fourth scenario.

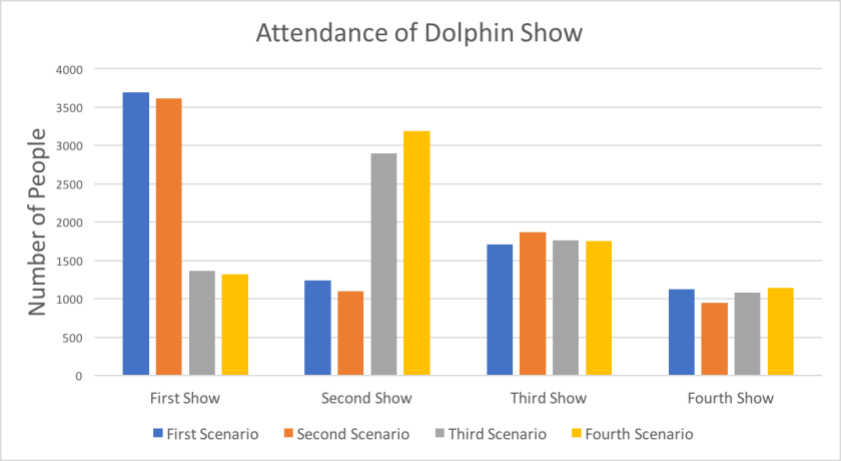

Figure 2.41 – Attendance of Dolphin show in four scenarios.

2.8.1.4 Group Formation

Group formation is visualized as an option during simulation. The line between two agents indicating a lead-follow relationship, in which darker end of the line connects leader, and lighter end connects follower (Figure 2.42).

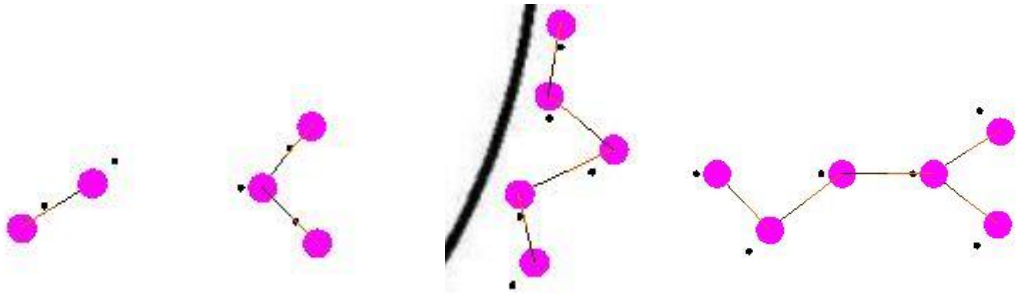

Figure 2.42 – Group formation in Georgia Aquarium simulation

2.8.2 Bobby Dodd Stadium of Georgia Tech

2.8.2.1 Data Collection and Motivation

With the objective to understand the safety and operation status of the stadium during game season, our team conducted the time motion study in collaboration with Bobby Dodd Stadium from 2014-2015. We collected the interarrival data for all audiences at all gates and started the recording from the beginning of admission till game starts. We also recorded the time spent in ticket scanning and security check. The number of guests is summarized in Table A.1 for all 7 games. The breakdown of number of attendance of gates (Figure 2.43, Figure A.4) shows gate 4 and gate 7 handle much more audiences than the rest. The number of attendances is unevenly distributed among gates, for example, gate 4 handles as high as 26.20% while gate 6 only handles 0.89%. To provide a data for a system model that could realistically capture the guest movement, and scenario characteristics, we also collected the location and number of guests at all major parking spaces across campus. Bobby Dodd Stadium is a frequent choice for game event. Resource allocation (including parking and camping spaces), traffic mitigation and security screening remain as the largest challenges given the significant scale of the event. Our goal is to identify the bottlenecks in the guest admission process, understand the reason for suboptimal performance in operations and increase logistical and operational efficiencies.

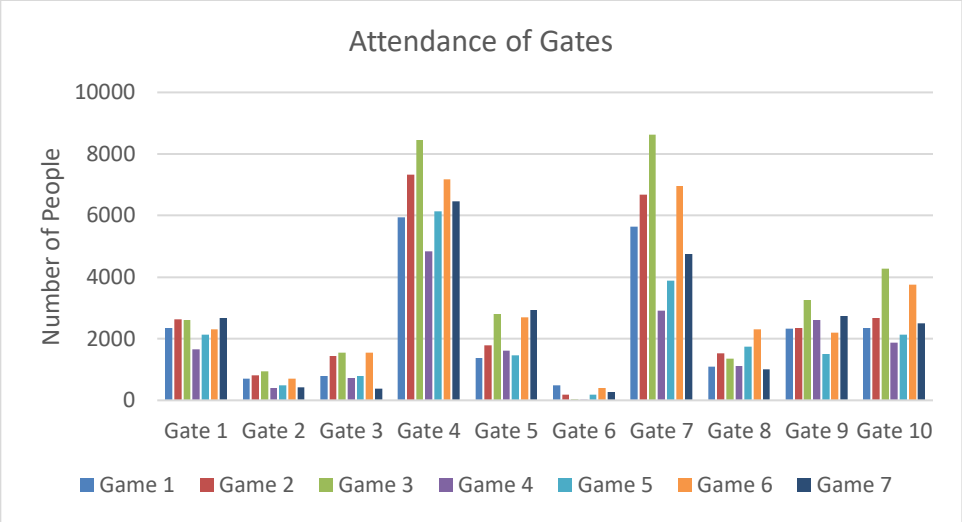

Figure 2.43 – Number of attendances of all gates for the seven games.

2.8.2.2 Simulation and Analysis

Two simulation models are implemented. To reveal the reason of the unbalanced distribution of admission data and capture the comprehensive profile of audiences, we implement a simulation in which the flows of pedestrians are modelled moving from the scattered parking spaces to the stadium. In the simulation, guests initialize their movement from the parking spaces across the Georgia Tech campus, select optimal paths and move toward the Bobby Dodd Stadium which is on the lower right of Figure 2.44. The simulation concludes that the 1410 and 992 guests walk to the northwest and northeast corners of the stadium while only 696 and 402 guests walk to the southeast and southwest corners (Figure 2.45). *The imbalance of crowd around the north of the stadium is in consistency of the fact that gate 4 and 7 process much more audiences than the rest.*

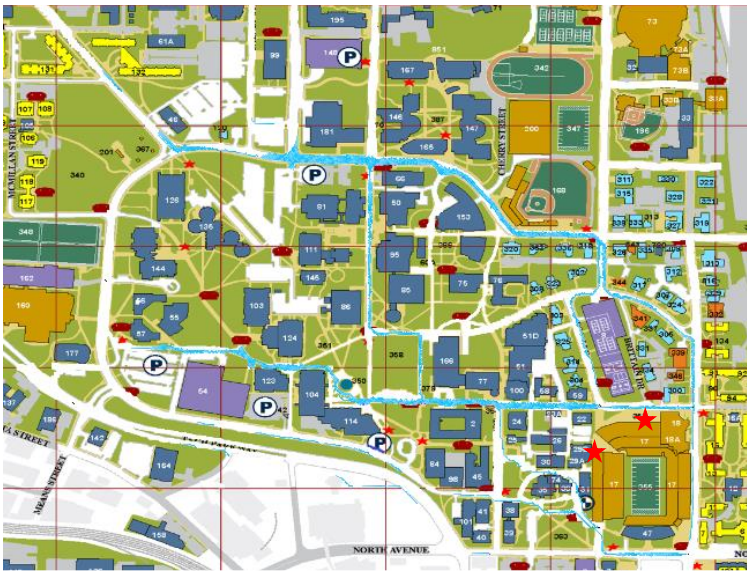

Figure 2.44 – Simulation of audiences crossing campus on route from parking spaces to the stadium.

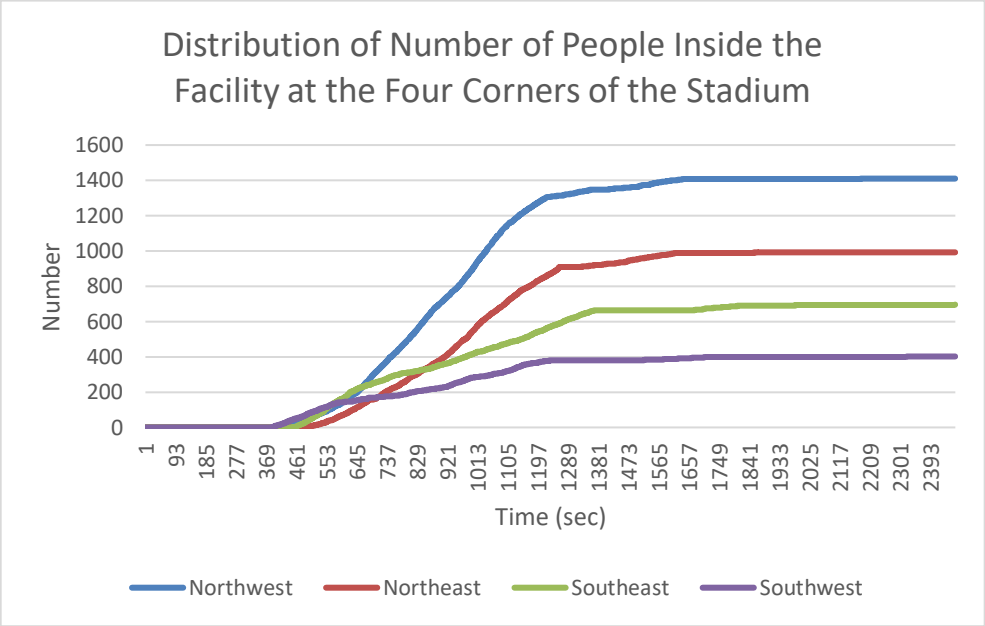

Figure 2.45 – Distribution of Number of People Inside the Facility at the Four Corners of the Stadium.

Figure 2.46 illustrates the logistical planning of guests to enter the game via ticket scanning and security check. In our second simulation (Figure 2.47), a total of 20,821 guests enter the stadium through all gates distributed as in Table A.2. We approximate the arrival time using multiple polynomial formulas for all gates (Table A.3).

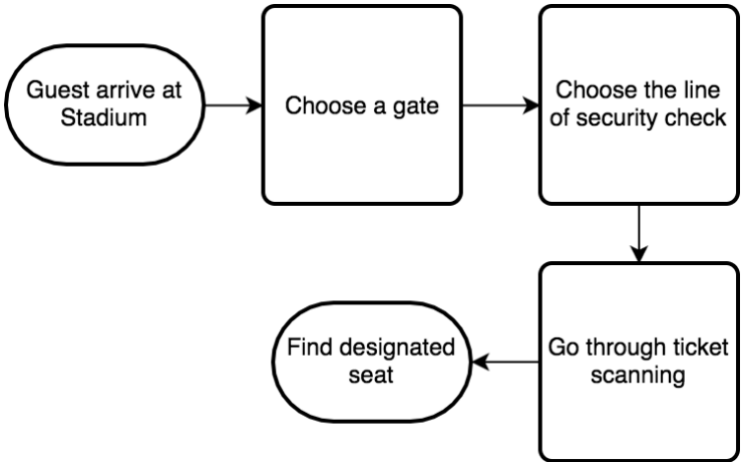

Figure 2.46 – Logistic planning of guests attending football event.

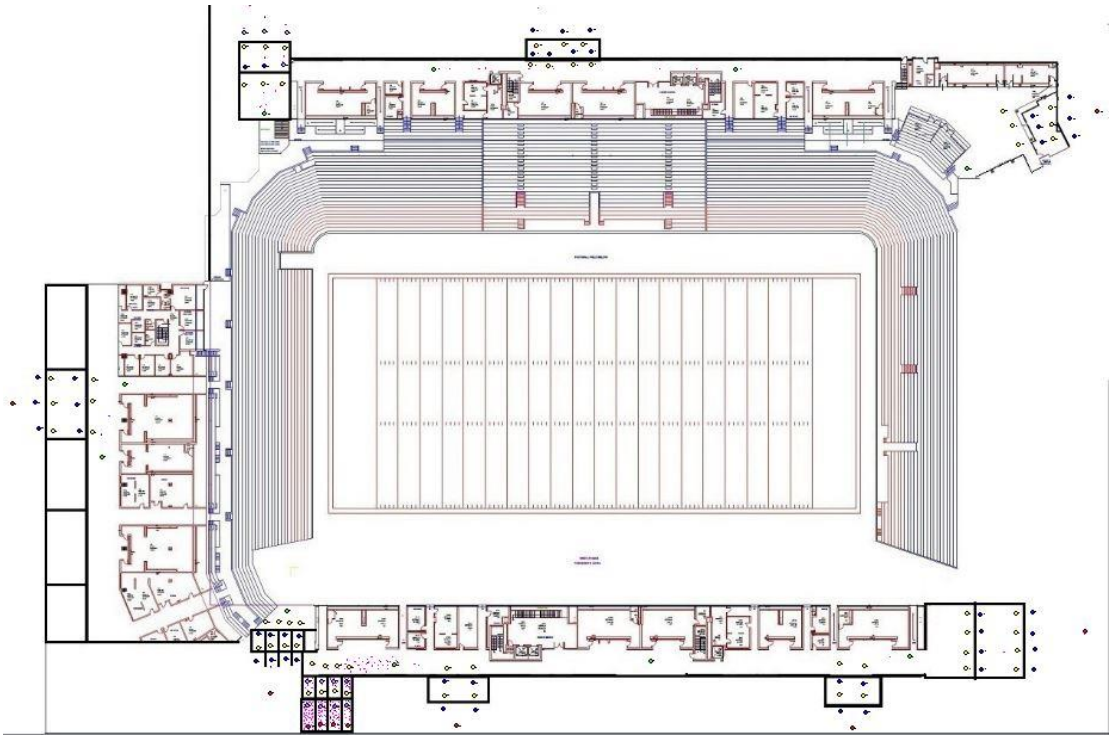

Figure 2.47 – Simulation of ticket admission of Bobby Dodd Stadium.

Simulation of the original scenario indicates prolonged delay of admission and high congestion outside gate 4 and 7. Given the fact that the staff at the gates have to process highly imbalanced number of guests, the resources of other gates are wasted due to low utilization. This situation leads to longer admission time, serious congestion at certain gates and safety risk to the crowd. To address the above issues, we propose that redistribution of guests evenly across all gates will improve the efficiency of operation and reduce negative experience due to long waiting. Four simulation scenarios have been created with a series of increasing levels of balanced redistribution of people across gates (Figure 2.48). Figure 2.49 illustrates that redistribution of guests significantly decrease the number of people waiting in the admission phase. Specifically, 50%, 80% and 100% balanced scenarios achieve 23.64%, 48.02%, 67.83% decrease in the number of guests in queue, respectively. The imbalanced distribution of guests is a collective result of the inconvenient placement

of parking space, lack of familiarity of the campus and herd behavior. Based on the simulation results, we made the following recommendations: 1) Strategies to provide more parking space at the south and east sides of the stadium, 2) More personnel or signs on the road that distribute the guests to utilize gates with availability, 3) Dynamic relocation of security and ticket scanning personnel between gates according to the need of the situation.

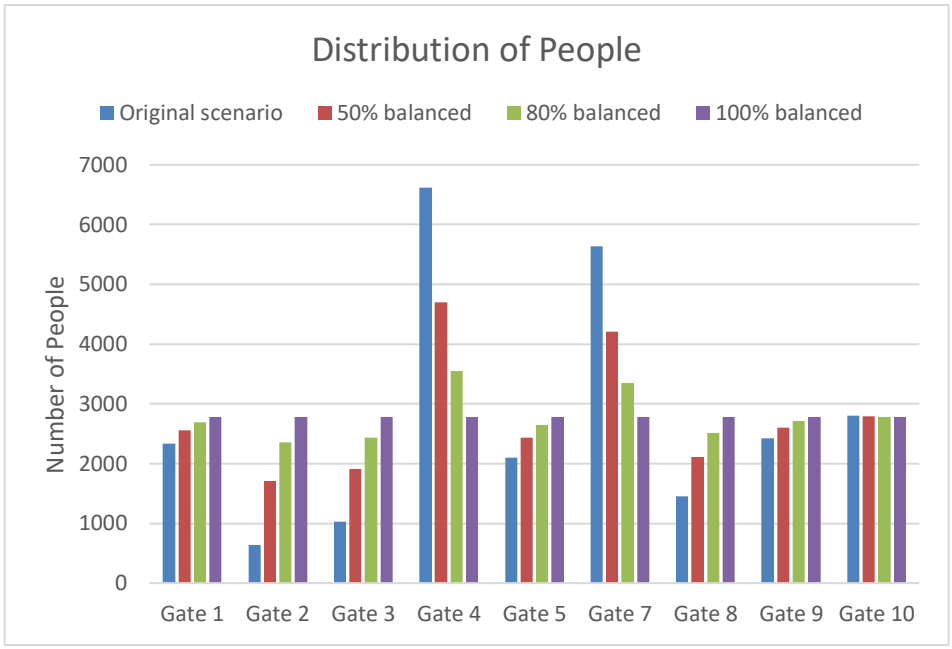

Figure 2.48 – Four scenarios of simulation with different level of redistribution for balance.

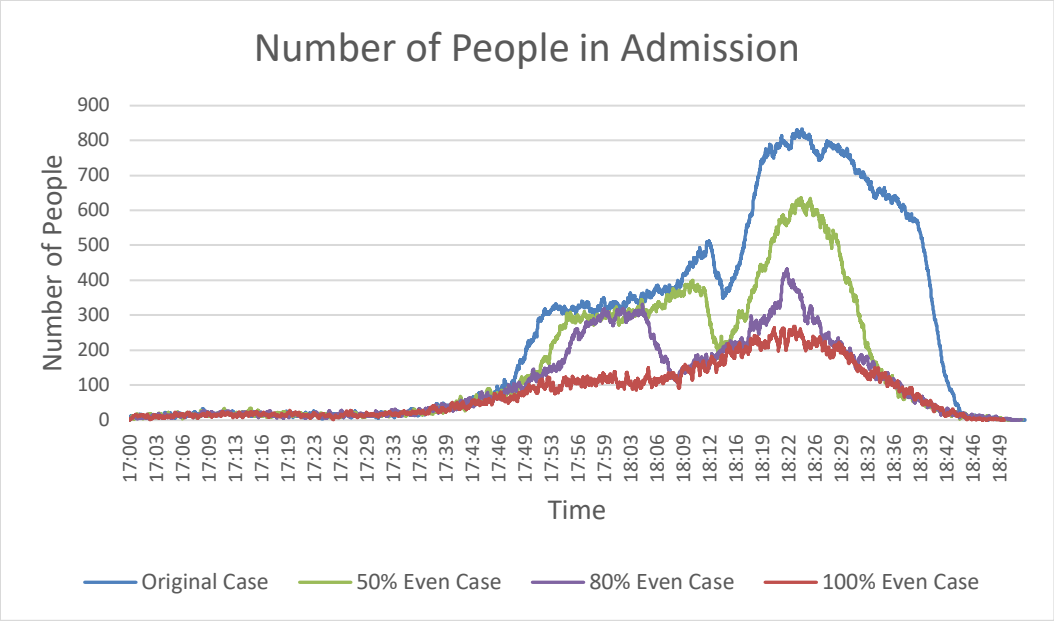

Figure 2.49 – Number of people in admission procedure with 4 levels of evening.

2.8.3 Additional Cases Study in Appendix A

2.9 Conclusion

Large scale traffic mitigation, logistical planning, facility design, information propagation, and evacuation validation have driven the need for realistic modelling techniques. Advances in computational capacity empowered the popularity of agent-based simulation in areas where equation-based model or discrete event simulation were the primary methodologies. To advance the technologies of agent-based simulation, we introduce a series of improvements on algorithms, modelling and concept.

In this study, we propose new implementations on four aspects, including path planning, collision avoidance, emotion modeling and optimization with simulation and present a complete simulation platform for customer's use. First, we introduce the Flood Theta* algorithm, an any-angle path planning algorithm on a grid environment. We

introduce and benchmark three mechanisms to improve the performance of the algorithm, which are Deep Looking, Larger Neighbor Looking and Close-Child policy. Deep Looking and Larger Neighbor Looking significantly reduce the path length, but at a cost of increased computational time. We argue that a trade-off should be made based on the actual scenario of application. Flood algorithm with priority queue could be further improved if integrated with the mechanism of boundary checking. Boundary check ensure that the algorithm only updates the cells that are immediately adjacent to unprocessed cells. We introduce the Projection Based Interactive Velocity Avoidance Model. The model adopts the simplicity of social force model, which requiring no optimization. The unique placement of divergent velocity makes the movement of agents more realistic. In the demonstration of the model in four scenarios where social force model fails, lane formation, smooth cross of intersection and antipodal movement are observed. We implement emotion modeling with classic personality and emotion model based on psychology. We also introduce the emotion contagion model that transmit emotions between agents in vicinity via interaction, determined by the expressiveness and openness of both parties. Additionally, we propose and integrate an optimization component in the simulation platform, using deep neural network. The platform is applied in cases studies in collaboration with Georgia Aquarium, the Georgia Tech Police and Emergency Response team. In the case study, bottlenecks in current logistical operation is identified with simulation and recommendation and improvement are proposed. Results from the simulation demonstrate reduction in congestion, mitigation in traffic and improvement in overall operation time. In the future, we plan to increase the representation of individual's feature, including expression, body

shape, and expand its application in a range of domains, such as city-scale event simulation, emergency evacuation in public venues and biological system simulation.

CHAPTER 3 INVESTIGATING A NEEDLE-BASED EPIDURAL PROCEDURE IN OBSTETRIC ANESTHESIA

3.1 Abstract

This study investigates the safety and efficacy of a large-dose, needle-based epidural technique in obstetric anesthesia. The technique differs from a standard, catheter-based approach in that the anesthetic dose is administered through an epidural needle prior to insertion of the epidural catheter. Using a data-driven informatics and machine learning approach, our findings show that the needle-based technique is faster and more dose-effective in achieving sensory level. We also find that injecting large doses in the epidural space through the epidural needle is safe, with complication rates similar to those reported in published literature for catheter-based technique. Further, machine learning reveals that if the needle dose is kept under 18 ml, the resulting hypotension rate will be significantly lower than published results. The machine learning framework can predict the incidence of hypotension with 85% accuracy. The findings from this investigation facilitate delivery improvement and establish an improved clinical practice guideline for training and for dissemination of safe practice.

3.2 Introduction

The potential consequences of failed or misplaced epidural needles are well known to obstetric anesthesiologists. A well-documented epidural complication, a “wet tap”, results in a headache and possible total spinal anesthesia/block, requiring immediate maintenance of the patient’s airway and blood pressure. The inadvertent intravenous injection of local anesthetic into a vein in the epidural space leads to seizures and fatal

cardiac arrhythmias. Equally worrisome is the inadequate epidural block leading to complications during a caesarian section. These complications include an emergency general anesthetic, resulting in airway loss, hypoxemia, hypercarbia and death [142-144]. However, to date, limited research has been performed regarding standardization of the epidural analgesia procedure to avoid practice variance with minimal complications.

Traditionally, the epidural catheter is placed, aspirated, and a test dose of medication is given to detect the possibility of an intravascular (IV) or intrathecal (IT) catheter prior to administering additional doses of local anesthetic and opioids. More rapid injection is often possible through the epidural needle given the relatively larger gauge and shorter length compared to a catheter [145], which could potentially enhance the spread of medication within the epidural space. However, there have been very few studies in which anesthesia providers have initiated labor analgesia by injecting medications through the epidural needle immediately after loss of resistance in order to achieve faster onset of pain relief [146]. The rationale for potentially improved analgesia onset with epidural needle injection is uncertain. In addition to faster onset of analgesia, it has been reported that dosing through the epidural needle may result in improved quality of epidural anesthesia compared to dosing through the catheter [147]. However, other investigations in obstetric [148] and non-obstetric [149] patients receiving epidural anesthesia have observed similar onset and quality of surgical anesthesia as well as similar level of sensory blockade when dosing through the needle versus the catheter. In a small double-blinded prospective investigation (n=60), G. Ristev et al. 2017 [150] directly compared needle and catheter injection of epidural medications for the initiation of labor analgesia. Their results observed that epidural needle and catheter injection of medications result in similar onset of

analgesia and sensory blockade, quality of labor analgesia, patient satisfaction, and complication rates. To date little is known regarding practice and patient outcome related to large doses of local anesthetic injected through the epidural needle.

In this paper, we perform an in-depth study of epidural process to capture practice variance and quantify the time and dose required to achieve the desired sensory level. In particular, using a data-driven and machine learning approach, we establish a safe and quickly effective epidural dose that can be administered through the epidural needle prior to the insertion of the epidural catheter. Based on clinical results, we quantify complications for doses as large as 20 ml that is injected through the epidural needle. We contrast the proficiency of physician practice and provide insights on their preference in medication and dosage. Understanding the causes and effects of such variation can help providers avoid practices that negatively impact outcomes. The machine learning analysis reveals practice characteristics that result in the best outcome with the least complications. Our findings facilitate establishment of improved clinical practice guidelines (CPG) for care outcome and delivery improvement.

3.3 Materials and Methods

This study employs a broad range of informatics techniques to facilitate improvement in patient care. It aims to capture practice variance, quantify dose-sensory achievement characteristics, and evaluate the safety and utility of injecting large doses (up to 20 ml) in the epidural space through the epidural needle for elective caesarian sections in the hands of experienced anesthesiologists at a large urban obstetric hospital. The study involves five major steps: 1) Develop process maps of patient and epidural service

workflow via objective process observations and structured interviews. 2) Perform time-motion studies of epidural processes, record complications and practice variance, and analyze hospital data. 3) Perform statistical analysis of collected data, conduct system analysis on practice variance, quantify effective dose-sensory level achievement, 4) Develop a machine-learning predictive analytic model to predict patient/outcome characteristics. 5) Develop a computerized simulation-optimization system to simulate current performance, optimize systems and estimate anticipated global improvement. 6) Report findings and establish practice guideline recommendations for improved quality of care.

3.3.1 Epidural Workflow and Services

Figure 3.1 summarizes the epidural process performed by anesthesiologists observed by medical informaticians and engineers. The green denotes practice variance that we observed. Anesthesiologists choose one of three basic techniques of loss of resistance (or a combination thereof) to identify the proper epidural space: air, saline and local anesthetic. Medication dosages vary by providers with most injecting as much as 20 ml through the epidural needle prior to inserting the epidural catheter.

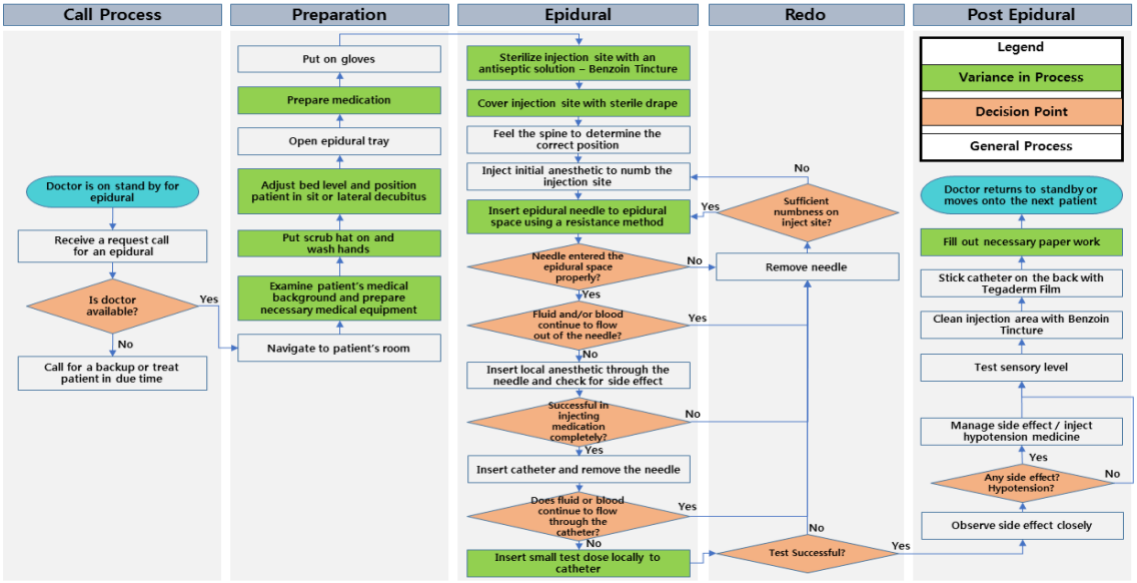

Figure 3.1 – This figure summarizes the anesthesiologist epidural procedure workflow process. Green highlights those processes with variance among providers.

3.3.2 Observations, Time-Motion Studies, and Chart Review

From January 2014 through December 2014, eight trained observers collected epidural process data via a standardized checklist through shadowing of the epidural team. Data collected includes patient demographics, vital signs, medication type and dosage, time to achieve sensory level, outcomes and response to medication. The observers simultaneously conducted time-motion studies, and measured service time for each step of the epidural workflow. Variability of practitioners and processes were also captured. In addition to observation, a random sample of electronic medical record (EMR) was gathered and reviewed to serve as a validation set for our machine learning and system simulation-optimization analysis. Two types of epidural approaches were defined based upon the primary delivery mechanism of the majority dose. If the majority of the dose is delivered through a needle, it is defined as a needle-based approach. Likewise, a catheter-based approach delivers the primary dose through a catheter.

3.3.3 Statistical Analysis

Statistical analysis was conducted to quantify variations and their associated outcome. Specifically, variations on delivery types, complications caused by delivery types, time to sensory level, medications and dosage, epidural approaches (needle-based versus catheter-based), and practitioner performance were noted.

Statistical analyses were performed using MATLAB [151]. Statistical significance was assessed at the 0.05 level unless otherwise noted. Descriptive statistics were calculated for all variables of interest including median and 25th to 75th percentiles, and counts and percentages when appropriate. Two-sample t-test and Wilcoxon rank-sum tests were used to compare continuous variables between groups and Chi-square tests were used for comparing categorical variables between groups.

Next, a machine learning predictive framework was designed to uncover key factors that influence and predict hypotension. Specifically, we used discriminant analysis via mixed integer program (DAMIP) as our classifier [152, 153] and contrasted its performance to other popular classification methods.

3.3.4 Machine-Learning Predictive Analytic Framework: Discriminant Analysis via Mixed Integer Program (DAMIP)

Suppose we have n entities from K groups with m features. Let $\boldsymbol{\mathcal{G}} = \{1, 2, \dots, K\}$ be the group index set, $\boldsymbol{\mathcal{O}} = \{1, 2, \dots, n\}$ be the entity index set, and $\boldsymbol{\mathcal{F}} = \{1, 2, \dots, m\}$ be the feature index set. Also, let $\boldsymbol{\mathcal{O}}_k$, $k \in \boldsymbol{\mathcal{G}}$ and $\boldsymbol{\mathcal{O}}_k \subseteq \boldsymbol{\mathcal{O}}$, be the entity set which belong to group k. Moreover, let $\boldsymbol{\mathcal{F}}_j$, $j \in \boldsymbol{\mathcal{F}}$, be the domain of feature j, which could be the space of

real, integer, or binary values. The i th entity, $i \in \boldsymbol{\mathcal{O}}$, is represented as $(y_i, \boldsymbol{x}_i) = (y_i, x_{i1}, \dots, x_{im}) \in \boldsymbol{\mathcal{G}} \times \boldsymbol{\mathcal{F}}_1 \times \cdots \times \boldsymbol{\mathcal{F}}_m$, where y_i is the group to which entity i belongs, and $(x_{i1}, \dots, x_{im})$ is the feature vector of entity i. The classification model finds a function $f: (\boldsymbol{\mathcal{F}}_1 \times \cdots \times \boldsymbol{\mathcal{F}}_m) \to \boldsymbol{\mathcal{G}}$ to classify entities into groups based on a selected set of features.

Let π_k be the prior probability of group k and $f_k(\boldsymbol{x})$ be the conditional probability density function for the entity $\boldsymbol{x} \in \mathbb{R}^m$ of group k, $k \in \boldsymbol{\mathcal{G}}$. Also let $\alpha_{hk} \in (0,1)$, $h, k \in \boldsymbol{\mathcal{G}}, h \neq k$, be the upperbound for the misclassification percentage that group h entities are misclassified into group k. DAMIP seeks a partition $\{P_0, P_1, \dots, P_K\}$ of $\mathbb{R}^K$, where P_k , $k \in \boldsymbol{\mathcal{G}}$, is the region for group k, and P_0 is the reserved judgement region with entities for which group assignment are reserved (for potential further exploration).

Let u_{ki} be a 0/1 variable to denote if entity i is classified to group k or not. Mathematically, DAMIP [152, 154-156] can be formulated as

$$\text{Max} \quad \sum_{i \in \mathcal{O}} u_{y_i i} \tag{3.1}$$

$$\text{s.t.} \quad L_{ki} = \pi_k f_k(\boldsymbol{x}_i) - \sum_{h \in \boldsymbol{\mathcal{G}}, h \neq k} f_h(\boldsymbol{x}_i) \lambda_{hk} \qquad \forall\, i \in \boldsymbol{\mathcal{O}}, k \in \boldsymbol{\mathcal{G}} \tag{3.2}$$

$$u_{ki} = \begin{cases} 1 & \text{if } k = \arg\max\{0, L_{hi} : h \in \boldsymbol{\mathcal{G}}\} \\ 0 & otherwise \end{cases} \qquad \forall\, i \in \boldsymbol{\mathcal{O}}, k \in \{0\} \cup \boldsymbol{\mathcal{G}} \tag{3.3}$$

$$\sum_{k \in \{0\} \cup \boldsymbol{\mathcal{G}}} u_{ki} = 1 \qquad \forall\, i \in \boldsymbol{\mathcal{O}} \tag{3.4}$$

$$\sum_{i:\, i \in \boldsymbol{\mathcal{O}}_h} u_{ki} \leq \lfloor \alpha_{hk} n_h \rfloor \qquad \forall\, h, k \in \boldsymbol{\mathcal{G}}, h \neq k \qquad (3.5)$$

$$u_{ki} \in \{0,1\} \qquad \forall\, i \in \boldsymbol{\mathcal{O}}, k \in \{0\} \cup \boldsymbol{\mathcal{G}}$$

$$L_{ki} \text{ unrestricted in sign} \qquad \forall\, i \in \boldsymbol{\mathcal{O}}, k \in \boldsymbol{\mathcal{G}}$$

$$\lambda_{hk} \geq 0 \qquad \forall\, h, k \in \boldsymbol{\mathcal{G}}, h \neq k$$

DAMIP has many appealing characteristics including: 1) the resulting classification rule is strongly universally consistent, given that the Bayes optimal rule for classification is known [157, 158], 2) the misclassification rates using the DAMIP method are consistently lower than other classification approaches in both simulated data and real-world data; 3) the DAMIP classifiers appear to be insensitive to the choice of prior probabilities, yet capable of reducing misclassification rates when the number of training entities from each group is different; 4) the DAMIP model generates robust classification rules on imbalanced data, regardless of the proportions of training entities from each group [153, 157, 159].

In this study, the entities correspond to the patients. The features are patient demographics, health conditions and clinical history, epidural workflow (processes, medication, and dosage), and provider experience and delivery characteristics. The goal is to undercover discriminatory features that can predict which patients will have a higher likelihood for complications. Ten-fold cross-validation is performed on the training set to obtain an unbiased estimate. To gauge the predictive power of the rule, we perform blind

prediction on an independent set of subjects. We compared the performance of DAMIP against well-known classifiers: classification tree, logistic regression, Naive Bayes, random forest k-nearest neighbors, and support vector machine.

3.3.5 Development of a Computerized Simulation-Optimization System

A computer simulation-optimization model was then established as a framework for modeling and optimizing the entire epidural workflow. This allows for development of improved CPGs. Parameters in the simulation include the entire epidural workflow as shown in Figure 3.1. The model captures delivery characteristics, service time, types and probabilities for each provider; response, risk factors, and outcome characteristics (including complication) of each patient; and overall throughput of processes. The model was fitted using the data collected from our time-motion studies and observations to simulate the annual hospital patient visits and treatment performance. The computer simulation model captures practice variations statistically, and allows us to investigate improvement strategies. We first fine-tuned the model to reflect the hospital regular performance. Then using the validation set from chart review, we further fine-tuned and cross-validated the accuracy of our model. The system was then optimized to identify areas of improvement.

3.4 Results

Northside Hospital delivers the highest number of newborns in the United States (the Centers for Medicare & Medicaid Services). During the study period, 19,651 deliveries were performed with 55.3% vaginal birth and 44.7% C-section. Among these, 75.1% received epidural analgesia. A total 750 parturition cases under routine epidural analgesia

were observed in full detail. This included 667 C-section, 76 vaginal birth, and 7 unlabeled cases. Majority of them (94%) were performed with patients in the sitting position. 60.42% of the patients received the injection of anesthesia at position L23. The observations covered 44 anesthesiologists.

The two groups of patients have similar distributions in weight ($p < 0.3138$), height ($p < 0.5784$), and weeks of pregnancy ($p < 0.3082$). The occurrence of allergies was similar (C-section group: 13.75%, vaginal birth group: 16.44%). 73.04% of the C-section patients had previous deliveries. And 29.41% of the vaginal deliveries were primigravidas. The systolic blood pressure of C-section and vaginal birth patients was similar ($p < 0.5700$). However, the diastolic pressure of vaginal birth patients (73.0714 mmHg) was lower than that of the C-section patients (78.0315 mmHg) ($p < 0.0074$).

The independent set of patients used for validation of findings consisted of 1,398 cases obtained through chart review. This included 892 C-section, 505 vaginal births, and 1 unlabeled case. This represented roughly 10% of the newborns delivered between January to September 2015.

3.4.1 Vaginal Birth and C-section

Age: It is well-documented that advancing maternal aged women are more likely to have cesarean delivery without labor [160]. The hospital data echoed this trend. The average age for the C-section group was 32.72 versus 30.77 of the vaginal birth group (*p*-value < 0.0089). The age range for vaginal birth and C-section groups are 18 – 39, and 17 – 49, respectively.

Medication: More than 40 combinations of medication are used. In vaginal birth, the most common medicine combinations are: 1. Lidocaine 2%, $NaHCO_3$, Epinephrine, Fentanyl (15.58%), 2. Lidocaine 1.5%, Ropivacaine 0.5%, Epinephrine (14.29%), 3. Lidocaine 2%, $NaHCO_3$, Epinephrine (11.69%), 4. Ropivacaine 0.5% (11.69%), 5. Lidocaine 2%, Epinephrine (10.39%). In C-section, they are: 1. Lidocaine 2%, $NaHCO_3$, Epinephrine, Fentanyl (28.98%), 2. Lidocaine 2%, $NaHCO_3$, Epinephrine (20.23%), 3. Lidocaine 2%, Epinephrine, Fentanyl (8.90%), 4. Lidocaine 2%, Epinephrine (8.61%), 5. Marcaine 0.5%, Fentanyl (5.74%). Ropivacaine is used for vaginal birth patients since Ropivacaine is less lipophilic than bupivacaine and less likely to penetrate large myelinated motor fibers, resulting in a relatively reduced motor blockade. It is preferred in vaginal birth where motor blockage is undesirable [161].

Sensory level achievement: Sensory level is an important indicator to measure the effect of anesthesia. A higher than desired anesthesia level (high block) can cause motor block, dyspnea, apnea and even loss of consciousness. Both groups achieve similar sensory level, with T4 (vaginal: 61.02%, C-section: 61.07%) and T6 (vaginal: 23.73%, C-section: 22.29%) being the most frequently achieved. However, the average time it takes to achieve sensory level between the vaginal birth and the C-section groups is significantly different (13.51 minutes versus 15.95 minutes, $p < 0.0126$).

Complications: Our observations identified six complication symptoms: hypotension, epidural replacement, wet tap, blood in the catheter/needle, high block, and nausea and vomiting. Only two of these, hypotension (11.84%) and blood in the catheter/needle (2.63%), were observed in the vaginal birth group. For C-section group, we observed the following incidence percentage: hypertension 52.32%, blood in the

catheter/needle 2.10%, epidural replaced 3.60%, wet tap 0.15%, high block 0.30% and nausea/vomit 0.45%. Since hypotension was the most common complication, we present detailed analysis on hypotension in a dedicated section.

3.4.2 C-section: Observed Group vs Independent Chart Review Group

General: The average age (32.72 vs 32.00, p = 0.0007), weight (188.73 lb. vs 183.41 lb., p = 0.0011), and height (163.63 cm vs 162.38 cm, p = 0.0035) are higher in the observation set then the validation set, but the pregnancy length is similar (38.16 weeks vs 38.31 weeks, p = 0.5353). Additionally, both systolic (127.19 mmHg vs 125.41 mmHg, p = 0.0426) and diastolic (77.90 vs 75.42, p = 0.0004) in the observed group are higher than those in the validation group.73.02% of the C-section patients in observed group had delivery before and it is 62.27% for the validation set. Hence, complication may be higher in the observed group.

Sensory level achievement: Both observed and validation groups showed similar achieved sensory level, with T4 (obs.: 61.07%, val.: 74.76%) and T6 (obs.: 22.29%, val.: 7.57%) being the most frequent ones. The average time to achieve level is 15.95 minutes in the observed group.

3.4.3 Needle-based vs Catheter-based Approach

We seek to quantify effective dose to achieve desired sensory level and evaluate the safety and utility of injecting large doses (up to 20 ml) in the epidural space through the epidural needle.

Among the 750 observed cases, 717 cases (95.6%) were needle-based and 33 cases (4.4%) were catheter-based. In the needle-based approach, in almost all cases over 90% of the dose was delivered through the needle; whereas for the catheter-based approach, an average of 60% of dose was delivered via the catheter.

Sensory level achievement: Needle-based approach achieved higher sensory level (average T4.79) than catheter-based approach (average T5.3) ($p < 0.0265$). The difference is not significant in C-section cases (average T4.79 versus T5.23, $p < 0.0841$). Figure 3.2 shows that the most frequent sensory levels are T4 (needle-based: 62.35%, catheter-based 36.36%) and T6 (needle-based: 21.80%, catheter based: 30.30%).

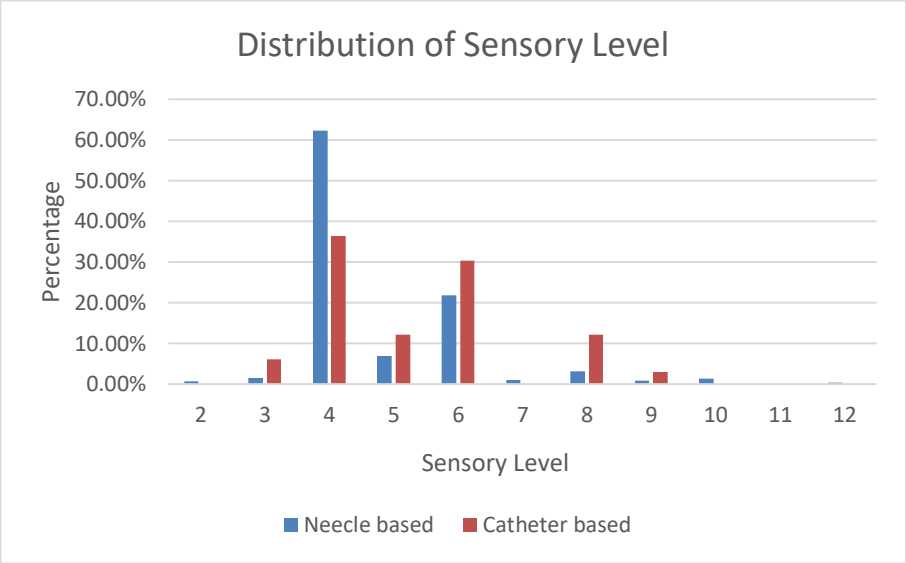

Figure 3.2 – Distribution of sensory level of needle and catheter-based approaches.

Time to achieve: The average time to achieve sensory level in needle-based approach was 15.63 minutes versus 20.00 minutes for catheter-based ($p < 0.0037$, Figure 3.3(a)). Specifically, the time difference is significant for both vaginal birth and C-section deliveries: 13.02 minutes vs 26.00 minutes for vaginal birth, $p < 0.0181$, and 15.80 minutes

vs 18.97 minutes for C-section deliveries, $p < 0.0390$. *Hence, this study reports that needle-based approach is faster and more effective in achieving the required sensory result.*

Furthermore, the needle-based approach uses less dose than catheter-based approach (mean 24.99 ml versus 30.27 ml, $p <$ 6.0e-05, Figure 3.3(b)). *These findings support that needle-based approach is more dose-effective, achieving better sensory level faster than the traditional catheter-based approach.*

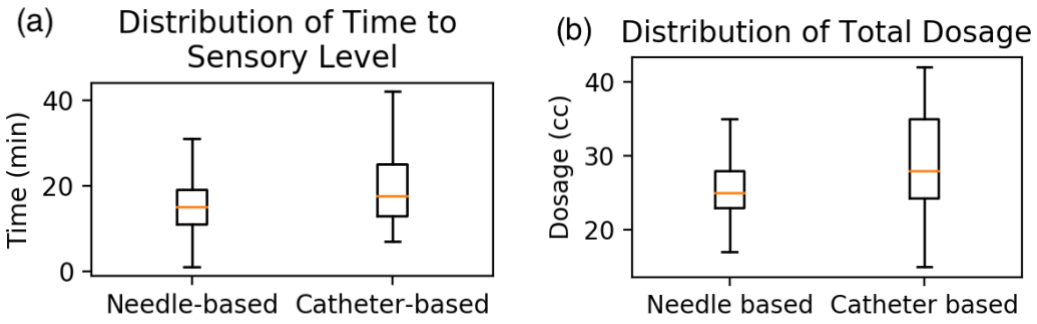

Figure 3.3 – (a) Distribution of time to sensory level, (b) Distribution of total dosage for needle vs catheter based.

3.4.4 Complications

General Statistics: We observed the following incidence percentage: hypertension 55.32%, blood in the catheter/needle 2.10%, epidural replaced 3.60%, wet tap 0.15%, high block 0.30%, faint 0.15% and nausea/vomit 0.45%. Since hypotension was the most common complication, we present detailed analysis on hypotension in a dedicated section. Table 3.1 contrasts this hospital's complication incidence to published results [162-173]. We note that these published results are all catheter-based since they did not inject dose via the epidural needles. *Compared to published results, the complication incidence of*

needle-based approach appears to be comparable to the traditional catheter-based approach.

Table 3.1 – This table contrasts the hospital's complication rate against published results.

Type of Complications	Epidural replace	Nausea/ Vomit	Wet tap	High Block	Blood in the catheter/needle	Re-do local anesthetic	Re-do loss of resistance
Known literature	4.7% - 17.8% (n=181–10995) [162-167]	1% (n=388) [168]	0.43% - 3.2% (n=141-29749) [162-165, 167-172]	0.02%-0.07% (n=10995-145550) [163, 173]	N/A	N/A	N/A
This study observed cases (n=750)	3.20%	0.40%	0.13%	0.27%	2.13%	4.00%	6.53%
This study: needle-based (n=717)	3.07%	0.42%	0.00%	0.28%	1.81%	4.04%	6.56%
This study: catheter-based (n=33)	6.06%	0.00%	3.03%	0.00%	9.09%	3.03%	6.06%

Hypotension: The most frequent complication for spinal, epidural and combined spinal and epidural anesthesia (CSE) is hypotension. Depending on different labor analgesia methods and definitions of hypotension, hypotension rates reported by previous studies can be as high as 70% [174, 175]. In this study, the reported hypotension rate was 51.73% across all approaches and delivery types. Specifically, it was 52.32% for C-section

and 11.54% for vaginal birth. The average age was 33 for the hypotension group and 32 for the non-hypotension group ($p < 0.034$).

Table 3.2 contrasts the hypotension rates of our patients to published results. We caution that since all previously reported results except one involved very small sample sizes, one can only meaningfully compare the hypotension results based on the "30% Drop of mean arterial pressure (MAP)" definition.

Table 3.2 reports the complication statistics for the observed cases. In the reporting, we do not separate the needle-based versus catheter-based cases, since statistically, there is no overall significant difference in the resulting hypotension rate (Table 3.3). To validate that the observed cases are representative of the overall hospital practice, we also report the complication statistics for the 1,398 charts reviewed. *The study reveals that the needle-based approach requires less dose for faster and effective epidural analgesia without increasing the incidence of hypotension.*

Table 3.2 – Comparison of hypotension rates.

Hypotension Definition	**Percentage and sample size from literature**		**Percentage and sample size in our study**					
			Observed cases (n=750)			**Chart Review cases (n=1398)**		
	Vaginal birth	**C-section n=107** [176]	**Vaginal birth n=76**	**C-section n=667**	**Overall n=750**	**Vaginal birth n=505**	**C-section n=892**	**Overall n=1398**
<90 mm Hg, systolic	23.1% , n = 65	16.3% [176]	17.04%	23.73%	21.62%	13.86%	23.54%	20.03%

	[177]; 4.0%, n=375 [168]							
<90 mm Hg or a 20% decrease from baseline, systolic	0%, n = 40 [178]; 5.2%, n=19 [179]	54.8% [176]	35.37%	48.91%	44.64%	33.07%	48.65%	42.99%
<100 mm Hg	7.5%, n=375 [168]	41.5% [176]	39.87%	50.66%	47.35%	38.22%	50.56%	46.14%
<100 mm Hg or >20% reduction from baseline, systolic	24%, n = 25 [180]; 48% n=25 [181]	59.3% [176]	49.20%	60.99%	57.36%	47.72%	60.65%	56.01%
<100 mm Hg or >30% reduction from baseline, systolic	9%, n = 53 [182]	46.7% [176]	40.51%	53.42%	49.45%	39.21%	53.14%	48.14%
30% Drop of MAP	N/A	46.5%, n=919 [183]	16.40%	28.53%	24.72%	13.66%	29.48%	23.75%

Table 3.3 – Comparison of hypotension for needle and catheter-based approaches.

Hypotension Standards	Overall %	% in needle-based approach	% in catheter-based approach	$\chi 2$ test statistic	P-value
<90 mm Hg, systolic	31.03%	31.55%	20.00%	1.232443	0.2669
<90 mm Hg or a 20% decrease from baseline, systolic	56.97%	61.07%	56.67%	0.091160	0.7627
<100 mm Hg, systolic	58.92%	31.55%	53.33%	4.177185	**0.0410**
<100 mm Hg or >20% reduction from baseline, systolic	72.41%	72.68%	66.67%	0.143280	0.7050
<100 mm Hg or >30% reduction from baseline, systolic	62.22%	62.48%	56.67%	0.155639	0.6932
30% Drop of MAP	38.98%	39.40%	30.00%	0.649923	0.4201

3.4.5 Uncovering Features for Predicting Hypotension

Machine learning is employed to uncover clinical and patient features that can predict hypotension. This allows for potential clinical practice guideline modification and/or early provider intervention to mitigate the effect. Our study consists of three folds. First, we used 561 observations from the first nine months (January – September 2014) and partitioned them randomly into two sets for training and blind prediction. Next, we used the established predictive rules to blind predict the future three months of 189 patients (October to December 2014). And finally, we blind predicted 1,398 patients from the period January to September 2015. This allows us to measure the accuracy in predicting status of future patients. It also sheds light on the consistency of the physicians' hypotension definition.

The inputs to the computational model consist of patient demographics, physical and allergy characteristics and overall health, weeks of pregnancy, number of redo epidurals, number of reboluses and dose, test dose, epidural needle and catheter doses, total dose, duration of injection, sensory level and time achieved, delivery type, position, medication type, and provider. Using the DAMIP machine learning algorithm, we seek to uncover a small subset of discriminatory features that can predict hypotension. DAMIP returns 27 predictive rules each achieving greater than 82% 10-fold cross-validation accuracy and greater than 85% blind prediction accuracy for predicting hypotension and non-hypotension in patients for the period January – September 2014. The discriminatory features selected include weeks of pregnancy, number of redos, epidural needle/catheter dose, number of reboluses and dosage, and patients' allergy. When blind predicting against new patients from October – December 2014, the predictive accuracy reaches 89%. Further, it reaches > 85% when blind predicting patients from January – September 2015.

Table 3.4 contrasts the performance of DAMIP against other well-known classifiers. Compared to other classifiers, we note the consistently good predictive accuracy of DAMIP in both hypotension and non-hypotension patients. The better performance of DAMIP over other classifiers may be due to the fact that its resulting classification rule is *strongly universally consistent*, given that the Bayes optimal rule for classification is known. In addition, it handles imbalanced data very well.

Identified provider practice features offer an opportunity for CPG improvement, whereas patient characteristics allow for target/personalized care intervention. In the simulation study section, we used the identified predictive rules and their associated discriminatory features to construct care / delivery redesign experiments in an attempt to reduce hypotension incidence.

Table 3.4 – DAMIP classification results for predicting hypotension and comparison against other classifiers.

Classifier	**10-fold cross validation (424 cases) unbiased prediction estimate**			**Blind Prediction on 137 cases (January – September 2014)**			**Blind Prediction on 189 cases (October – December 2014)**		
	Overall Accuracy	Hypotension	Normal	Overall Accuracy	Hypotension	Normal	Overall Accuracy	Hypotension	Normal
Classification Tree	65.60%	71.61%	51.76%	51.09%	73.85%	30.56%	59.79%	79.05%	35.71%
Logistic Regression	74.69%	88.24%	43.53%	47.45%	61.54%	34.72%	57.67%	67.62%	45.24%
Naive Bayes	73.80%	87.47%	42.35%	43.07%	78.46%	11.11%	58.20%	89.52%	19.05%
Random forest	76.83%	98.21%	27.65%	46.72%	96.92%	2.78%	56.08%	100.00%	1.19%

k-nearest neighbors	66.31%	86.19%	20.59%	38.69%	80.00%	15.28%	56.08%	86.67%	17.86%
Support vector machine	60.61%	68.29%	42.94%	49.64%	69.23%	31.94%	52.38%	72.38%	27.38%
DAMIP	**82.30%**	**82.50%**	**82.00%**	**89.00%**	**90.70%**	**87.50%**	**90.40%**	**89.20%**	**91.40%**

3.4.6 Predictive Model of Sensory Level and Time to Sensory Level for C-section

Machine learning is further applied to predict the sensory level and time to sensory level. Achieving the appropriate level of sensory blockade is critical for the C-section procedure. Dosage wrongly administered into the subarachnoid space will cause the block to extend too high up and can result in a series of side effects, including hypotension, decrease of cardiac output and loss of breath [184].

Accurate prediction could assist providers in prognosis with early determination of outcome. This will leave adequate amount of time for treatment and patient care. The prediction of sensory level herein employs 18 continuous and 19 categorical features covering the biometrics of patients, use of medicine, procedures, etc. The predictive algorithms include an optimized random forest, a deep neural network and a gradient boost regression model. The neural network and gradient boost model perform equally well with the lowest mean relative error of 0.15 - 0.16. Random forest achieves the best mean squared error of 1.59, indicating that it can handle better the diverse range in sensory level (Table 3.5).

Table 3.5 – Performance comparison of random forest, neural network and gradient boost regression in predicting sensory level. MSE: mean squared error, MAE: mean average error, MRE: mean relative error.

Dataset		Random forest	Neural network	Gradient boost
Training	MSE	1.2564	2.0033	2.1303
	MAE	0.9042	0.9204	0.8121
	MRE	0.1866	0.1687	0.1362
Test	MSE	1.5878	1.8657	2.1403
	MAE	0.9972	0.9179	0.9128
	MRE	0.1987	0.1643	0.1540

To understand the importance of factors in contributing to the sensory level achievement, we applied SHAP (SHapley Additive exPlanation) value [185] to infer individual and interactional effects. The random forest model reports that total dosage, duration of injection, weight and physicians' experience are top features that positively impact sensory level. Meanwhile, higher initial blood pressure, being overweight, and operation redo are indications of unsatisfactory sensory level (Figure 3.4).

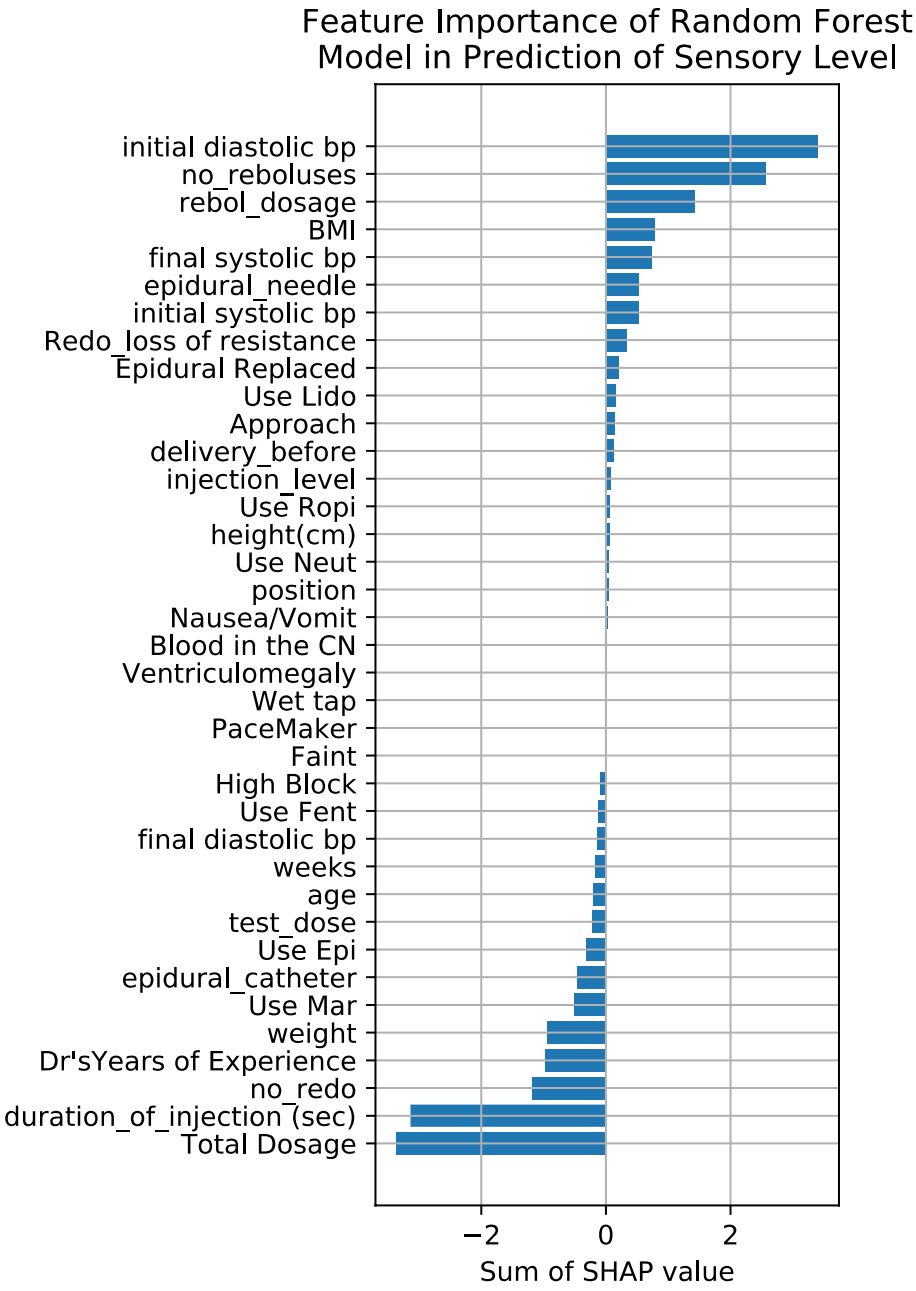

Figure 3.4 – Feature importance (SHAP value) of random forest model in the prediction of sensory level.

The effect of factors on sensory level are not monotonic. For example, initial diastolic blood pressure has zero or slightly positive effect on sensory level when within the range of 55-86 mmhg. However, when the pressure is too high (>90 mmhg) or too low

(<50 mmhg), it is significantly harder for the body to achieve the required sensory level (Figure 3.5). It is also possible to compensate the negative effect of high diastolic blood pressure by increasing the total dosage, indicated by the negative correlation when the pressure is greater than 90 mmhg. Similarly, total dosage is intuitively positive on achieving sensory level until the dosage reaches greater than 35 cc. This phenomenon represents situations where the patient's body is not responding well to the initial anesthetics and multiple reboluses have to be administered. It is worth noting that in the group with high total dosage (>35 cc), the patients are significantly taller (p = 0.0053), further confirming that height is a negative factor on sensory level achieving (Figure 3.6).

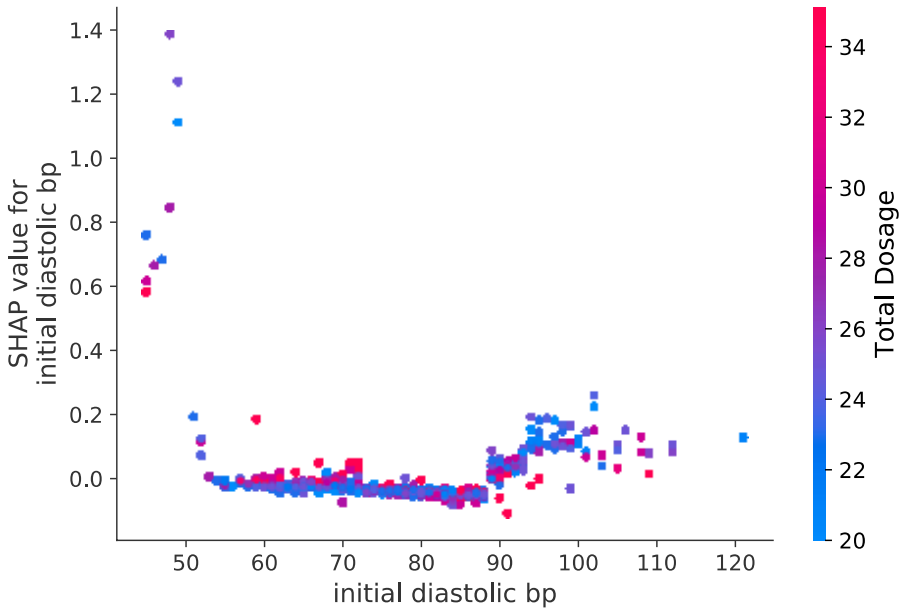

Figure 3.5 – Interaction of initial diastolic blood pressure and total dosage.

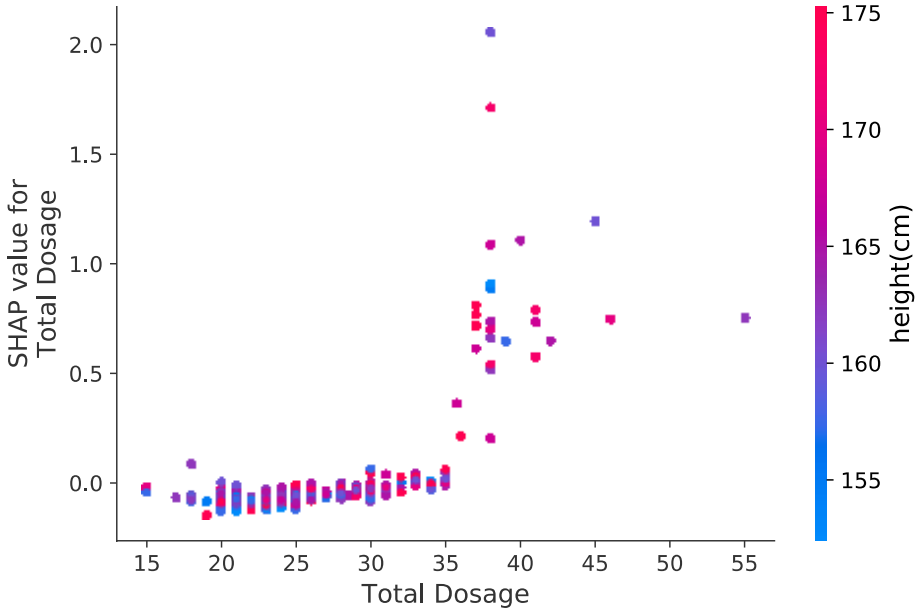

Figure 3.6 – Interaction of total dosage and height.

In the prediction of time to sensory level, the modeling algorithm includes an optimized random forest and a deep neural network. Features of the two models include biometrics, variance in procedures, outcome, side effects, and medicines. Random forest model shows that total dosage, final systolic blood pressure, doctors' experience, weeks of pregnancy, initial systolic blood pressure, catheter dosage, use of epinephrine, etc. are the top key factors in determining the time to sensory level, while the choice of medicine, delivery history and side effects are less relevant (Figure 3.7). The neural network model performs better with mean averaged error of test set at 4.32 minutes compared at 4.61 of random forest model (Table 3.6).

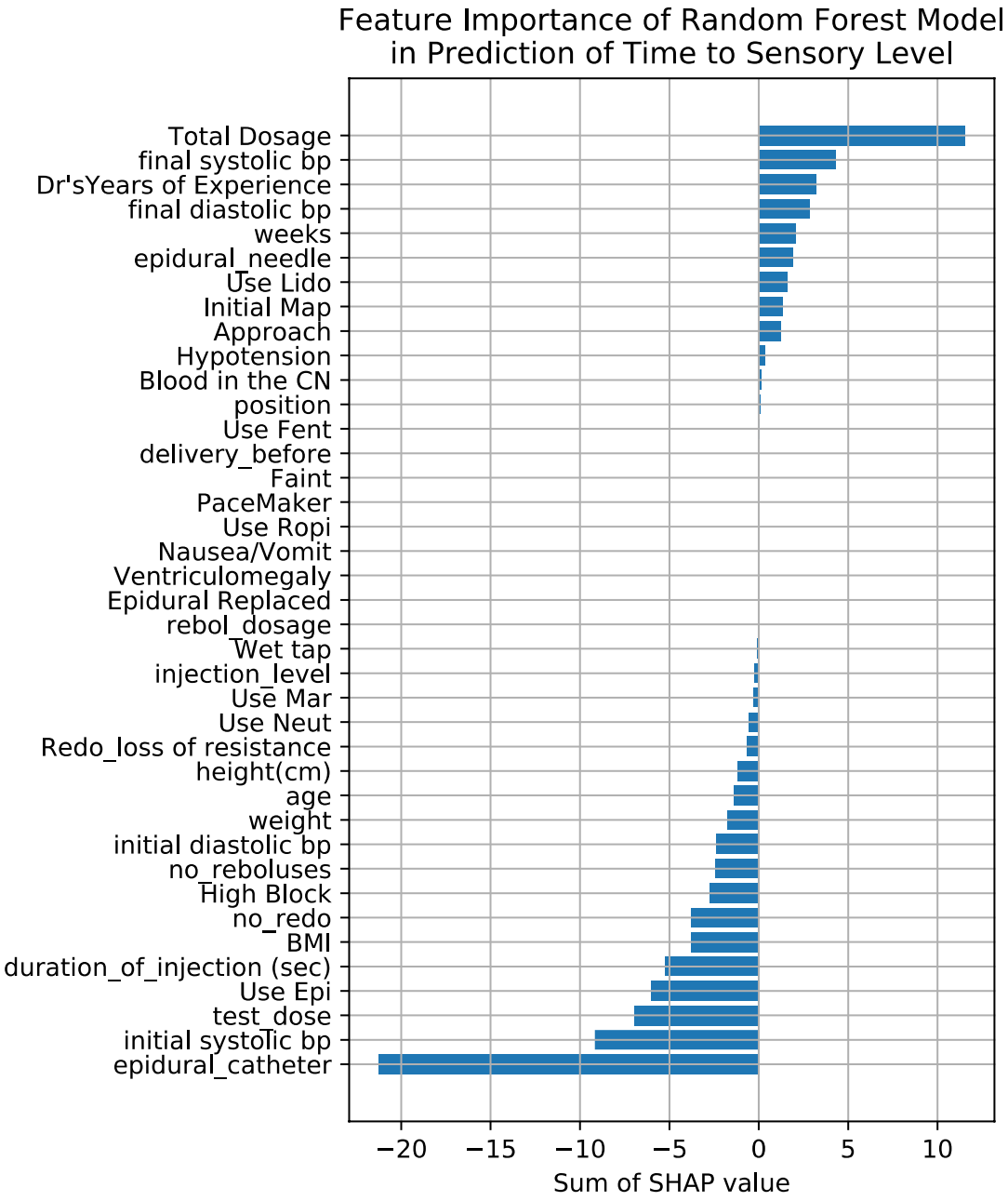

Figure 3.7 – Feature importance (SHAP value) of random forest model in the prediction of time to sensory level.

Table 3.6 – Performance comparison of random forest and neural network in predicting time to sensory level. MSE: mean squared error, MAE: mean average error, MRE: mean relative error

Dataset		Random forest	Neural network
Training	MSE	27.35	38.27
	MAE	4.08	4.61
	MRE	34.26%	35.50%
Test	MSE	36.76	33.90
	MAE	4.65	4.32
	MRE	39.85%	34.78%

3.4.7 System Simulation and Clinical Practice Improvement

We first ran the computer simulation model using parameters from the 750 observed cases. The simulation was run for 19,651 patients to reflect the total number of babies delivered during a calendar year. We focused on highly revealing issues based on our outcome findings: re-do epidural procedure, hypotension and other complications such as blood in catheter/needle, wet tap, high block, and nausea and vomiting. Expected time for completing the entire epidural workflow was 9.26 minutes under current conditions.

Guided by the results from machine learning and the identified discriminatory features, we optimized the needle-base epidural dose administration process. Table 3.7 summarizes briefly the anticipated changes from the current practice on three scenarios. These scenarios focus on physician variations on administering medication, test dosage and total dosage. Each scenario is characterized by physician's individual epidural technique. In our simulation model, each scenario reflects actual physicians' characteristics such as selecting medications, loss of resistance technique and injecting durations.

Table 3.7 – Simulation scenarios performed to investigate potential reduction in complications.

	Scenario 1: Needle dosage of 15-18 ml	Scenario 2: Needle dosage 20-25 ml (Scenario 2)	Scenario 3: Diverse dose range
Test dosage	2 ~ 5 ml	0 ~ 5 ml	0 ~ 5 ml
Epidural needle dose	15 ~ 18 ml	20 ~ 25 ml	5 ~ 20 ml
Total dosage	15 ~ 25 ml	20 ~ 30 ml	10 ~ 30 ml

Scenario 1 reflects a moderate needle dose with a tight total needle dose across all practitioners (15-18 ml). Scenario 2 allows for higher needle dose up to 25 ml. Scenario 3 offers broader dose variance reflecting current practice while limiting needle dose to 20 ml. Table 5 shows that Scenario 1 results in the lowest re-do rate, hypotension rate and total procedure time compared to the other two scenarios; whereas Scenario 3 shows

acceptable results on hypotension. The hospital delivers roughly 19,651 newborns annually, with 75.1% receiving epidural analgesia. Hence the reduction in patient complication cases, reflected in the last two columns in Table 3.8, is substantial. Overall, all three scenarios improve the procedure time. Using high epidural needle dose, Scenario 2 performs worse than the current practice. For the 1,398 chart review cases, the hypotension rate is 21% among patients satisfying Scenario 1 criteria.

Table 3.8 – Contrast of complication rates using 3 scenarios of needle-based approach.

						Complication Reduction in number of patient cases	
Complication	Occurrence rate per year: Current performance		Scenario 1	Scenario 2	Scenario 3	Scenario 1 - Scenario 2	Scenario 1 - Scenario 3
Re-do epidural process	Needle	5.14%	**4.18%**	4.75%	4.92%	84	109
	Catheter	5.15%					
Replace epidural	2.80%		**2.40%**	2.88%	3.02%	71	91
*Hypotension	50.89%		**31.82%**	55.43%	49.47%	3484	2605

Blood in catheter/needle	0.32%	**0.31%**	0.32%	0.33%	1	3
Wet tap	0.17%	**0.16%**	0.18%	0.17%	3	1
High block	0.33%	**0.33%**	0.33%	0.33%	0	0
Nausea/Vomit	0.35%	**0.34%**	0.35%	0.35%	1	1
Faint	0.17%	**0.17%**	0.16%	0.17%	-1	0
Procedure time	9.26 minutes	**5.12 minutes**	5.98 minutes	5.78 minutes		

*Based on definition used by hospital providers (Table 3.11).

3.4.8 Practice Variance among Providers

Forty-four physicians were observed. The years of practice ranges from 6 to 30 years. All physicians report using needle-based approach with over 68% acquiring this skill at this hospital.

We categorized physicians by years of practice: greater than 25 years (long), between 10 to 25 years (medium), and fewer than 10 years (short). Analysis shows that there is no significant difference in prescribed epidural dosage for C-section (long vs medium: $p < 0.8590$, short vs medium: $p < 0.6623$, long vs short: $p < 0.8245$).

43.52% of providers favor the use of air in the loss of resistance technique, followed by 28.9% for local anesthetic, 11.9% for saline, 11.5% for air+local anesthetic and 4.3% for air+saline. When comparing the time to sensory level versus different loss of resistance

techniques, a significant difference is observed while the height, weight, and age of patients are similar across the preference techniques. When the loss of resistance utilizes air with local anesthetics, the average time to sensory level and frequency of re-bolus are lowest among all other techniques (Figure 3.8, left and Table 3.9).

While there is marginal difference in epidural replaced rate, the overall redo rate appears to be lowest among physicians with medium years of experience. This may be explained that they have adequate experience and knowledge and are in prime condition to deliver high quality service. The statistics also show that experienced physicians have the lowest redo rate in loss of resistance (Figure 3.8, right).

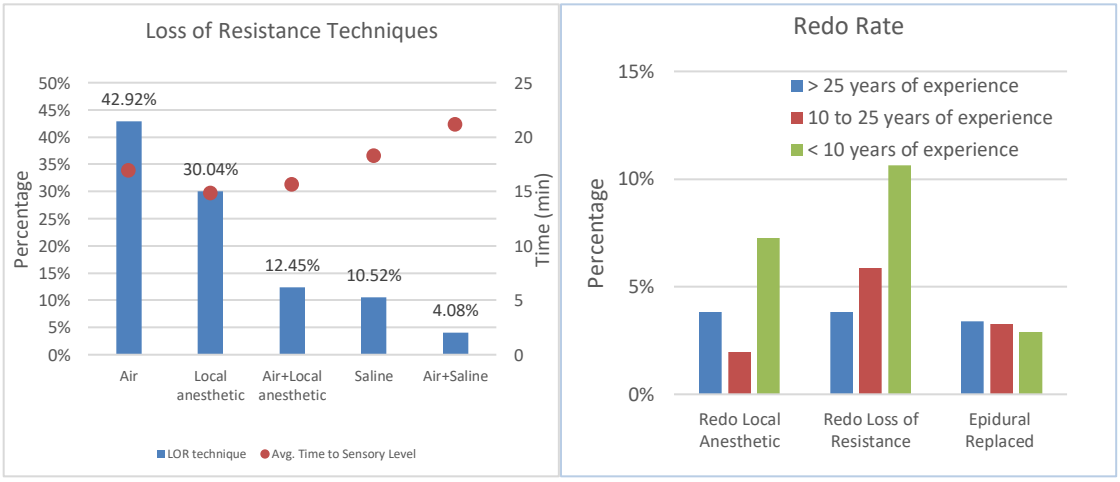

Figure 3.8 – Loss of resistance techniques versus the time to achieve desired sensory level.

Table 3.9 – Frequency of re-bolus with different loss of resistance techniques.

Loss of Resistance Technique	Air	Local anesthetic	Air+Local anesthetic	Saline	Air+Saline

Frequency of Re-bolus	27.66%	32.05%	17.74%	25.00%	37.50%

Patients treated by anesthesiologists with medium and long years of experience also have significant shorter time to sensory level when compared to those administered by less-experienced providers (Table 3.10). Meanwhile, the contrast of difference of hypotension rate, total dosage prescribed, and sensory level show no significant difference with years of experience.

Table 3.10 – Years of experience and time to sensory level.

Years of experience		Avg. time to sensory level (min)		t test statistics	p-values
Short	Medium	17.31	15.59	2.45842927	0.01462619
Short	Long	17.31	15.40	2.49430328	0.01314172
Medium	Long	15.59	15.40	0.34005402	0.73399864

The anesthesiologists apply different standards regarding identifying hypotension (Table 3.11). Among the 44 providers, 34.09% of them use 20% systolic drop from baseline as the criteria, which is also the most common standard. Other common criteria include “Below 90mmHg, systolic” and “Below 90mmHg, systolic or 20% off baseline, systolic”, while 9.09% of the anesthesiologists do not apply a specific quantitative standard. Different standards result in diverse rate of hypotension and even minor changes

of definition can cause major difference in the incidence of hypotension [176]. Our study confirms this conclusion (Figure B.1). *We caution that a universal standard of hypotension should be reached before contrasting treatment and intervention procedures.*

Table 3.11 – Self-reported hypotension definition used by anesthesiologists in the studied hospital.

Self-reported hypotension definition	% of anesthesiologists
20% off baseline, systolic	34.09%
Below 90mmHg, systolic	18.18%
Below 90mmHg, systolic or 20% off baseline, systolic	9.09%
Below 100mmHg, systolic or 20% off baseline, systolic	4.55%
15% off baseline, MAP<55	2.27%
30% off baseline, systolic	2.27%
Below 80mmHg, systolic or 20% off baseline, systolic	2.27%
20% off baseline, MAP<55	2.27%
Non-Quantitative Standard	9.09%
Not Reported	15.91%

3.4.9 Drug Types and Use of Opioids

Anesthesiologists have different drug preferences and overall fifty-one medicine combinations were used. Lidocaine is the most common medicine and is used in 88.79% of all C-section cases. The top five combination drugs are 1) Lidocaine 2%, NaHCO3, Epi, Fentanyl (29.83%), 2) Lidocaine 2%, NaHCO3, Epi (16.05%), 3) Lidocaine 2%, Epi (12.84%), 4) Lidocaine 2% (11.24%), and 5) Lidocaine 2%, Epi, Fentanyl (7.49%); and they are used in over 50% of all patient cases (Figure B.2). 49.70% of all cases involved the opioid fentanyl as one of the components. In 39.46% of the cases, fentanyl was combined with epinephrine.

Lidocaine with epinephrine is more acidic compared to standalone lidocaine, and the acidity causes pain during injection [186]. To neutralize the acidity, NaHCO3 (neut) was applied. Our findings show that neut has little effect on the time to sensory (time to sensory level: 15.51min vs 16.47min, p = 0.0680, $\alpha = \frac{0.05}{4} = 0.0125$). We found that "lidocaine + epi" is similar in achieving sensory level when compared to Marcaine (time to sensory level: 15.61 min vs 17.33 min, p = 0.0649, $\alpha = 0.0125$). In 78.4% of the total cases, epinephrine is added to the medicine as prevention of hypotension. In the cases where Lidocaine is used as the main medicine, epinephrine is beneficial to achieving higher and faster sensory level (sensory level: 4.77 (1.330) vs 5.26 (1.77), p = 0.0120; time sensory to level: 15.61 min vs 17.67 min, p = 0.0303, $\alpha = 0.0125$). More importantly, there is no significant difference in outcome when fentanyl is used (with fentanyl: 15.65 min, without fentanyl: 16.37 min, p = 0.2114, $\alpha = 0.0125$). Our study supports that fentanyl can be avoided in epidural anesthesia.

3.5 Discussion

This study demonstrates the use of broad range of informatics techniques can help to uncover practice characteristics that are critical for care improvement. Of the 3,988,076 documented births in the United States in 2014, 32.2% were delivered via cesarean delivery [187]; and among women delivering vaginally, as high as 61% received epidural or spinal anesthesia [54]. The potential consequences of a failed or misplaced epidural needle are well known to anesthesiologists who practice obstetric anesthesia. While much has been analyzed regarding complications, especially hypotension, there has been limited research regarding the dose-sensory response and standardization of the epidural analgesia procedure to reduce practice variance and maintain low rates of complication. Provision of neuraxial labor analgesia in a timely manner has been shown to be important to many parturients on open-ended patient surveys [188]. Thus, it is important to examine the efficacy and safety of epidural dosing techniques that may shorten analgesic onset.

The rationale for potentially improved analgesia onset with epidural needle injection is uncertain. Dosing prior to placement of the catheter, such as with a combined spinal and epidural approach or through the epidural needle, may have the additional benefit of allowing labor analgesia to commence in instances which catheter placement is in an epidural vein and additional procedure time is necessary. In addition to faster onset of analgesia, it has been reported that dosing through the epidural needle may result in improved quality of epidural anesthesia compared to dosing through the catheter [147]. However, other studies in obstetric [148, 150] and non-obstetric [149] patients receiving epidural anesthesia have observed similar outcome. Recently, G. Ristev et al. 2017 [150] performed the first study in comparing needle and catheter injection of epidural

medications for the initiation of labor analgesia. There remains a serious lack of research examining the potential benefits and risks of initiating labor analgesia with injection of anesthetic medications through the epidural needle. Moreover, little is known regarding practice and patient outcome related to large dose injected through the epidural needle.

We hypothesized that needle injection directly into the epidural space would shorten analgesic onset and improve the quality of subsequent labor analgesia compared to catheter injection. With increasing demand on quality of medical service and evidence of outcome, the medical providers seek to work collaboratively with medical informaticians and systems engineers to comprehensively analyze the performance of the epidural anesthesia service. Leveraging the unique clinical practice at this hospital, we evaluate the safety of a needle-based epidural technique for elective caesarian sections and establish evidence of a safe-level of epidural needle dose. We also analyze and quantify the dose-sensory response evidence and the associated complications in the hands of experienced anesthesiologists. For objective comparison, we contrast our findings to published results. To the best of our knowledge, there is no previous comparative effectiveness study analyzing dosage delivered via needle versus catheter.

Our findings indicate that needle-based approach is faster and more dose-effective in achieving comparable sensory level than the traditional catheter-based approach. Injecting large doses (up to 20 ml) in the epidural space through the epidural needle is safe, with complication rates similar to those reported in published literature. Further, if the needle dose is kept under 18 ml, the resulting hypotension rate will be significantly lower than current catheter delivery practice.

We identified a small subset of discriminatory features, including weeks of pregnancy, patient allergies, number of redos, epidural needle/catheter dose, number of reboluses and dosage that can predict hypotension with 85% confidence using our DAMIP machine learning approach. The identified patient characteristics allow for precautionary care intervention for at-risk patients during the epidural procedure. The provider practice features offer an opportunity for clinical practice guideline development and process improvement. Using system simulation and optimization, we investigated scenarios to reduce the hypotension incidence. Our results suggest that the hypotension rates can be driven down to 31% while the needle dose can be as high as 18 ml. A cohort of 1,398 patients obtained via chart review is used to validate our findings to ensure that they are representative of the hospital clinical practice.

Using machine learning, we quantified the features and their interactive and combination effect to achieving proper sensory level. With accurate prediction of sensory level, our findings can assist anesthesiologists in prognosis with early determination of outcome. Subsequently, the advanced information will allow prompt treatment and patient care. Our analysis reveals that total dosage, duration of injection, weight and physicians' experience are the top features that positively impact sensory level. Higher initial blood pressure, being overweight, and operation redo are indications of unsatisfactory sensory level. Additionally, using the SHAP value, we discovered the non-monotonic effect of factors. This again confirms the sophistication in constructing optimum practice guidance in epidural anesthesia. By breaking down the underlying factors, it is possible to advance the knowledge and practice for better outcome.

We contrasted the proficiency of physician practice and provided insights on their preference in medication and dosage. Understanding the causes and effects of variation can help providers and healthcare organizations avoid practices that negatively impact outcomes. Our results establish evidence of safe and effective epidural needle dosage. They confirm that needle injection directly into the epidural space shortens analgesic onset, reduces medication dosage, and improves the quality of subsequent labor analgesia when compared to catheter injection. This facilitates evidence-based dose delivery to patients that results in safer and more effective pain control during child delivery. The new CPG results in fewer complications and helps with training of anesthesiologists based on evidence-based best practice. *Our study also supports that use of fentanyl has little effect on the outcome and can be avoided in epidural anesthesia.*

Currently there are very few reported studies in which anesthesia providers have initiated labor analgesia by injecting medications through the epidural needle immediately after loss of resistance in order to achieve faster onset of pain relief. This practice site offers a unique opportunity for in-depth study in the efficacy and quality of a needle-based epidural approach due to the practice and the large volume of newborns delivered annually. While design of a direct clinical comparison may be desirable, because the expertise of these physicians is mostly needle-based approach, it seems better suited to compare outcome of this site to reported published results. While this study was performed in a single hospital location, the practice of injecting dose via the epidural needles has been used and reported in obstetric [148, 150] and non-obstetric [149] patients. The results thus are applicable to broad epidural practice in other types of surgeries that required localized anesthesia.

CHAPTER 4 ANTIGENICITY PREDICTION AND VACCINE RECOMMENDATION OF HUMAN INFLUENZA A VIRUS (H3N2) USING CONVOLUTIONAL NEURAL NETWORKS

4.1 Abstract

The rapid evolution of influenza A viruses poses a great challenge to vaccine development. Analytical and machine learning models have been applied to facilitate the process of antigenicity determination. In this study, we designed deep convolutional neural networks (CNNs) to predict Influenza antigenicity. We first systematically analyzed 566 amino acid properties and 141 amino acid substitution matrices for their predictability. We then optimized the structure of the CNNs using particle swarm optimization (PSO). The optimal neural networks outperform other predictive models with a validation accuracy of 0.958. Further, we applied our model for vaccine recommendation over the period from 1997 to 2011 and contrasted the performance of previous vaccine recommendations using traditional experimental approaches. The results show that our model outperforms the WHO recommendation and other existing models and could potentially improve the vaccine recommendation process. Our results show that WHO often selects virus strains with small variation from year to year and learns slowly and recovers once coverage dips very low; whereas our system-approach CNN model selects strains that can differ quite drastically from year to year with consistently good coverage. Overall, we have designed a comprehensive computational pipeline for optimizing a convolutional neural network in the modeling of Influenza A antigenicity and vaccine recommendation. It is more cost and

time-effective when compared to traditional hemagglutination inhibition assay analysis. The framework is flexible and can be adopted to study other type of viruses.

4.2 Significance Statement

Influenza A viruses remain dangerous pathogens with the potential to cause pandemic outbreaks. The World Health Organization (WHO) is constantly monitoring the circulation of influenza viruses in precaution to detect potential pandemic strains. Every year, WHO recommends on which strains should be included in the flu vaccines to protect people from seasonal outbreak. We propose and apply a state-of-the-art deep learning approach to tackle this problem. Our study designs an *in silico* prediction of antigenicity of Influenza A virus using convolutional neural networks. We systematically analyze the selection of the physicochemical properties and optimize the structure of the neural networks. This leads to a validation accuracy of 0.958. Further, using our model, we show that vaccine strain recommendations could be improved significantly.

4.3 Introduction

4.3.1 Current State-Of-The-Art Antigenicity Models

The genome of influenza viruses is constantly changing, and thus continuous vigilance is required to protect the world population not only from seasonal influenza but also from novel influenza A viruses that could trigger a pandemic. Seasonal influenza is an acute viral infection and is estimated to cause 3 to 5 million cases of severe illness and around 250,000 to 500,000 deaths worldwide [12]. Among the three subtypes, type A is the only one known to cause pandemics [12].

Vaccination is the most effective way to prevent Influenza outbreaks and epidemics. To produce a qualified vaccine, a composition virus must be evaluated and should represent the newly emerged circulating viruses which are capable of escaping from the human immune system. However, the rapid evolution of influenza virus poses a severe challenge for fast and accurate vaccine production [13]. Modeling of influenza pathogenicity has focused on hemagglutinin (HA) which executes the function of binding with host cells and triggers the process of virus internalization [189]. Hemagglutinin is also the primary target of antibodies. Two mechanisms have empowered HA the capability of frequent escape from the elimination of human immune system, one is antigenic drift due to lack of proof-reading of RNA polymerase [7], the other is reassortment involving one or more gene segments from different subtypes [10, 11].

The "gold standard" for evaluating the efficacy of vaccine and characterization of virus strains is the hemagglutination inhibition assay (HI assay) [14, 15]. However, the process of conducting HI assay is labor and economic intensive. Hence, a wide range of sequence-based methods have been proposed to infer the antigenicity of Influenza virus [16-21].

Numerous research [20, 190-193] has explored point mutations and their association of influenza epidemic, primarily based on a limited number of amino acid properties. However, these models only measure the contribution of chosen amino acids as individuals. As a consequence, they lack the modeling capacity of the combinatorial effects introduced by the interactions of amino acids in a 3D structure.

In silico antigenic characterization using machine learning approach has been gaining attention. Y.C. Liao [19] improved the model by quantifying the amino acid difference with change of polarity, charge and structure and applied iterative filtering algorithm, multiple regression, logistic regression and SVM algorithms. Y. Yao[18] observed the limitation in the selection of amino acid matrices in previous sequence-based method and systematically analyzed amino acid index dataset 2. And J. Qiu [194] stepped beyond sequence information by incorporating spatial information with a linear model.

Understanding the combinatorial effect of point mutations of influenza A and expanding the number of amino acids in the analysis may better reveal the relationship between HA sequence and its antigenicity. In this study, we designed a computational pipeline based on CNN and fast optimization algorithms for antigenicity prediction. Our model systematically explores all the amino acids and their combinatorial effect. We benchmarked our system-CNN approach with current state-of-the-art methodologies [18, 19, 194].

A reliable prediction of antigenicity can be readily applied to vaccine composition recommendation. Influenza A virus is continuously monitored globally, and twice yearly, WHO work in collaboration with experts from WHO Collaborating Centers and Essential Regulatory Laboratories to make recommendations on influenza vaccine composition for both northern and southern hemispheres for the next epidemic season. A successful selection of vaccine strain is signified by highly induced immune effect against target virus, which requires the chosen vaccine representing the new mutations of prevalent virus in circulation. The selection of vaccine strain is consisted of collection of clinical specimens, diagnosis and virus isolation, antisera production, thorough antigenic and genetic analysis,

serological study of seasonal influenza vaccine and finally the selection of candidate viruses for vaccine use [195]. The antigenic and genetic analysis process is primarily composed of continuous hemagglutination inhibition assay test, in which candidate strains are tested against circulating ones and the "antigenic distance" is measured. However, this empirical methodology is limited by the availability of high-level biosafety laboratories and economic cost and is time-consuming. In this study, we demonstrate our approach in finding optimal strains for vaccination recommendation and establishe a pipeline for a highly accurate and efficient recommending system.

4.3.2 Application of Convolutional Neural Network

Deep convolutional neural network (CNN) has been applied successfully in visual analysis [196-199] and natural language processing [200-202]. Given its outstanding performance in image processing, CNN is heavily applied in medicine especially within the realm of cancer detection [203-205] and neurology [206-208]. D. Quang [209] proposed a hybrid convolutional and recurrent deep neural network to predict the function of non-coding region of DNA. J. Kim [210] applied CNN on climate heat maps to detect influenza outbreak. S. Zhong [211] applied CNN to predict influenza dynamics in a location network for location-oriented intervention strategy. Thus far, CNN has not been applied to antigenicity analysis of influenza.

The structural design of a neural network is critical for its performance. Tuning the hyperparameters and structure of a deep neural network via a manual process requires much expertise and experience and remains a challenge due to the large number of architectural design choices. Numerous approaches have been proposed to optimize the

architecture of neural networks [212-223]. Despite their successes, most of them are restricted to fixed search choices and cannot handle non-continuous space. To address this issue, biological inspired algorithms have been applied including particle swarm optimization [212, 222] and genetic algorithm [221, 223]. Among these approaches, particle swarm optimization is able to optimize the structure, hyperparameters and activation of a neural network simultaneously while maintaining good computation performance [212].

4.3.3 Study Objective

In this study, we designed a systems biology machine learning framework to analyze all prior years' viruses to predict and select a set of strains for vaccine development. We first evaluated the combinatorial effect of point mutations of influenza A virus using a convolution neural network approach for antigenicity quantifying (Figure 4.1). The CNN model was designed to scan a large sub-region of the influenza sequence, which enables the model to potentially quantify the spatial relationship and interaction of amino acids that are not necessarily adjacent in a sequence. The CNN model extracted and formulated high level patterns from the sequence through intermedia layers, thus advanced the understanding of pathogenicity of the virus. Using particle swarm optimization, we optimized the CNN model and its feature space. The fast heuristic offers an efficient computational environment while achieving good performance.

Specifically, leveraging CNN's effectiveness on recognizing patterns in images, we innovatively constructed the patterns of HA protein sequence using amino acid indices. Training on these patterns, the CNN model analyzed the principle introduced by individual

mutations and their associated combinational effect. Furthermore, we systematically analyzed all available amino acid properties for the predictability of H3N2 antigenicity.

We next applied the predicted antigenicity results to vaccine composition recommendation. We first reported the efficacy of the World Health Organization (WHO) vaccine recommendation. Next, we analyzed the ideal scenario: an optimal vaccine recommendation when the circulating strains are known. This is followed by exploring optimal vaccine recommendations using our CNN model.

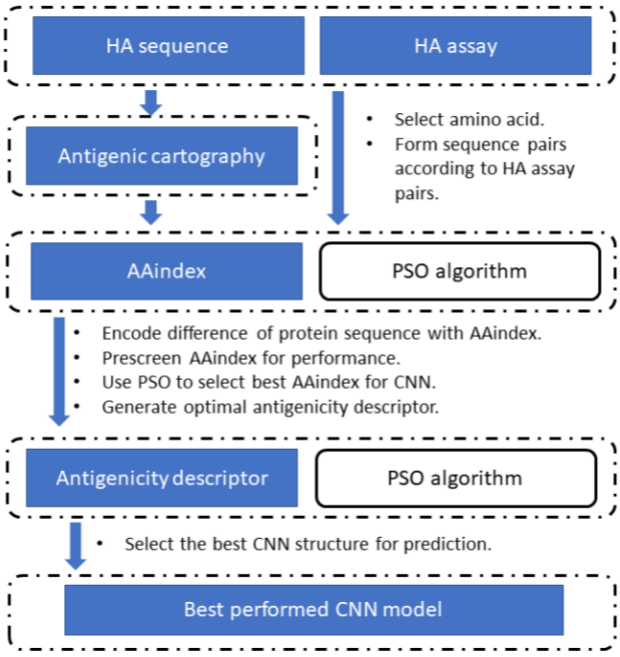

Figure 4.1 – The computational pipeline for antigenicity prediction. HA sequence and HI assay data were used to construct HI sequence pairs. HI assay was also used to make antigenic cartography to generate more HA pairs (augmented set via multi-dimensional scaling). The HA sequence pairs were filled with data using the metrics in AAindex, the choice of which was optimized using PSO algorithm. Upon obtaining the optimal antigenicity descriptor, the optimal CNN model is constructed using PSO algorithm.

4.4 Materials and Methods

4.4.1 Dataset

HI assay data was collected and combined from T. Bedford [224] and WHO reports. The T. Bedford dataset includes HI titer for seasonal A/H3N2 influenza viruses and ferret antisera isolated between 1968 and 2011, which has a total of 10,059 recordings of antigen-antiserum pairs. The dataset from WHO was obtained via batch search, weekly epidemiological records, and influenza summary, ranging from 1980 to 2017. After filtering for A/H3N2, we obtained a total of 755 HI titer pairs from these WHO records. Duplicates in the datasets were averaged into one entry and titer numbers indicated as "<20" and "<40" were taken as half of the value. The final set contains 6,166 unique HI titer pairs. Among the HI titer data, 5,916 pairs involving virus strains from 1968 to 2010 were used as the training set, while the remaining 250 pairs from 2011 to 2016 were used as an independent validation set.

In addition, we constructed the antigenic cartography using multidimensional scaling proposed by D.J. Smith [225] and acquired 156,255 HI pairs calculated with the coordinates of strains. This augmented set was then partitioned into 145,930 training samples and 10,325 validation samples using the same partition time range as described above. In total, we obtained 463 strains and the HA1 protein sequences of which were downloaded from NCBI Influenza Virus Database [226], Influenza Research Database [227] and GISAID [228]. The sequences were aligned using MUSCLE [229] under default parameters.

4.4.2 Antigenic Distance

The HI titer value H_{ij} is the maximum dilution of serum containing antibody raised against virus j, which is necessary to inhibit erythrocytes agglutination induced by virus i. We followed D.J. Smith's [225] definition of antigenic distance :

$$D_{ij} = b_j - log_2(H_{ij}) \tag{4.1}$$

$$b_j = log_2\, max(HI\ of\ antiserum\ j) \tag{4.2}$$

If D_{ij} is greater than 4, virus i and j are considered antigenic variant (positive), otherwise they are antigenic similar (negative). An antigenic variant pair represents that the underlining virus can "escape" from the immune system that was vaccinated by the other virus.

4.4.3 Modelling Antigenic Variance

Conservation scores were calculated using ConSurf [230] for the selection of amino acids. Amino acid positions in the alignment with no gaps and a conservation score smaller than 0.99 were collected as the basis for making quantitative descriptors of antigenic variance. A logistic regression model equation (4.3) was constructed to further filter the candidate amino acids.

$$y = \frac{1}{1 + e^{-(\beta_0 + \beta_1 x)}} \tag{4.3}$$

For each amino acid position, a binary vector x was constructed across all HI pairs which represent the difference between virus and serum. After convergence, the mutual

information, MI equation (4.4) of predicted and true response was calculated and a threshold of 1e-4 was used to filter amino acids candidates.

$$I(X,Y) = \sum_{x \in X} \sum_{y \in Y} p(x,y)\, log\left(\frac{p(x,y)}{p(x)p(y)}\right) \tag{4.4}$$

Unlike previous studies [18, 190, 194] which limit the selection of candidate amino acid to surface accessible ones, this study included inner amino acids considering their potentially important roles.

For all the amino acid positions, we constructed a vector corresponding to the HI titer pairs with the value in the vector deduced from selected amino acid index [231], representing aligned HA sequences. The value was obtained by subtracting the value of amino acid in serum virus from that of antigen virus. There are three datasets of AAindex database: amino acid indices (AAindex 1), amino acid mutation matrices (AAindex 2) and amino acid pair-wise contact potentials (AAindex 3). We applied the logistic regression model to test the predictability of three amino acid indices one at a time. A moving window technique was used to produce 10 training and testing sets based on the year of virus, thus guaranteeing that older pairs were used to predict newer pairs. The performance was averaged among the 10 sets. After comparing both MCC and MI of the training and the testing sets, only AAindex 2 and 3 were merited for further analysis. After filtering out non-applicable values, we obtained 92 matrices of AAindex 2 and 43 matrices of AAindex 3. Particle swarm optimization algorithm was then used to further select candidates from these AAindex 2 and 3 matrices.

4.4.4 Convolutional Neural Networks (CNN)

CNN models were implemented with Keras v2.0.8 [232]. The composition of CNN in this study includes convolution layers, pooling layers, dropout layers, and fully connected layers. A convolution layer is defined by the number of filters, filter size, stride size, and activation function. A pooling layer is defined by the kernel size and stride size. A dropout layer is defined by the probability of dropout. And a fully connected layer is defined by the number of neurons and activation function. The CNN structure is illustrated in Figure 4.2. All previous mentioned hyperparameters with the number of CNN modules and number of dense layers are formed as a vector with proper normalization and optimized using particle swarm optimization algorithm. The range of the hyperparameters of the CNN model are summarized in Table 4.1.

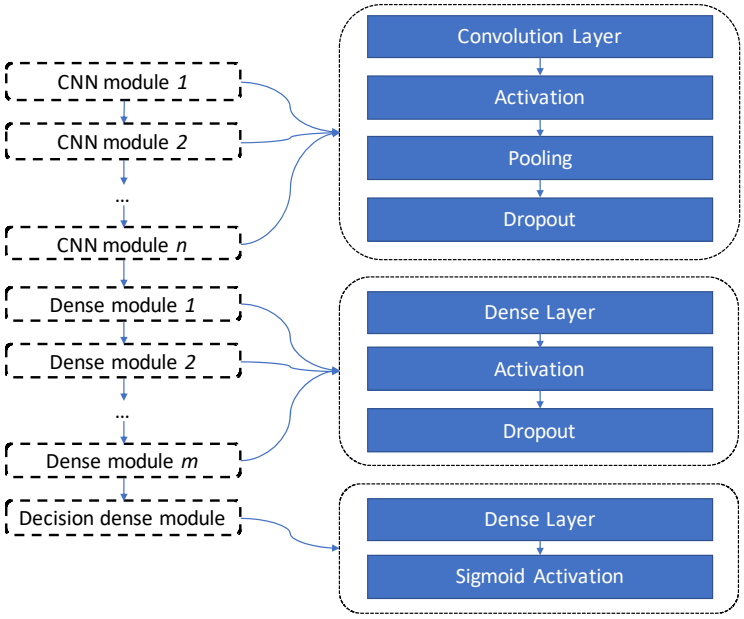

Figure 4.2 – Design schema of the CNN networks.

Table 4.1 – Range of hyper-parameters used in our CNN.

Hyperparameter	Min	Max
Number of CNN modules	1	4
Number of filters	32	256
Filter size	2	5
Filter stride	1	3
Pooling size	1	4
Pooling stride	1	4
Dropout probability	0.1	0.5
Number of dense modules	1	3
Number of neurons in dense layers	72	256
Dropout probability	0.1	0.5

4.4.5 Particle Swarm Optimization (PSO)

We have implemented effective PSO algorithms for feature selection [233, 234]. In this work, PSO was designed to optimize the choice of amino acid index, and the structure

and the hyperparameters of our CNN model. Our PSO algorithm was implemented in Python 3.6 and worked as follows:

Step 1. Initialize the optimization process with a set of 25 particles with random locations and velocities.

Step 2. Define the von Neumann neighborhood [235] for the initialized particles.

Step 3. For all the particles, evaluate the fitness function. If the fitness value is better than the particle's best value, update the personal best position p^{p}_{best}, and the personal best value v^{p}_{best} accordingly.

Step 4. Compute the local best value v^{l}_{best}, local best position p^{l}_{best} to update all particles. Change the velocity and position of particles according to the following formula [236]:

$$v_{t+1} = w * v_t + r_1 * c_1 * \left(p^p_{best} - p^p_t\right) + r_2 * c_2 * \left(p^l_{best} - p^p_t\right) \tag{4.5}$$

$$p^p_{t+1} = p^p_t + \Delta t * v_{t+1} \tag{4.6}$$

Step 5. Go to *Step 3* until the maximum number of iterations is met or the change of global best value is less than a pre-set threshold.

We optimized using PSO to select 10 indices from the AAindex. A binary vector was used to represent the selection of the AAindex and served as the position vector of the particles. The PSO algorithm was initialized with 25 particles, and a random speed uniformly initiated between -1 and 1. The algorithm terminates when the maximum number

of iterations reaches 50, or when the change in the global best value is smaller than $1e^{-6}$. In the process of updating the particle's position vector, the top ten ranked elements were set to 1 and the rest to 0, which maintains the conceptual rule of the position vector. The fitness value was returned by a simple CNN model (Table 4.2), which uses the position vector as the choice of AAindex and trained with 10 epochs and batch size of 600. Upon termination, the optimal position vector was reported and the corresponding AAindex were retrieved. The selected 10 AAindex were then used to calculate the value difference between virus strain and serum strain. The resulting values would form the feature matrix for each HI pair. In the final step, a tensor (size: sample size × amino acid candidates×selected AAindices) was generated and split accordingly for further training and validation.

Table 4.2 – CNN structure used for optimizing AAindex selection.

Layer Index	Layer
1	Convolution; Filter: 32, Filter size: 3, stride: 1, activation: ReLU.
2	Max pooling; Kernel size: 2, stride: 2.
3	Dropout; Dropout rate: 0.3.
4	Dense; Neurons: 128, activation: ReLU.
5	Dropout; Dropout rate: 0.5.

6	Dense; Neurons: 64, activation: ReLU.
7	Dropout; Dropout rate: 0.5.
8	Dense; Neurons: 1, activation: sigmoid.

In the optimization of the CNN structure, a vector of length 26 with continuous values ranging between 0 and 1 was used to represent the structure of the underling CNN. In the optimization process, the constant inertia w is set to 0.5, cognitive constant c_1 and social constant c_2 are both set to 2.

4.4.6 Performance Metrics

The performance of the models was evaluated using accuracy, sensitivity, specificity, Matthews correlation coefficient (MCC) and f-scores on their predictability of antigenic variance. Specifically,

$$\text{Accuracy} = \frac{TP+TN}{TP+TN+FP+FN} \tag{4.7}$$

$$\text{Sensitivity} = \frac{TP}{TP+FN} \tag{4.8}$$

$$\text{Specificity} = \frac{TN}{TN+FP} \tag{4.9}$$

$$\text{MCC} = \frac{TP \times TN - FP \times FN}{\sqrt{(TP+FP)(TP+FN)(TN+FP)(TN+FN)}} \quad (4.10)$$

$$F - score = 2 \cdot \frac{precision \cdot recall}{precision + recall} \quad (4.11)$$

where TP represents true positive, TN represents true negative, FP represents false positive, FN represents false negative, recall equals sensitivity and precision equals TP divided by the sum of TP and FP.

4.4.7 Optimization of Vaccine Recommendation

The recommendation of H3N2 vaccine composition was collected from the data repository of WHO, among which we chose six strains for analysis (Table 4.3).

Table 4.3 – WHO's recommendation of H3N2 vaccine composition.

Strain	Start year	End year
A/Sydney/5/1997	1998	2000
A/Moscow/10/1999	2000	2004
A/Fujian/411/2002	2004	2005
A/California/7/2004	2005	2006
A/Wisconsin/67/2005	2006	2008

A/Brisbane/10/2007	2008	2010

The efficacy of vaccine composition can be measured by antigenicity coverage which is defined as

$$C_{a,i} = \frac{K_{a,i}}{M_i} \quad \textbf{(4.12)}$$

Here $C_{a,i}$ denotes the antigenicity coverage of strain a in year i, $K_{a,i}$ represents the number of strains similar to strain a in year i, and M_i means the total number of newly emerged vaccine strains in year i.

We proposed the following optimization to obtain the optimal recommendation of vaccine composition:

$$\max \sum_{i=1}^{n-1} [w(s_i|y_i) + w(s_{i+1}|y_{i+1})] \quad (4.13)$$

$$\text{s.t. } g(s_i) < y_i, i = 1, \dots, n \quad (4.14)$$

where $g(s_i)$ represents the year of virus strain s_i, and $w(s_i|y_i)$ is the antigenicity coverage of virus strain s_i in the year of y_i. Constraint (4.14) restricts the selection of candidate vaccine to emerge earlier than the year of recommendation.

Specifically, let **S** denote the collection of all virus strains**,** and $s = [s_1, s_2, \dots, s_n]$ is a permutation of a subset of **S** with size *n.* $\boldsymbol{s}^* = argmax_s \sum_{i=1}^{n-1}[w(s_i|y_i) + w(s_{i+1}|y_{i+1})]$ represents the optimal solution.

4.5 Result

4.5.1 Selection of Candidate Amino Acid

We extend the traditional way of selecting antigenicity-dominant positions from surface ones to all non-conserved amino acids. This was based on two assumptions: 1) Surface amino acids may directly interact with antibodies, and inner amino acids are equally important in the role of affecting the overall 3D structure of the protein; 2) The change of antigenicity introduced by point mutations is more complicated than a linear addition of individual contribution, thus requiring a comprehensive modeling of spatial and long distant interaction.

We collected amino acid positions in the alignment of the 463 HA1 protein sequences with no gaps and a conservation score smaller than 0.99 as the basis for making quantitative descriptors of antigenic variance. This results in a total of 116 most mutated amino acid positions (Figure 4.3). The number was further reduced to 96 using a mutual information threshold.

The relationship between spatial and sequential distance of the 96 candidate amino acid positions was explored in Figure 4.4. We observe that due to the complexity of HA1, the distances are not linearly related. This phenomenon indicates that amino acids on the HA structure can interact even with large sequence distances between them. To facilitate

our model to learn this phenomenon, the size of the first kernel of our CNN networks was fixed at 96, equal to the total number of amino acids selected for prediction.

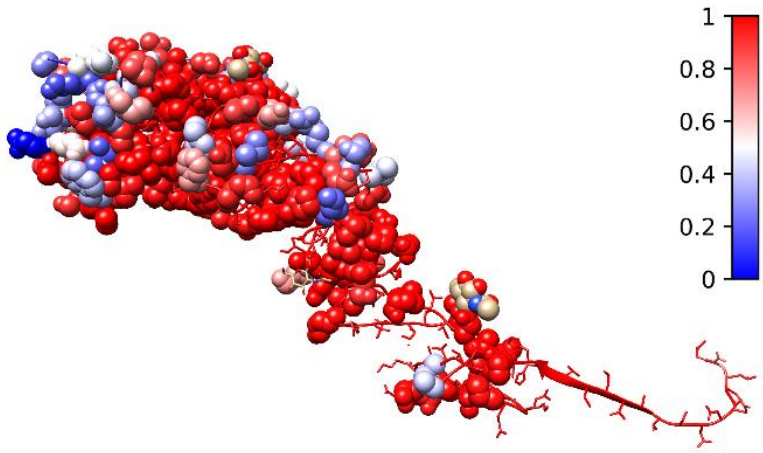

Figure 4.3 – Conservation score calculated using the alignment of all protein sequences and shown on the 3D structure of 3HMG. The 96 selected amino acids are shown as sphere and the rest are shown as ribbon. Red represents the most conserved, and blue represents the most non-conserved.

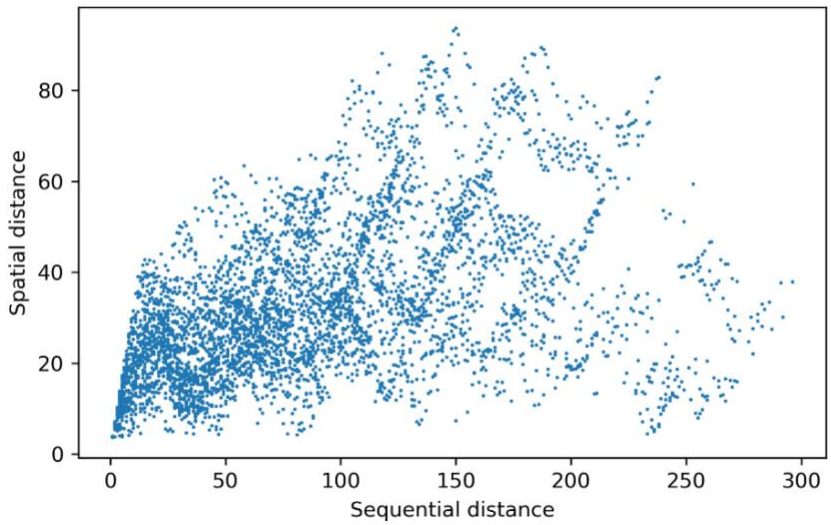

Figure 4.4 – Spatial and sequential distances of candidate amino acids. Each amino acid pair is represented by a dot in the figure. There are 4,560 pairs for the 96 amino acids.

4.5.2 Systematic Analysis of Predictability of AAindex

AAindex [231] is a database of numerical values representing physicochemical and biochemical properties of single and paired amino acids, which are primarily consisted of three sections: amino acid physicochemical properties (AAindex1), substitution matrices (AAindex2) and statistical protein contact potentials (AAindex3). The choice of AAindex is crucial to the predictability of machine learning models.

After filtering out missing data in AAindex, we obtained 553, 92, 43 recordings of AAindex 1, 2 and 3 respectively. Each of the recording was used to construct the feature vector based on the resulting 96 amino acid positions. The predictability measured by Matthews correlation coefficient (MCC) and mutual information (MI) were obtained using a simple logistical model. The sorted MCC and MI slopes of AAindex 2 and 3 indicate sufficient potential in predictability whereas AAindex 1 does not (Figure 4.5, Figure 4.6).

The best MCC of training sample using AAindex 2 and 3 reach as high as 0.465 and 0.409 respectively while AAindex 1 only achieves 0. This result reflects the fact that AAindex 2 and 3 measure the properties involved in amino acid interaction and interchanging instead of merely the physical and chemical features as in AAindex 1.

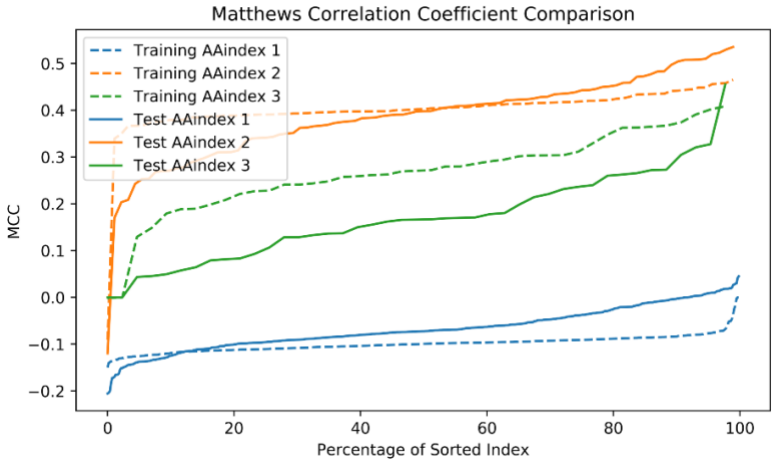

Figure 4.5 – Comparing Matthews correlation coefficients produced using each of the AAindex as predicting variable via a logistic regression model.

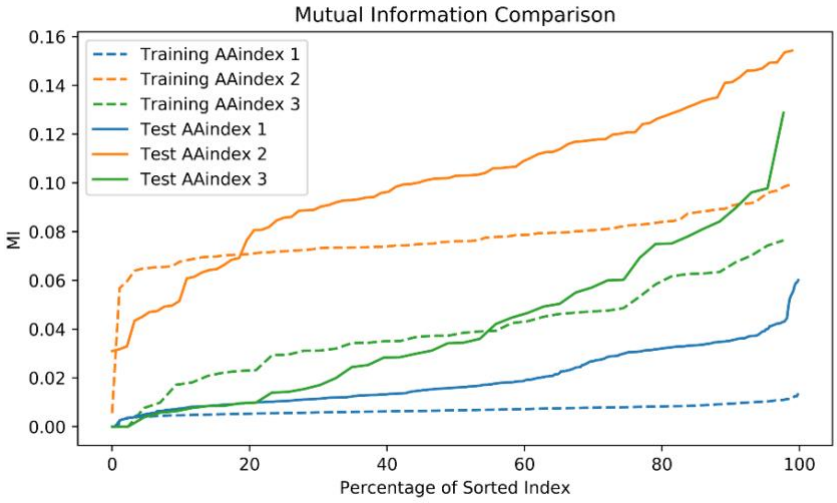

Figure 4.6 – Comparing mutual information produced using each of the AAindex as predicting variable via a logistic regression model.

4.5.2.1 Optimized Selection of AAindex

We benchmarked several optimization algorithms including the Newton's method, Nelder-Mead [237], Powell's algorithm [238], the Conjugate Gradient method [239], the Broyden–Fletcher–Goldfarb–Shanno algorithm (BFGS) [240], the limited-memory BFGS-B (L-BFGS-B) [241], the truncated Newton (TNC) algorithm [242], constrained optimization by linear approximation (COBYLA) [243], and sequential least squares programming (SLSQP) [244]. In a scenario where there are multiple local maxima (Figure 4.7), PSO algorithm is usually able to find the global maximum when the rest of the algorithm failed to do so (Figure 4.8). All the candidate algorithms were trapped in a local maximum close to the initial point, while the Nelder-Mead algorithm failed to converge.

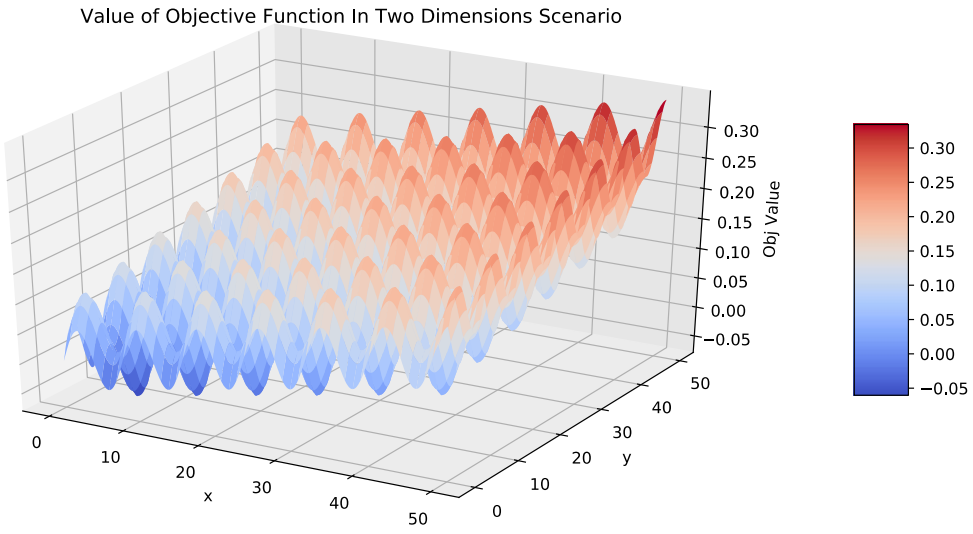

Figure 4.7 – A scenario with numerous local maxima.

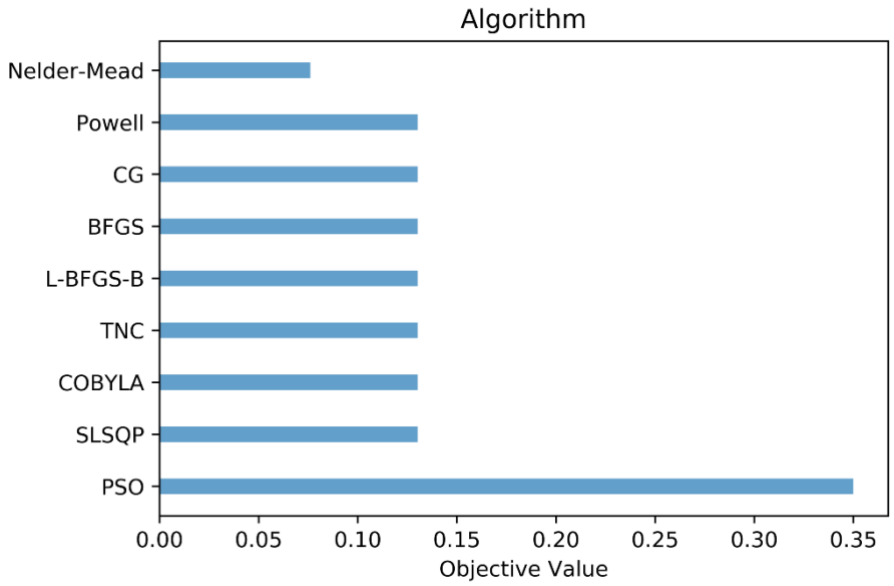

Figure 4.8 – Comparison of optimization algorithms on 25 instances

The PSO algorithm returns 10 matrices from AAindex 2 and 3 (Table 4.4). Our result is inspiring and different from previous attempts in a way that the optimized combination of AAindex do not include any PAM250 or BLOSUM62, which is commonly thought to have good predictability [19, 245, 246]. We note that these two matrices were also absent in one previous research [191]. After ranking the MCC of AAindex candidates using a simple logistical regression model, conclusion can be drawn that our candidates are not merely a collection of best performed single variates, rather they produce best result with certain combinations, which is difficult to obtain using a step-wise optimization algorithm.

Table 4.4 – Optimized AAindex for further feature construction.

AAindex ID	AAindex Source	Description	Rank
BENS940104	2	Genetic code matrix (Benner et al., 1994)	18
LUTR910108	2	Structure-based comparison table for alpha helix class (Luthy et al., 1991)	53
MUET010101	2	Non-symmetric substitution matrix (SLIM) for detection of homologous transmembrane proteins (Mueller et al., 2001)	63
KOLA920101	2	Conformational similarity weight matrix (Kolaskar-Kulkarni-Kale, 1992)	75
AZAE970101	2	The single residue substitution matrix from interchanges of spatially neighbouring residues (Azarya-Sprinzak et al., 1997)	86

BONM030104	3	Distances between centers of interacting side chains in the antiparallel orientation	1
TANS760101	3	Statistical contact potential derived from 25 x-ray protein structures	5
ZHAC000106	3	Environment-dependent residue contact energies (rows = coil, cols = coil)	7
BETM990101	3	Modified version of the Miyazawa-Jernigan transfer energy	22
BONM030103	3	Quasichemical statistical potential for the parallel orientation of interacting side groups	29

4.5.2.2 Optimized Deep Neural Network Structure

An optimized structure of convolutional neural network is reported back with three layers of convolutional layers and one fully connected layer (Table 4.5). The convolutional layers treat the input tensor as an image of size 96*10 with only one channel, and scan through the "image" with specific kernel size and stride steps, which extract and form the upper level features from the previous layer.

Table 4.5 – Optimized structure of convolutional neural network.

	Filter/Neurons	Kernel size	Stride	Pooling	Dropout
Conv 1	193	96*10	3	1	0.1
Conv 2	212	5*10	2	1	0.165
Conv 3	109	5*10	3	1	0.1
Dense 1	256	N/A	N/A	N/A	0.241

4.5.2.3 Performance of the CNN Model

We tested our CNN model extensively and validated using two sets of data: the original data set and an augmented set obtained via multi-dimensional scaling. The first data set contains 5,916 HI pairs for training and 250 for validation. This results in a very balanced positive case ratio of 0.432 and 0.412. The augmented set contains 145,930 for training and 10,325 for validation. This larger dataset results in positive case ratio of 0.780 and 0.923 respectively. This significant increase in positive case ratio reveals that a large number of similarity relationship in H3N2 viruses were previously unknown due to the limited and costly experiment of hemagglutination inhibition assays. This again asserts the necessity of *in silico* modeling of Influenza pathogenicity. Our models report an overall accuracy of 0.921 and 0.924 on the training data, and 0.832 and 0.958 on the validation data (Table 4.6, Table 4.7).

We implemented the state-of-the-art approaches from the literature: Y.C. Liao's [19], J. Qiu's [194] and Y. Yao's [18] and contrasted theirs against our approach (Table 4.6, Table 4.7, Table C.1). Y.C. Liao applied three linear models with scoring method being polarity, aromaticity, PAM25 and BLOSUM52. J. Qiu stepped beyond sequence information by incorporating spatial information with a linear model. Y. Yao's joint random forest method innovatively transformed more than one AAindex metrics into a feature matrix and achieved an excellent result with validation accuracy 0.938 and MCC 0.632. Our optimized CNN with multi-dimensional scaling (MDS) performed the best with validation accuracy as high as 0.958 and MCC 0.732. Both Y. Yao's and our approaches are more stable in maintaining similar level of accuracy, sensitivity and specificity.

Table 4.6 – Accuracy of models in training set.

Model	Accuracy	Sensitivity	Specificity	MCC	F-score
Liao's	0.701	0.748	0.599	0.335	0.775
Qiu's	0.718	0.782	0.577	0.354	0.792
Yao's	0.881	0.927	0.722	0.653	0.924
CNN	0.921	0.877	0.954	0.839	0.906
CNN+ MDS	0.924	0.958	0.807	0.777	0.952

Table 4.7 – Accuracy of models in validation set.

Model	Accuracy	Sensitivity	Specificity	MCC	F-score
Liao's	0.762	0.773	0.724	0.442	0.833
Qiu's	0.742	0.680	0.948	0.531	0.802
Yao's	0.938	0.953	0.765	0.632	0.966
CNN	0.832	0.839	0.821	0.651	0.861
CNN+MDS	0.958	0.970	0.817	0.732	0.977

4.5.3 Antigenicity Analysis and Optimal Vaccine Recommendation

Simulating the vaccine recommendation process, we contrasted our CNN model to Y.C. Liao's [19], J. Qiu's [194] and Y. Yao's [18] models in predicting antigenicity for a sequential year range (Table 4.8, Table C.2). Our model outperformed these previous models on 11 out of the 14 cases with a higher validation MCC. Our model is especially robust in giving a high specificity which is useful in determining the closest strains in antigenicity.

Table 4.8 – Comparing Y.C. Liao's, J. Qiu's and Y. Yao's model on sequential prediction.

	CNN model on test set	Compare MCC

Year of test set	Accuracy	Sensitivity	Specificity	CNN	Liao's	Qiu's	Yao's
1998	0.920	0.933	0.852	0.732	0.556	0.811	0.727
1999	0.913	0.940	0.781	0.697	0.536	0.261	0.697
2000	0.892	0.969	0.506	0.565	0.000	-0.218	0.517
2001	0.904	0.948	0.728	0.693	0.533	0.548	0.686
2002	0.766	0.830	0.650	0.486	0.402	0.452	0.393
2003	0.776	0.722	0.876	0.571	0.455	0.353	0.567
2004	0.855	0.888	0.790	0.676	0.189	0.220	0.664
2005	0.843	0.827	0.880	0.667	0.233	0.251	0.698
2006	0.886	0.921	0.812	0.737	0.262	0.200	0.705
2007	0.866	0.905	0.710	0.596	0.034	0.338	0.593
2008	0.844	0.828	0.877	0.672	0.385	0.364	0.595
2009	0.819	0.888	0.594	0.490	0.146	0.624	0.548
2010	0.906	0.927	0.758	0.619	0.362	0.486	0.570
2011	0.918	0.922	0.878	0.660	0.346	0.411	0.649

The antigenicity coverage was calculated for all the recommended strains by WHO from 1997 to 2010 using our augmented dataset. Figure 4.9 shows the antigenicity coverage of WHO recommended vaccine strains. In general, the antigenicity coverage of vaccine displays two major phases: the ascending and the descending stages. Among the six strains, 'A/Sydney/5/1997' and 'A/California/7/2004' represent two successful vaccine recommendation cases, which actually increase in coverage after being chosen in 1998 and 2005 respectively and achieve high coverage percentage. However, a four-year long recommendation of 'A/Moscow/10/1999' dropped in coverage tremendously after 2001, indicating a potential vaccine failure. Similarly, the antigenicity coverage of H3N2 vaccine drops to around 20% during the time of the 2009 H1N1 pandemic.

Figure 4.10 shows the "ideal" optimal vaccine recommendation based on the principle of maximizing the antigenicity coverage year by year. The optimal recommendation is obtained by solving the optimization problem retrospectively (This is the ideal case where it is assumed that knowledge of the circulating strains is known). The optimized result suggests a different virus strain for each year and presents a much better antigenicity coverage when compared to the WHO recommendation (Figure 4.9). Specifically, the coverage of year from 1997 to 2000 reach up to 100% and above 90% from 2001 to 2008. In the optimized result, the model avoids recommending virus strain such as 'A/Moscow/10/1999' or 'A/Brisbane/10/2007', whose coverage drop dramatically in 2002 and 2009 respectively. Instead, the optimized recommendation suggests 'A/Netherlands/301/1999', 'A/Fujian/140/2000', 'A/Netherlands/816/1991', 'A/Kumamoto/102/2002', 'A/Philippines/825/2003', as replacement for 'A/Moscow/10/1999' and 'A/Singapore/57/2006', 'A/Santiago/6881/2007' for

'A/Brisbane/10/2007'. However, an obvious decline in coverage from 2009 to 2010 suggests tremendous variety in the virus genotype. Therefore, both WHO's suggestion and optimal recommendation exhibit coverage decrease. The average and median coverage of the optimized result are 92.80% and 95.89% with a standard deviation of 0.088, while the WHO's recommendation has an average and median coverage of 59.43% and 74.07% with a standard deviation of 0.335.

Figure 4.11 shows the recommendation of vaccine composition produced by our CNN model using MDS. It results in an average coverage of 90.19% and standard deviation of 0.123. The CNN model produced the same vaccine recommendation as the optimal scenario for the period 1997 to 2000. The overall recommendation is different from the optimal scenario, and achieves slightly lower mean coverage, which is expected due to intrinsic predictive errors. Three strains (A/Texas/6/2004, A/Taiwan/83/2006, A/Hong Kong/34430/2009) reported by our CNN models present an upward trend in antigenicity coverage, indicating an increased vaccine efficacy during its installment. For 2009 to 2010, the CNN model suggests A/Switzerland/1397477/2008, which covers around 40% to 80% and achieves better performance than the WHO's A/Brisbane/10/2007 recommendation. Contrasting Figure 4.9 and Figure 4.11, we note that WHO often selects virus strains with small variation from year to year, and learns slowly and recovers once coverage dips very low; whereas our system-approach CNN model selects strains that can differ quite drastically from year to year. This rapid learning appears to offer consistently good coverage.

The average coverage of our CNN model outperforms all three other models (Figure 4.11, Figure 4.12, Figure 4.13, Figure 4.14). Table 4.9 summarizes and compares the coverage of vaccine recommendation from each model.

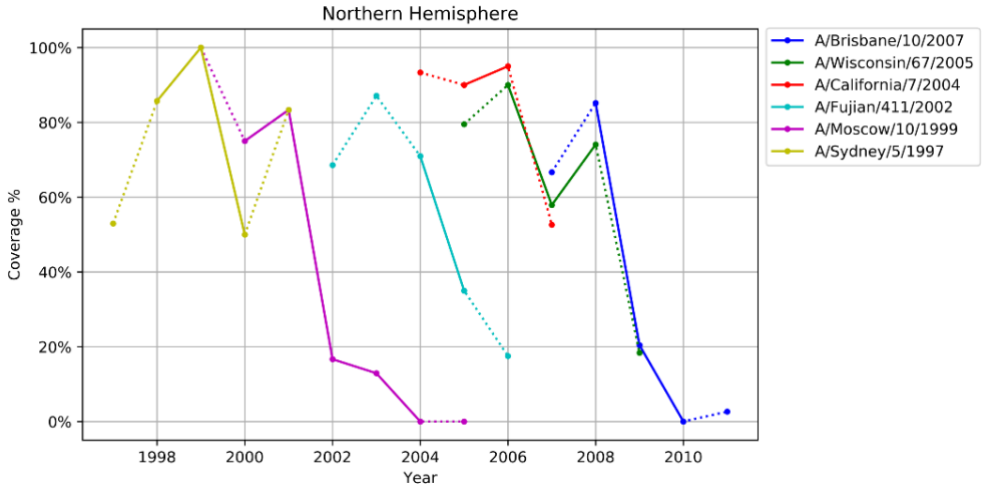

Figure 4.9 – Antigenicity coverage of WHO's recommendation for H3N2 vaccine composition in northern hemisphere. In Figures 4.8 - 4.13, x-axis represents years from 1994 to 2011 and y-axis represent vaccine coverage of each year. Solid lines represent the period of being a recommended strain and dashed lines represent otherwise.

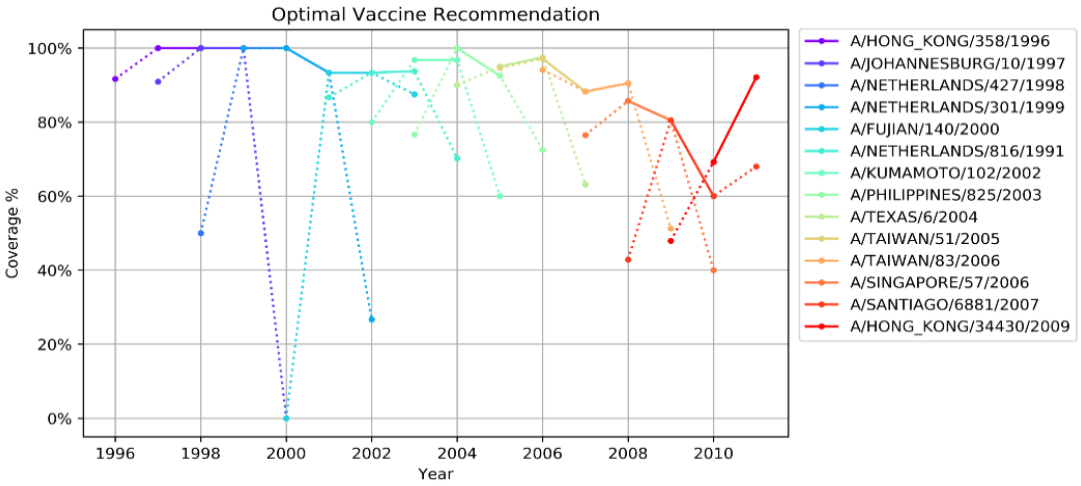

Figure 4.10 – Antigenicity coverage of optimal H3N2 vaccine composition recommendation.

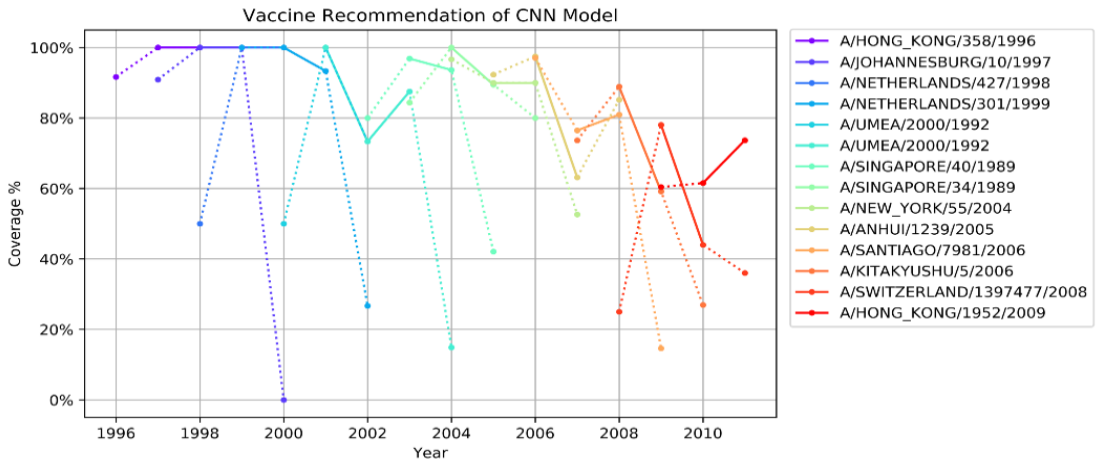

Figure 4.11 – Antigenicity coverage of vaccine recommendation by our CNN model.

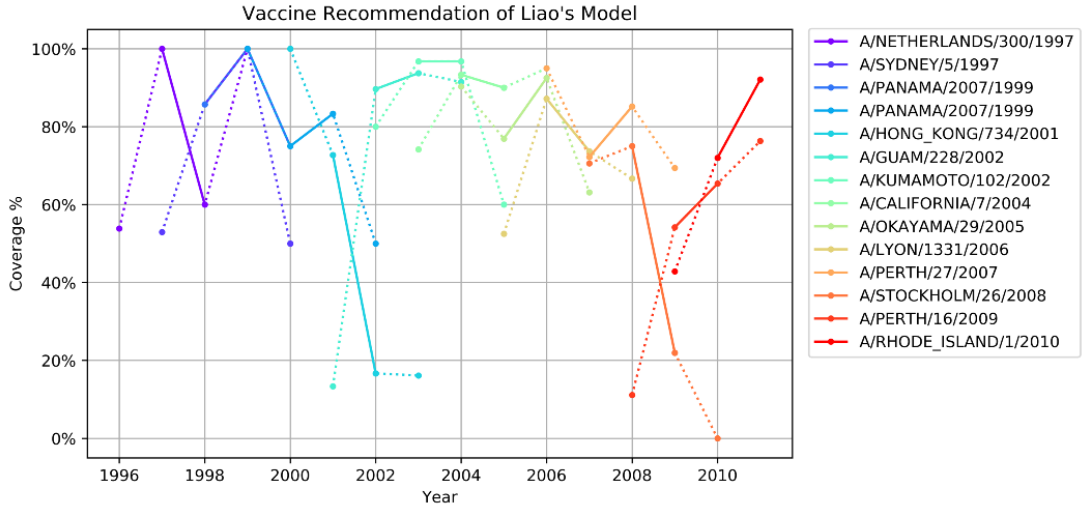

Figure 4.12 – Antigenicity coverage of vaccine recommendation by YC Liao's model.

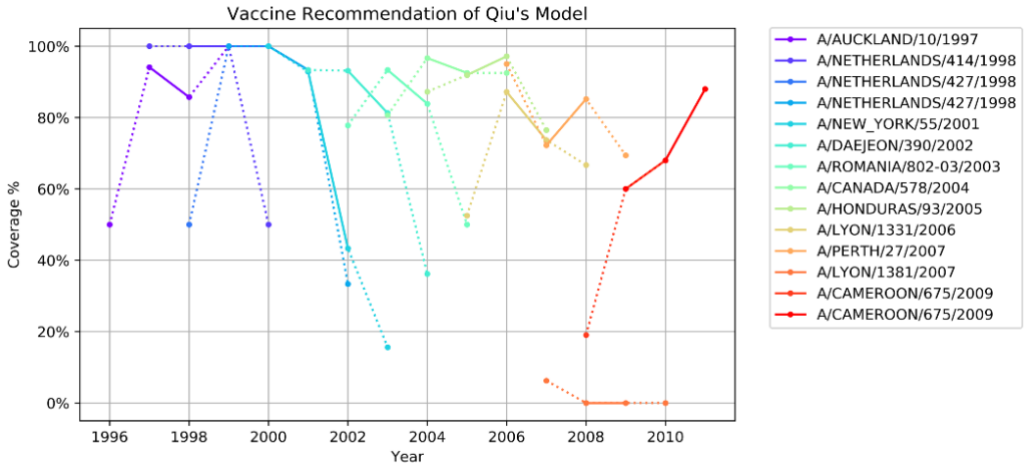

Figure 4.13 – Antigenicity coverage of vaccine recommendation by J Qiu's model.

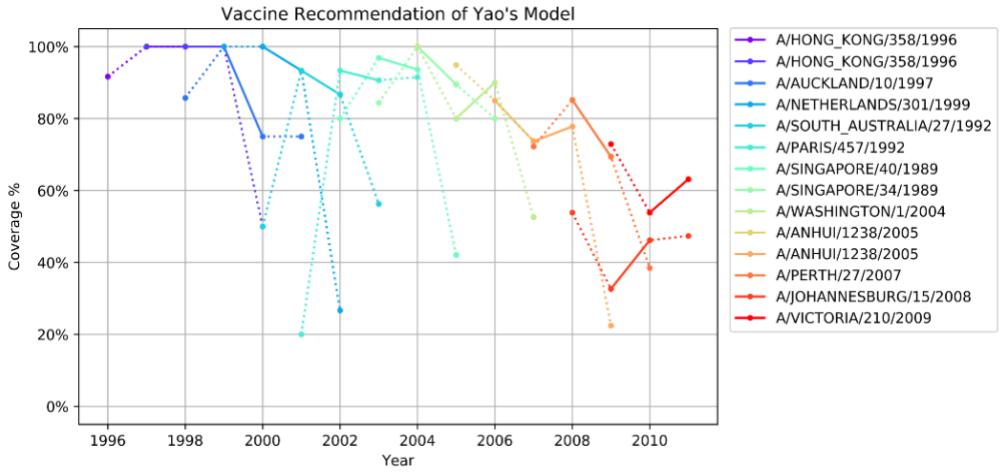

Figure 4.14 – Antigenicity coverage of vaccine recommendation by Y. Yao's model.

Table 4.9 – Summary of model coverage.

Model	Mean coverage	Median coverage	Standard deviation
Optimized recommendation	92.80%	95.89%	0.088

WHO recommendation	59.43%	74.07%	0.335
Liao's	82.19%	81.32%	0.127
Qiu's	82.10%	92.98%	0.258
Yao's	85.28%	93.33%	0.194
CNN model	90.19%	97.19%	0.123

4.6 Discussion

Because of the continuous evolution of influenza viruses, vaccine recommendation remains a public health challenge. Due to the limitation of traditional hemagglutination inhibition assay, *in silico* prediction of antigenicity is cost-effective and has become more widely accepted. As many predictive models have been developed, this work is the first time that convolutional neural networks are applied in this realm. Compared to other predictive models, our CNN model outperformed all others in terms of accuracy, sensitivity and specificity. To validate the usefulness of antigenic cartography, we constructed augmented models using cartography (multidimensional scaling) and evaluated its performance. Our results show that the CNN model trained with antigenic cartography can further achieve better performance.

AAindex [231] is an excellent source for quantifying the property of protein sequences but have not been utilized comprehensively. Previous research primarily focused on limited properties of amino acids [194, 247], such as polarity and hydrophobicity. Y. Yao [18] performed a comprehensive analysis of AAindex 2 using random forest. In this study, we systematically analyzed the predictability of all three datasets provided by AAindex database and optimized their selection for our CNN model. In prior studies of antigenicity prediction, researchers tend to select amino acid properties primarily from AAindex1 [194, 247], such as hydrophobicity, and polarity. However, our regression model showed that AAindex 1 has relatively low predictability when compared to AAindex 2 and 3. The best validation MCC achieved by AAindex 1 is merely around 0. Combining AAindex 1 with AAindex 2 and 3 also reveals worse than mediocre predictive performance. Our findings suggest that it is reasonable to abandon the use of AAindex 1 for antigenicity prediction.

We have developed a pipeline for optimizing the selection of AAindex within a deep learning environment. Specifically, we adopted a non-gradient based optimization approach – particle swarm optimization algorithm – and use a small but carefully designed neural network to produce an objective function value (the solution corresponds to a set of good combinations of AAindex*)*. Multiple random starts of the optimization pipeline produced the best AAindex combinations with roughly half of the candidates from AAindex 2 and half from AAindex 3. The optimized combinations of AAindex elements prove to be not just a collection of individual elements with top performance in singular validation mentioned above. Rather, there is obvious combinatorial effect from several "weak" AAindex elements, which is captured in the convolutional neural network model.

In previous work [18], Y. Yao et al. proposed a stepwise method to select the AAindex elements, which initializes a pool of candidates by adding the best performed element sequentially. In contrast, our method starts with randomly selected elements multiple times, and thus avoid being potentially trapped in local minima.

The optimization of deep learning neural networks has been a major challenge for researchers, since it requires extensive empirical experiments. Although it benefits from experience, optimizing neural networks based on experience poses serious limits. Our proposed computational pipeline of a particle swarm optimization algorithm-based protocol to choose the best performed CNN structure allows flexibility in designing and testing different optimizers and tailoring algorithms to specific applications. Similarly, several random initializations were conducted when optimizing the selection of AAindex candidates. These steps ensure a diverse pool in generating the best performed CNN model.

A major significance of the *in silico* prediction of antigenicity is its application to vaccine recommendation and disease prevention. Vaccine recommendation remains a key challenge in combating seasonal influenza viruses and numerous predictive models have been investigated. In the 14 years 1998 – 2011 of antigenicity prediction (Table 4.8), our models achieved better MCC in validation set when compared to the state-of-the-art published approaches. The accurate prediction eventually facilitates better vaccine candidate selection and recommendation.

We also note the limitation on the analysis for the test set in the year of 2000, where the specificity was merely 0.506, indicating the difficulty in predicting this particular dataset. Historical archive has shown that the flu season of 2000-2001 is especially mild

and it was the first time since 1995 that H3N2 did not predominate [248]. The reason of the mild pandemic could be the lack of diverse variants and thus introducing difficulty in identifying distant mutants. Our model presents advantage even under such a difficult case where it still outperformed all other models.

We only performed year by year prediction up to 2011. The reason for not furthering our analysis for the year 2012 to 2016 is the sparsity of data and we judge that the lack of data will be a major obstacle for meaningful prediction.

Contrasting to other approaches (Figure 4.9, Figure 4.10, Figure 4.11, Figure 4.12, Figure 4.13, Figure 4.14, Table 4.9), the CNN vaccine recommendation offers better coverage during the period of being a recommended strain. It tends to suggest a different virus strain more frequently than the WHO recommendation and presents a much better antigenicity coverage. The analysis supports that our model learns rapidly and selects strains based on global knowledge, whereas human experts take longer time (and lower coverage) to guide them to a new strain.

Unlike other approaches where single mutation of amino acids are identified, our CNN model embeds their combinatorial relationship within a weighted matrix. One way to elucidate these relationships is to apply permutation to a specific position of the protein sequence across all samples and measure the change of performance.

Computationally, it takes approximately 30 minutes to an hour to train the convolutional neural networks, while the prediction is instant (merely seconds). This time expense estimate applies to all recommendations.

In summary, we demonstrated an innovative design and application of convolutional neural networks in the realm of influenza antigenicity prediction. We proposed and validated the pipeline of amino acids selection, AAindex selection, and structural optimization of neural networks for the theme of Influenza vaccine recommendation. Our systems approach learns rapidly and advances the development of vaccine with higher accuracy. The beneficial effect resides in both saving of time and economic expenses.

CHAPTER 5 CONCLUSIONS

In conclusion, this thesis dissertation is composed of three studies focused on providing decision modeling and analytical tools with the objective of protecting public health. The complexity of real-world issues and the growing scale of data have largely prohibited direct human interpretation. The advances in computation technique and methodology provides an alternative perspective of computation assisted decision making and problem modelling. This dissertation aims at tackling public health problems at three levels: 1) public activity, 2) medical care service, and 3) vaccine recommendation.

The first study introduces an agent-based simulation platform that serves as a decision support system for crowd management in public venues. Crowd management has been one of the center topics of operation research for decades, where equation-based model and discrete event simulation approaches have been the dominating methodology. Alternatively, the emergence of agent-based simulation provides a bottom-up perspective to tackle the crowd management problem in an emergent or non-emergent scenario. The second study applies a data-driven informatics and machine learning approach to quantify the outcome of practice variance of medical care providers. Machine learning approach has been gaining attention in health care research, such as MRI processing, EMR standardization, disease prediction and medicine optimization. The second study extend its application to explore the efficacy and side effects of an innovative needle-based technique in epidural anesthesia for parturient women and summarize the practice guideline regarding improvement of the procedure. The third study proposes the application of convolutional neural network in the prediction of antigenicity of influenza viruses (A/H3N2) and vaccine

recommendation. Mathematical modeling and machine learning have been used in antigenicity determination based on the genomic, phylogenetic and serological information of influenza viruses. Our model is benchmarked with three state-of-the-art machine learning models and proved to exhibit superior performance in multiple prediction metrics.

Researchers argue that all future computer simulation will be agent-based simulation because of the natural representation of real-life entity and the resemblance between agent and the predominant computational paradigm of objective-oriented programming [249]. Chapter 2 proposes a new implementation of agent-based simulation with improvement on four aspects: path planning, collision avoidance, emotion modeling and optimization with simulation. The deliverables of this study also include a complete simulation platform for researcher's use. In the study, we demonstrate that Flood Theta* path planning algorithm outperforms Basic Theta* in finding the optimal path. We introduce the mechanism of Deep Looking, Larger Neighbor Looking and Close-Child policy and discuss the reduction of path length upon implementation. Deep Looking and Larger Neighbor Looking achieve path length reduction by expanding the choices of children of vertex, thus an increase of computational time is unavoidable. We argue that a trade-off of path length and computational cost should be made according to the requirement of the simulation scenario and computational resources, when apply the two mechanisms. It is worth noting that Close-Child policy produces relatively small reduction in path length compared to the other two, but it also reduces computational cost. Therefore, Close-Child policy should be applied regardless of the simulation scenario. There have been a variety of collision avoidance models. This study aims at introducing a collision avoidance model that is computationally feasible with large scale scenario and preserves

realistic human avoidance behavior at the same time. The Projection Based Interactive Velocity Avoidance Model is inspired by the classic social force model, whereas the avoidance of dynamic and static obstacle is modified toward more realistic behaviors. The simulation engine also integrates emotion modelling and an optimization component.

Machine learning approach brings alternative perspectives to the traditional practice of medical care. Large scale information processing, algorithm-based treatment planning, universal access to top grade diagnostics are made possible by applying computational tools along the side of health care providers. Epidural anesthesia has been thoroughly studied and preferred in various operations over general anesthesia, due to its lower rate of adverse effects. However, it is necessary to place the technique under scrutiny for further improvement, given the continuous evolution of knowledge, practice and technology. Chapter 3 presents the study that investigates the safety and efficacy of a large-dose, needle-based epidural anesthesia technique for parturient women, using a data-driven informatics and machine learning approach. The needle-based technique differs from the traditional catheter-based approach in that the majority of the dosage of anesthetics is administered via the epidural needle. Our findings indicate that the needle-based technique is faster and more-dosage effective in achieving sensory level. Additionally, we conclude that the technique is safe for clinical use, which has similar complication rate compared to the traditional approach. Discriminant analysis via mixed integer program (DAMIP) is used as the classifier to predict the occurrence of hypotension. The comparison reveals that 85% accuracy of DAMIP outperform other classic machine learning algorithms, including random forest, naïve Bayes, etc. The trained model returns 27 predictive rules each achieving greater than 82% 10-fold cross-validation accuracy and greater than 85% blind

prediction accuracy for predicting hypotension and non-hypotension. Further, machine learning approach is applied to predict the sensory level and time to sensory level. Besides obtaining a predictive model, the relationships between important factors and outcome are quantified, which confirms the complexity in achieving successful practice of epidural anesthesia. The analysis on medicine shows that the most common medicine combinations achieve above average efficacy. However, our findings also support that fentanyl has limited effect and could be avoided in practice. The findings from this investigation facilitate delivery improvement and establish an improved clinical practice guideline for training and for dissemination of safe practice.

The effectiveness of seasonal influenza vaccine mainly depends on how well the vaccine strain represents the prevalent viruses that circulate in the community. Hemagglutinin inhibition assay is the standard method for antigenic characterization of influenza viruses in the process of vaccine development. However, the approach is time-consuming, mid-throughput and requires live virus strains. The rapid evolution of influenza has become a major challenge due to the limitation of the empirical approach. The seasonal change of antigenicity is mainly due to the change of protein structures of the viruses, which is essentially determined by the genomic information. Therefore, *in silico* antigenic characterization using genomic data becomes the natural choices to enhance early determination of prevalent strains and vaccine recommendations. To our best knowledge, the study in Chapter 4 is the first to incorporate deep learning model with determining the composition of the seasonal influenza vaccine. The study systematically explores the ways of representation of hemagglutinin (HA) besides using binary digit or character as widely applied in other researches. We demonstrate that representing hemagglutinin protein

sequences using amino acid mutation matrices and amino acid pairwise contact potentials [231] produce superior performance of antigenicity prediction. Additionally, we applied a heuristic optimization algorithm, particle swarm optimization (PSO), to optimize the selection of AAindex before the construction of the feature space of HA. Particle swarm optimization is appealing in the particular scenario where the convexity is unknown, and constraints are not strict. Similarly, we apply PSO to find the optimized structure of the convolutional neural network, which serves as our predictive model for antigenicity prediction. We benchmark the performance of our model against three state-of-the-art machine learning models in a series of prediction scenarios, simulating the processes of annual vaccine recommendations. Contrasting to other models, the CNN vaccine recommendation offers better antigenic coverage and tends to suggest a different virus strain more frequently than the WHO's recommendation, presenting a much better vaccine effectiveness.

To take one step further in the battle against seasonal influenza epidemics, it is necessary to predict the evolution of influenza viruses. M. Łuksza [250] proposed a fitness model that predicts the evolution of the viral population from one year to the next, considering adaptive epitope changes and deleterious mutations outside the epitopes. Research sharing the similar perspective has been gaining attention but is still understated. We believe that computational model using deep learning technique will play an increasingly important role in the topic. For example, variational autoencoder [251] has been introduced to quantify the evolutional effect of genetic variations in a generalized manner, which could be further applied to infer the fitness of newly emerged mutations. A

similar model dedicated to the analysis of influenza viruses will definitely advance the recommendation of vaccine strains and protection of public health.

APPENDIX A. SUPPLEMENTARY INFORMATION FOR CHAPTER 2

A.1 Supplementary Figures and Tables for Chapter 2

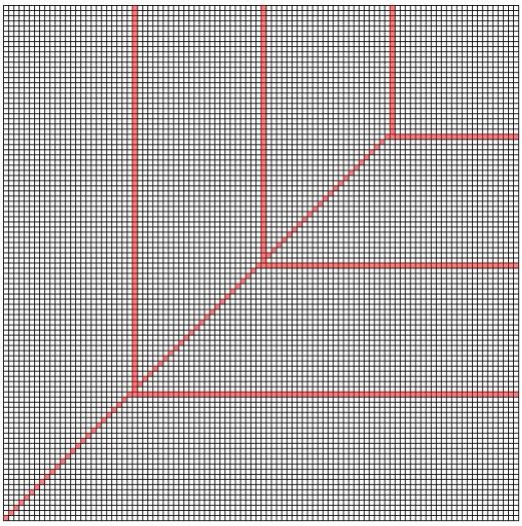

Figure A.1 – Paths of A* with 45-degree effect (100*100 map).

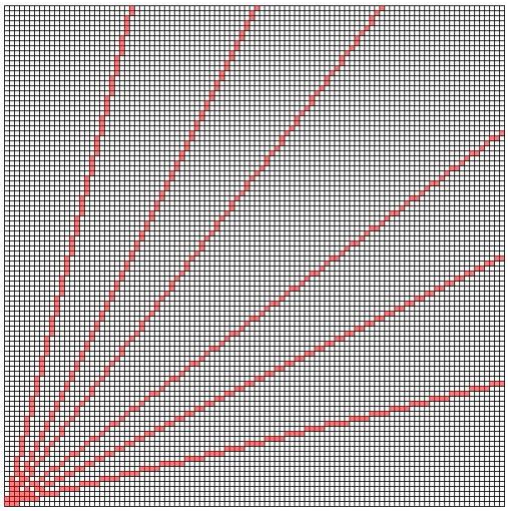

Figure A.2 – Flood Theta* path (100*100 map).

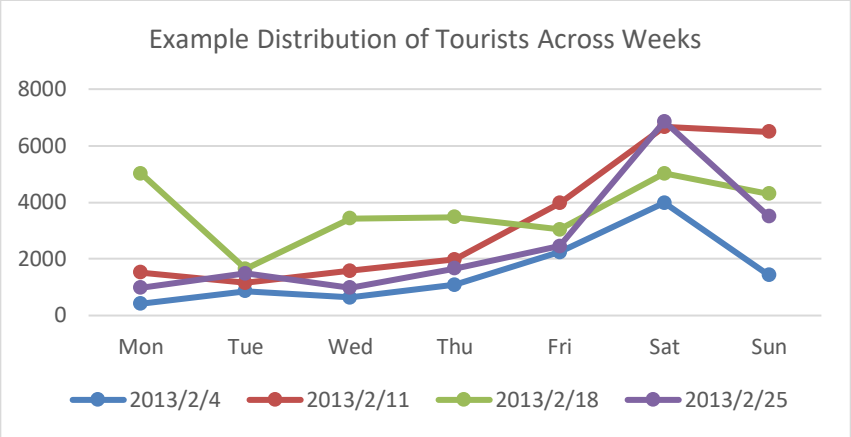

Figure A.3 – Distribution of Georgia Aquarium tourists in a week of February, 2013.

Table A.1 – Number of audiences admitted at gates of 7 games at Bobby Dodd Stadium.

Game	Gate 1	Gate 2	Gate 3	Gate 4	Gate 5	Gate 6	Gate 7	Gate 8	Gate 9	Gate 10	Total
Game 1	2349	708	798	5942	1375	486	5629	1089	2337	2355	23068
Game 2	2628	816	1440	7333	1782	176	6682	1523	2341	2676	27397
Game 3	2608	951	1550	8444	2808	32	8633	1355	3265	4278	33924
Game 4	1667	392	724	4831	1611	20	2907	1122	2619	1882	17775
Game 5	2141	482	788	6131	1469	186	3897	1743	1497	2136	20470
Game 6	2304	694	1557	7174	2688	403	6969	2303	2197	3747	30036
Game 7	2667	432	370	6466	2925	277	4748	1015	2736	2511	24147

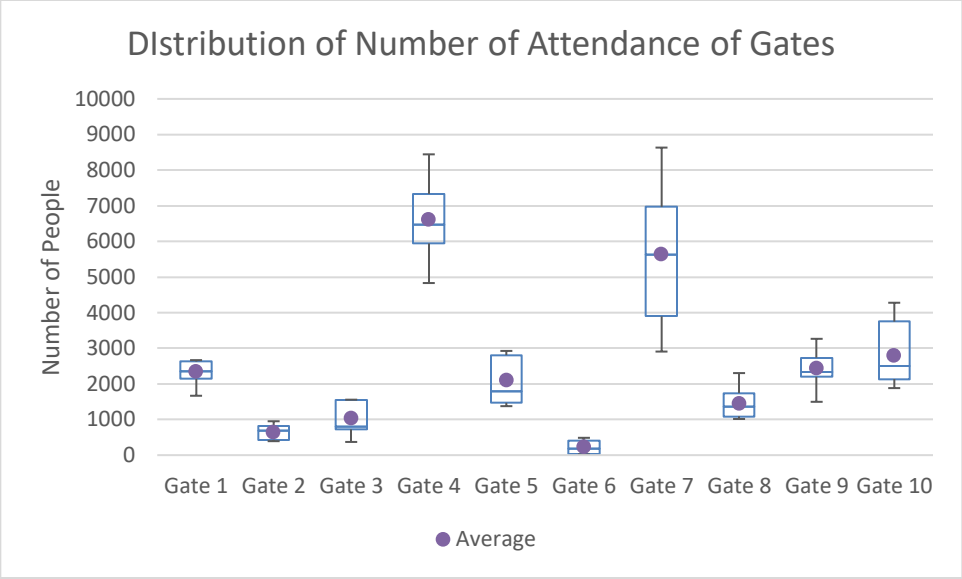

Figure A.4 – Distribution of attendance of all gates. Gate 4 and gate 7 handles the greatest number of guests, since they are convenient to reach from parking spaces.

Table A.2 – Averaged attendance of gates of Bobby Dodd Stadium.

	Gate 1	**Gate 2**	**Gate 3**	**Gate 4**	**Gate 5**
Average	2337.71	639.29	1032.43	6617.29	2094.00
Percentage	9.25%	2.53%	4.09%	26.20%	8.29%
	Gate 6	**Gate 7**	**Gate 8**	**Gate 9**	**Gate 10**
Average	225.71	5637.86	1450.00	2427.43	2797.86
Percentage	0.89%	22.32%	5.74%	9.61%	11.08%

Table A.3 – Fit and goodness of fit of arrival time to 5-degree polynomials.

	Polynomial coefficient					Goodness of fit		
Gate	p1	p2	p3	p4	p5	RMSE	R-square	Adjusted R-square
1	-0.0001106	0.02156	-1.288	30.03	-184.7	32.77	0.9848	0.9747
2	-1.96E-05	0.002978	-0.1137	1.394	20.21	20.7	0.8748	0.7746
3	-4.35E-05	0.00652	-0.2303	2.024	8.221	17.73	0.9822	0.968
4	-0.002175	0.3484	-18.27	373.5	-1970	364.8	0.8814	0.7232
5	-3.01E-05	0.002729	0.2073	-17.13	278.6	119.4	0.7427	0.5712
6	-1.85E-05	0.003607	-0.2411	6.573	-36.47	16.97	0.3241	-0.3517
7	-0.0005792	0.1003	-5.301	107.6	-655.2	142.7	0.9761	0.9521
8	-0.000486	0.05667	-2.163	38.04	-132	51.51	0.9656	0.8279
9	-0.0001728	0.03011	-1.516	25.42	-52.03	25.85	0.9932	0.9878
10	-5.03E-06	0.0007256	-0.02299	0.1979	3.271	12.07	0.511	0.4809

A.2 Additional Case Study in Use of the Agent-Based Simulation Platform

A.2.1 JFK Airport Evacuation

Agent-based simulation provides a unique approach to study emergency evacuation and assists in the design of logistical operations in an emergent scenario. Previous research has applied social force model [252] to simulate the panic behaviour in an evacuating crowd. Prolonged evacuation due to reduced visibility is well known to simulation researchers [253, 254]. Various implementations of agent-based simulation have revealed the factors in a successful evacuation, including emotions, location of hazard, facility configuration, placement of leaders, allocation of exits and exit route awareness of the crowd [254-257]. In our study, we propose using the optimization component to minimize the overall evacuation time in the JFK (John F. Kennedy) airport scenario.

The layout of JFK airport is obtained from public source and edited to highlight the boundaries of all terminals (Figure A.5). The simulation is initialized with a total of 10,000 passengers who evacuate from the all areas of the terminals to parking deck and roads outside the airport. Terminal 1, 2, 4, 5, 7, 8 evacuate 1000, 1000, 2000, 2000, 1000, 3000 passengers respectively, while the virtual passengers are assumed with various physical characteristics (Figure A.6).

In the minimization of evacuation time, 20 random initializations of the route selection are generated, followed by simulating using the initializations. A neural network is trained to fit the 20 cases to the objective value, which is the overall evacuation time of the whole facility. Sequential quadratic programming [258] is used to find the optimal variables with the training neural network serving as the objective function. Figure A.8

illustrates the contrast of the evacuation scenario with optimized route against random initialization, in which the optimized scenario evacuates all passengers 56 seconds faster than the average of the rest of cases.

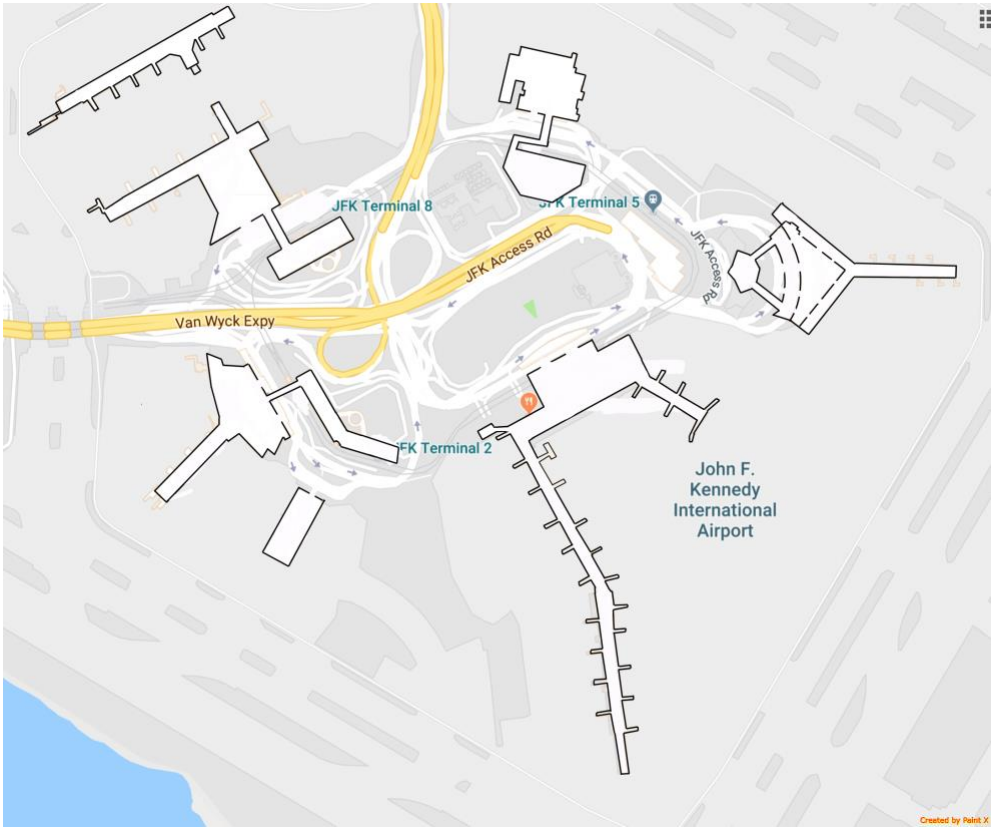

Figure A.5 – JFK evacuation simulation layout design.

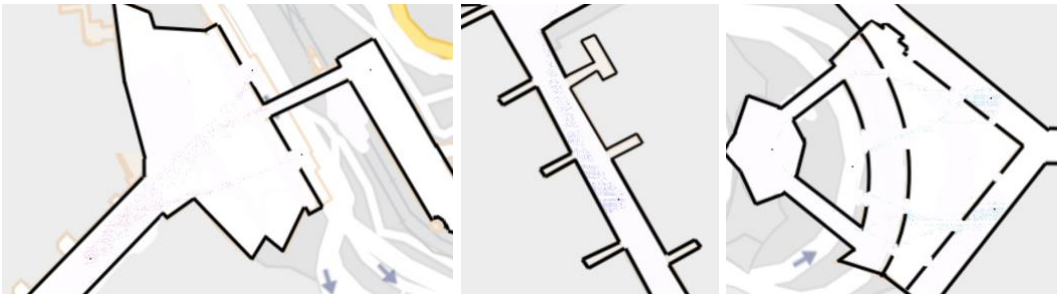

Figure A.6 – JFK terminal 1, 4 and 5 in evacuation.

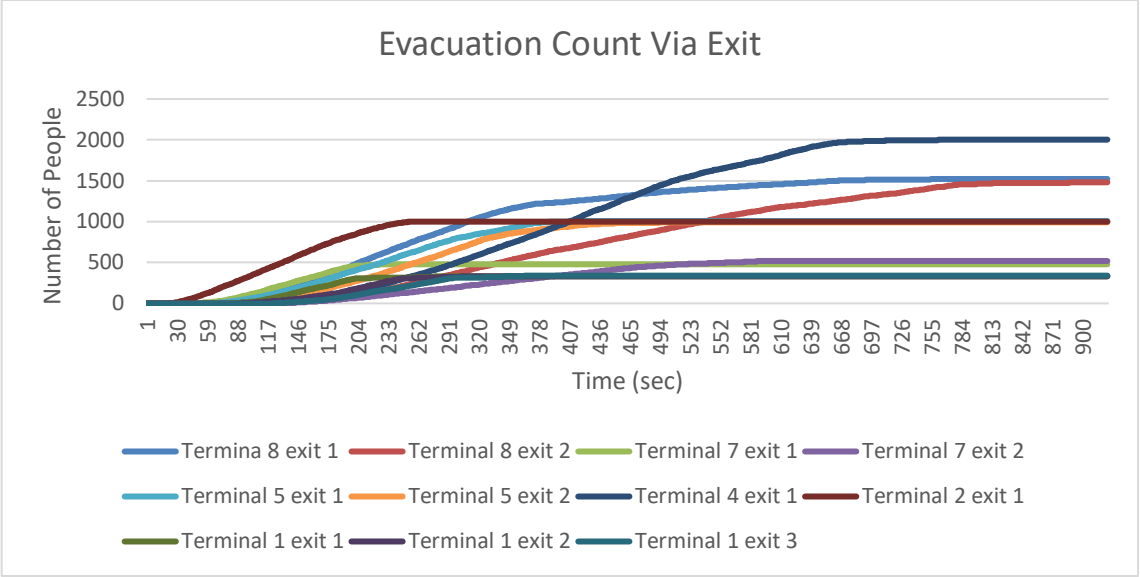

Figure A.7 – JFK evacuation progress for all exits.

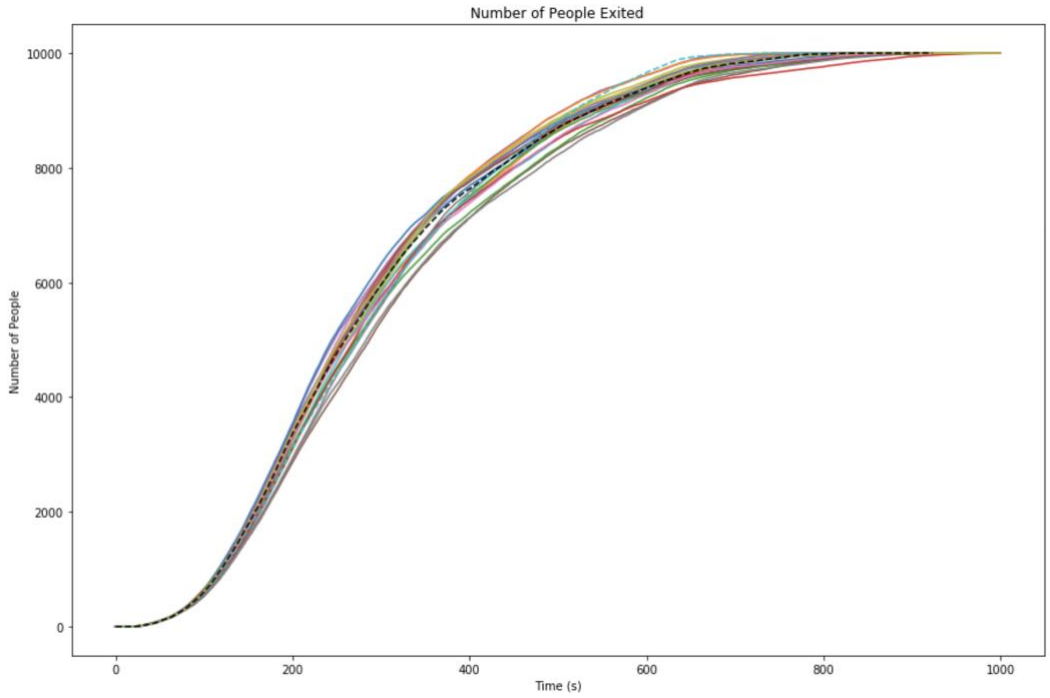

Figure A.8 – Optimization of evacuation time. Dashed cyan line represents the optimized scenario.

APPENDIX B. SUPPLEMENTARY INFORMATION FOR CHAPTER 3

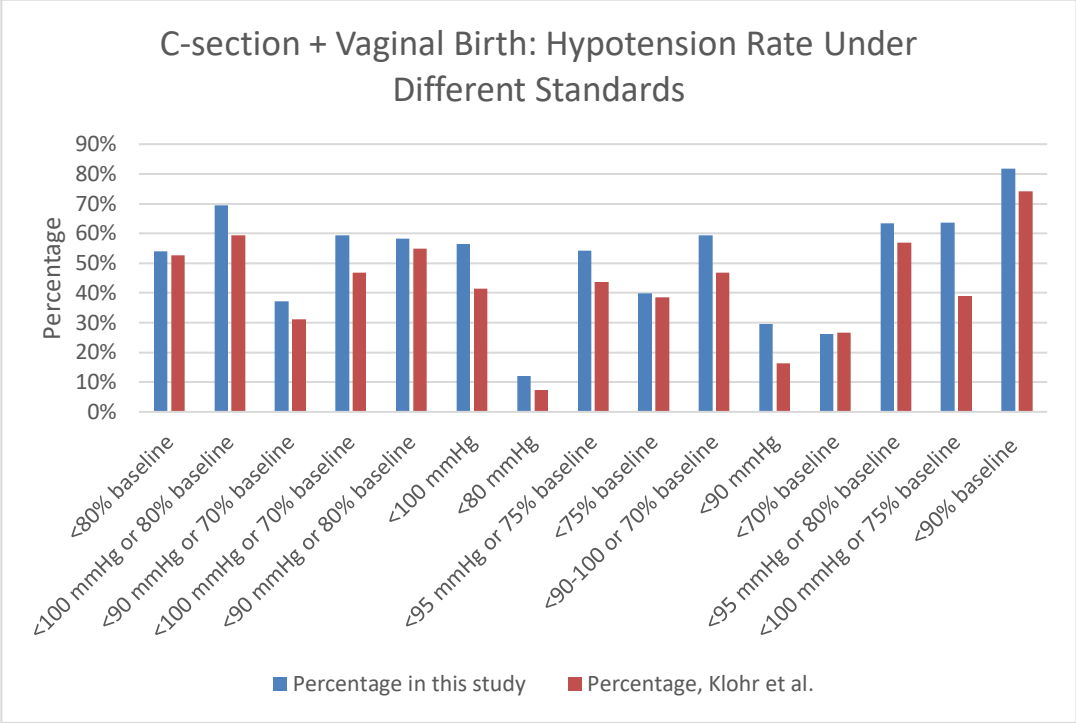

Figure B.1 – Contrast of hypotension occurrence rate with review study by Klöhr et al. [176].

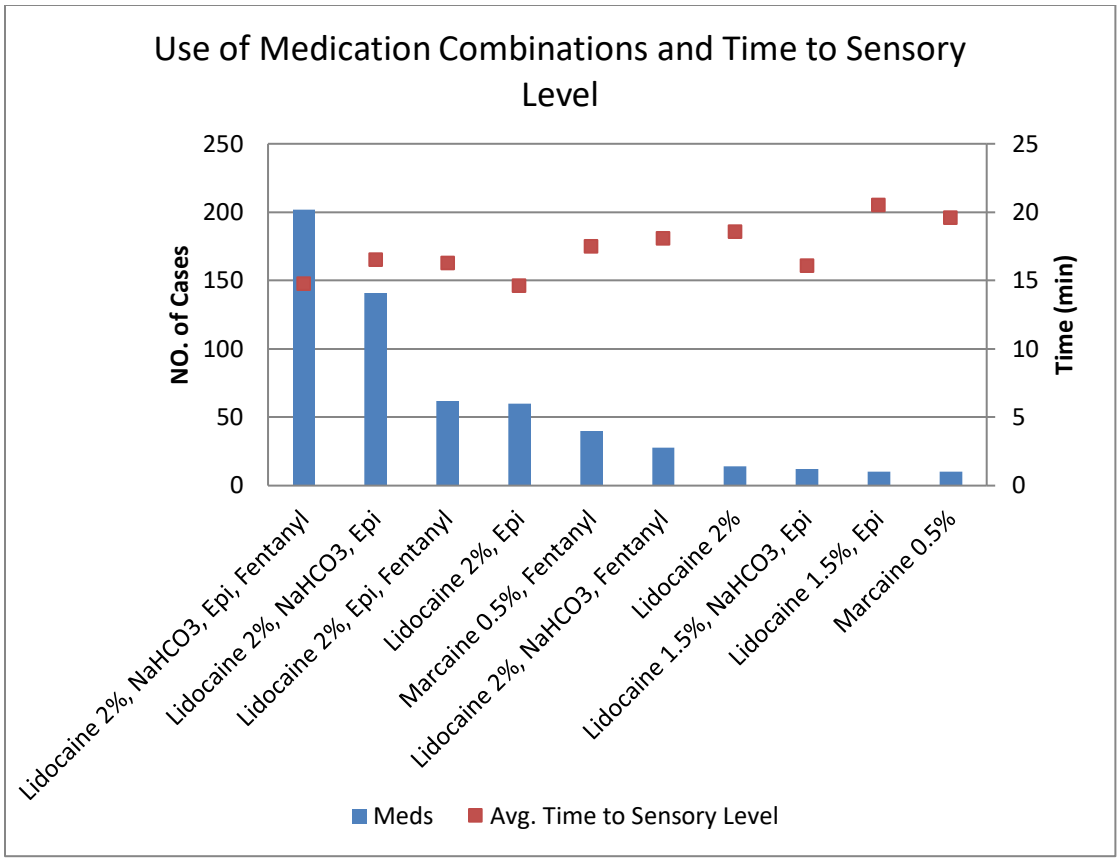

Figure B.2 – Preference of top 10 medicine combinations and average time to sensory level.

APPENDIX C. SUPPLEMENTARY INFORMATION FOR CHAPTER 4

Table C.1 – Implementation details of Y.C. Liao, J. Qiu, Y. Yao's and our CNN models.

Method	**Selection of Amino Acid**	**Scoring method**	**Data preprocessing**	**Predicative method**
Liao	None	Identity, Polarity, Aromaticity, PAM25, BLOSUM62		Linear regression, logistic regression, **SVM**
Qiu	By identifying antigenicity-dominant position	Position specific scoring matrix (PSSM), isoelectric point (ZIMJ680104), hydrophobicity, van der waals volume		Linear regression
Yao	Non-conserve ones	Stepwise optimization, from AAindex 2	MDS	Random forest
CNN	Conservation score, logistic regression and	Logistic regression and PSO, selection from AAindex 2, and 3		CNN

	mutual information score			
CNN with MDS	Conservation score, logistic regression and mutual information score	Logistic regression and PSO, selection from AAindex 2, and 3	MDS	CNN

Table C.2 – Data availability of sequential predictions.

Start year of training set	End year of training set	NO. of samples	Year of test set	NO. of samples
1968	1997	3148	1998	54
1968	1998	3202	1999	43
1968	1999	3245	2000	8
1968	2000	3253	2001	49
1968	2001	3302	2002	242
1968	2002	3544	2003	313
1968	2003	3857	2004	636
1968	2004	4493	2005	433
1968	2005	4926	2006	386
1968	2006	5312	2007	84

1968	2007	5396	2008	123
1968	2008	5519	2009	304
1968	2009	5823	2010	141

REFERENCES

[1] RAMSTEDT, L. and WOXENIUS, J. "Modelling approaches to operational decision-making in freight transport chains," in Proc. 18th NOFOMA Conference, 2006.

[2] STEENKEN, D., VOS, S. and STAHLBOCK, R., "Container terminal operation and operations research-a classification and literature review," OR spectrum, vol. 26(1): pp. 3-49, 2004.

[3] GÜNAL, M.M. and PIDD, M., "Discrete event simulation for performance modelling in health care: a review of the literature," Journal of Simulation, vol. 4(1): pp. 42-51, 2010.

[4] SIEBERS, P.-O., MACAL, C.M., GARNETT, J., BUXTON, D. and PIDD, M., "Discrete-event simulation is dead, long live agent-based simulation!," Journal of Simulation, vol. 4(3): pp. 204-210, 2010.

[5] PARVIN, J.D., MOSCONA, A., PAN, W., LEIDER, J. and PALESE, P., "Measurement of the mutation rates of animal viruses: influenza A virus and poliovirus type 1," Journal of virology, vol. 59(2): pp. 377-383, 1986.

[6] DRAKE, J.W. and HOLLAND, J.J., "Mutation rates among RNA viruses," Proceedings of the National Academy of Sciences, vol. 96(24): pp. 13910-13913, 1999.

[7] KAGEYAMA, T., FUJISAKI, S., TAKASHITA, E., XU, H., YAMADA, S., UCHIDA, Y., NEUMANN, G., SAITO, T., KAWAOKA, Y., et al., "Genetic analysis of novel avian A (H7N9) influenza viruses isolated from patients in China, February to April 2013," Euro surveill, vol. 18(15): pp. 7-21, 2013.

[8] MEHLE, A., DUGAN, V.G., TAUBENBERGER, J.K. and DOUDNA, J.A., "Reassortment and mutation of the avian influenza virus polymerase PA subunit overcome species barriers," Journal of virology, vol. 86(3): pp. 1750-1757, 2012.

[9] MCDONALD, S.M., NELSON, M.I., TURNER, P.E. and PATTON, J.T., "Reassortment in segmented RNA viruses: mechanisms and outcomes," Nature Reviews Microbiology, vol. 14(7): pp. 448-460, 2016.

[10] HOLMES, E.C., GHEDIN, E., MILLER, N., TAYLOR, J., BAO, Y., ST GEORGE, K., GRENFELL, B.T., SALZBERG, S.L., FRASER, C.M., et al., "Whole-genome analysis of human influenza A virus reveals multiple persistent lineages and reassortment among recent H3N2 viruses," PLoS biology, vol. 3(9): pp. e300, 2005.

[11] DE, A. and NANDY, A., "An insight to segment based genetic exchange in Influenza A virus: an in silico study," 2015.

[12] WHO. "Influenza (Seasonal)," 2016 [cited 2016 11]; Available from: http://www.who.int/mediacentre/factsheets/fs211/en/.

[13] BLACKBURNE, B.P., HAY, A.J. and GOLDSTEIN, R.A., "Changing selective pressure during antigenic changes in human influenza H3," PLoS Pathog, vol. 4(5): pp. e1000058, 2008.

[14] PENG, D., HU, S., HUA, Y., XIAO, Y., LI, Z., WANG, X. and BI, D., "Comparison of a new gold-immunochromatographic assay for the detection of antibodies against avian influenza virus with hemagglutination inhibition and agar gel immunodiffusion assays," Veterinary immunology and immunopathology, vol. 117(1): pp. 17-25, 2007.

[15] STEPHENSON, I., WOOD, J., NICHOLSON, K. and ZAMBON, M., "Sialic acid receptor specificity on erythrocytes affects detection of antibody to avian influenza haemagglutinin," Journal of medical virology, vol. 70(3): pp. 391-398, 2003.

[16] SUN, H., YANG, J., ZHANG, T., LONG, L.-P., JIA, K., YANG, G., WEBBY, R.J. and WAN, X.-F., "Using sequence data to infer the antigenicity of influenza virus," MBio, vol. 4(4): pp. e00230-13, 2013.

[17] REN, X., LI, Y., LIU, X., SHEN, X., GAO, W. and LI, J., "Computational identification of antigenicity-associated sites in the hemagglutinin protein of a/h1n1 seasonal influenza virus," PloS one, vol. 10(5): pp. e0126742, 2015.

[18] YAO, Y., LI, X., LIAO, B., HUANG, L., HE, P., WANG, F., YANG, J., SUN, H., ZHAO, Y., et al., "Predicting influenza antigenicity from Hemagglutintin sequence data based on a joint random forest method," Scientific Reports, vol. 7, 2017.

[19] LIAO, Y.-C., LEE, M.-S., KO, C.-Y. and HSIUNG, C.A., "Bioinformatics models for predicting antigenic variants of influenza A/H3N2 virus," Bioinformatics, vol. 24(4): pp. 505-512, 2008.

[20] PAN, K., SUBIETA, K.C. and DEEM, M.W., "A novel sequence-based antigenic distance measure for H1N1, with application to vaccine effectiveness and the selection of vaccine strains," Protein Engineering Design and Selection, vol. 24(3): pp. 291-299, 2011.

[21] STEINBRÜCK, L., KLINGEN, T. and MCHARDY, A., "Computational prediction of vaccine strains for human influenza A (H3N2) viruses," Journal of virology, vol. 88(20): pp. 12123-12132, 2014.

[22] AN, G., MI, Q., DUTTA‐MOSCATO, J. and VODOVOTZ, Y., "Agent‐based models in translational systems biology," Wiley Interdisciplinary Reviews: Systems Biology and Medicine, vol. 1(2): pp. 159-171, 2009.

[23] BONABEAU, E., "Agent-based modeling: Methods and techniques for simulating human systems," Proceedings of the national academy of sciences, vol. 99(suppl 3): pp. 7280-7287, 2002.

[24] GIMBLETT, H.R., "Integrating geographic information systems and agent-based modeling techniques for simulating social and ecological processes. 2002: Oxford University Press.

[25] RABERTO, M., CINCOTTI, S., FOCARDI, S.M. and MARCHESI, M., "Agent-based simulation of a financial market," Physica A: Statistical Mechanics and its Applications, vol. 299(1-2): pp. 319-327, 2001.

[26] MONOSTORI, L., VÁNCZA, J. and KUMARA, S.R., "Agent-based systems for manufacturing," CIRP annals, vol. 55(2): pp. 697-720, 2006.

[27] PAN, X., HAN, C.S., DAUBER, K. and LAW, K.H., "A multi-agent based framework for the simulation of human and social behaviors during emergency evacuations," Ai & Society, vol. 22(2): pp. 113-132, 2007.

[28] TAN, L., HU, M. and LIN, H., "Agent-based simulation of building evacuation: Combining human behavior with predictable spatial accessibility in a fire emergency," Information Sciences, vol. 295: pp. 53-66, 2015.

[29] SCHWARZ, N. and ERNST, A., "Agent-based modeling of the diffusion of environmental innovations—An empirical approach," Technological forecasting and social change, vol. 76(4): pp. 497-511, 2009.

[30] MAHAJAN, V., MULLER, E. and WIND, Y., "New-product diffusion models. Vol. 11. 2000: Springer Science & Business Media.

[31] SHAROMI, O. and MALIK, T., "Optimal control in epidemiology," Annals of Operations Research, vol. 251(1-2): pp. 55-71, 2017.

[32] RAHMANDAD, H. and STERMAN, J., "Heterogeneity and network structure in the dynamics of diffusion: Comparing agent-based and differential equation models," Management Science, vol. 54(5): pp. 998-1014, 2008.

[33] PARUNAK, H.V.D., SAVIT, R. and RIOLO, R.L. "Agent-based modeling vs. equation-based modeling: A case study and users' guide," in International Workshop on Multi-Agent Systems and Agent-Based Simulation: Springer, 1998.

[34] WONHAM, M.J., DE-CAMINO-BECK, T. and LEWIS, M.A., "An epidemiological model for West Nile virus: invasion analysis and control applications," Proceedings of the Royal Society of London. Series B: Biological Sciences, vol. 271(1538): pp. 501-507, 2004.

[35] PERKINS, T.A., SIRAJ, A.S., RUKTANONCHAI, C.W., KRAEMER, M.U. and TATEM, A.J., "Model-based projections of Zika virus infections in childbearing women in the Americas," Nature microbiology, vol. 1(9): pp. 16126, 2016.

[36] ALLEN, L.J., "Some discrete-time SI, SIR, and SIS epidemic models," Mathematical biosciences, vol. 124(1): pp. 83-105, 1994.

[37] KOROBEINIKOV, A. and MAINI, P.K., "A Lyapunov function and global properties for SIR and SEIR epidemiological models with nonlinear incidence," 2004.

[38] AMADOR, J., "The SEIQS stochastic epidemic model with external source of infection," Applied Mathematical Modelling, vol. 40(19-20): pp. 8352-8365, 2016.

[39] LIU, X. and YANG, L., "Stability analysis of an SEIQV epidemic model with saturated incidence rate," Nonlinear analysis: real world applications, vol. 13(6): pp. 2671-2679, 2012.

[40] KIM, K.I. and LIN, Z., "Asymptotic behavior of an SEI epidemic model with diffusion," Mathematical and Computer Modelling, vol. 47(11-12): pp. 1314-1322, 2008.

[41] KHOSROSHAHY, M., ALI, M.K.M. and QIU, D., "The SIC botnet lifecycle model: A step beyond traditional epidemiological models," Computer Networks, vol. 57(2): pp. 404-421, 2013.

[42] FISHMAN, G.S., "Discrete-event simulation: modeling, programming, and analysis. 2013: Springer Science & Business Media.

[43] ANGERHOFER, B.J. and ANGELIDES, M.C. "System dynamics modelling in supply chain management: research review," in Proceedings of the 32nd conference on Winter simulation: Society for Computer Simulation International, 2000.

[44] SUN, Y., LIU, N., SHANG, J. and ZHANG, J., "Sustainable utilization of water resources in China: A system dynamics model," Journal of cleaner production, vol. 142: pp. 613-625, 2017.

[45] RUBINSTEIN, R.Y. and KROESE, D.P., "Simulation and the Monte Carlo method. Vol. 10. 2016: John Wiley & Sons.

[46] CU, P.T. and BALL, J.E., "The influence of the calibration metric on design flood estimation using continuous simulation," International journal of river basin management, vol. 15(1): pp. 9-20, 2017.

[47] EKYALIMPA, R., WERNER, M., HAGUE, S., ABOURIZK, S. and PORTER, N. "A combined discrete-continuous simulation model for analyzing train-pedestrian interactions," in Proceedings of the 2016 Winter Simulation Conference: IEEE Press, 2016.

[48] MOON, Y.B., "Simulation modelling for sustainability: a review of the literature," International Journal of Sustainable Engineering, vol. 10(1): pp. 2-19, 2017.

[49] ONGGO, B.S.S., "An introduction to agent-based simulation as a decision-support tool," 2016.

[50] FANG, Z.-M., SONG, W.-G., ZHANG, J. and WU, H., "A multi-grid model for evacuation coupling with the effects of fire products," Fire Technology, vol. 48(1): pp. 91-104, 2012.

[51] SARMADY, S., HARON, F. and TALIB, A.Z. "Simulating crowd movements using fine grid cellular automata," in 2010 12th International Conference on Computer Modelling and Simulation: IEEE, 2010.

[52] GILLI, M. and WINKER, P., "A global optimization heuristic for estimating agent based models," Computational Statistics & Data Analysis, vol. 42(3): pp. 299-312, 2003.

[53] SCHÖNEBERG, J., ULLRICH, A. and NOÉ, F., "Simulation tools for particle-based reaction-diffusion dynamics in continuous space," BMC biophysics, vol. 7(1): pp. 11, 2014.

[54] OSTERMAN, M.J.K. and MARTIN, J.A., "Epidural and Spinal Anesthesia Use During Labor: 27-state Reporting Area, 2008." 2011, National Center for Health Statistics.

[55] HOLTE, K., FOSS, N.B., SVENSÉN, C., LUND, C., MADSEN, J.L. and KEHLET, H., "Epidural anesthesia, hypotension, and changes in intravascular volume," Anesthesiology: The Journal of the American Society of Anesthesiologists, vol. 100(2): pp. 281-286, 2004.

[56] MARDIROSOFF, C., DUMONT, L., BOULVAIN, M. and TRAMÈR, M.R., "Fetal bradycardia due to intrathecal opioids for labour analgesia: a systematic review," BJOG: an international journal of obstetrics & gynaecology, vol. 109(3): pp. 274-281, 2002.

[57] GOODMAN, B.S., POSECION, L.W., MALLEMPATI, S. and BAYAZITOGLU, M., "Complications and pitfalls of lumbar interlaminar and transforaminal epidural injections," Current reviews in musculoskeletal medicine, vol. 1(3-4): pp. 212, 2008.

[58] TORVALDSEN, S., ROBERTS, C.L., SIMPSON, J.M., THOMPSON, J.F. and ELLWOOD, D.A., "Intrapartum epidural analgesia and breastfeeding: a prospective cohort study," International Breastfeeding Journal, vol. 1(1): pp. 24, 2006.

[59] HALPERN, S.H., LEVINE, T., WILSON, D.B., MACDONELL, J., KATSIRIS, S.E. and LEIGHTON, B.L., "Effect of labor analgesia on breastfeeding success," Birth, vol. 26(2): pp. 83-88, 1999.

[60] WILSON, M., MACARTHUR, C., COOPER, G., BICK, D., MOORE, P., SHENNAN, A. and UK, C.S.G., "Epidural analgesia and breastfeeding: a randomised controlled trial of epidural techniques with and without fentanyl and a non‐epidural comparison group," Anaesthesia, vol. 65(2): pp. 145-153, 2010.

[61] HORLOCKER, T.T., WEDEL, D.J., BENZON, H. and BROWN, D.L., "Regional anesthesia in the anticoagulated patient: defining the risks," Regional anesthesia and pain medicine, vol. 29(2): pp. S1, 2004.

[62] APFELBAUM, J.L., HAWKINS, J.L., AGARKAR, M., BUCKLIN, B.A., CONNIS, R.T., GAMBLING, D.R., MHYRE, J., NICKINOVICH, D.G., SHERMAN, H., et al., "Practice Guidelines for Obstetric Anesthesia: An Updated Report by the American Society of Anesthesiologists Task Force on Obstetric Anesthesia and the Society for Obstetric Anesthesia and Perinatology∗," Anesthesiology, vol. 124(2): pp. 270-300, 2016.

[63] OBSTETRICIANS, A.C.O. and GYNECOLOGISTS, "ACOG Practice Bulletin. Clinical management guidelines for obstetrician-gynecologists. Number 32, November 2001 (replaces Technical Bulletin Number 181, June 1993, and Committee Opinion Number 241, September 2000). Thyroid disease in pregnancy," Obstetrics and gynecology, vol. 98(5 Pt 1): pp. 879, 2001.

[64] AGOR, J.K. and ÖZALTIN, O.Y., "Models for predicting the evolution of influenza to inform vaccine strain selection," Human vaccines & immunotherapeutics, vol. 14(3): pp. 678-683, 2018.

[65] BIERE, B., BAUER, B. and SCHWEIGER, B., "Differentiation of influenza B virus lineages Yamagata and Victoria by real-time PCR," Journal of clinical microbiology, vol. 48(4): pp. 1425-1427, 2010.

[66] AMBROSE, C.S. and LEVIN, M.J., "The rationale for quadrivalent influenza vaccines," Human vaccines & immunotherapeutics, vol. 8(1): pp. 81-88, 2012.

[67] BOTH, G.W., SLEIGH, M., COX, N. and KENDAL, A., "Antigenic drift in influenza virus H3 hemagglutinin from 1968 to 1980: multiple evolutionary pathways and sequential amino acid changes at key antigenic sites," Journal of virology, vol. 48(1): pp. 52-60, 1983.

[68] KOELLE, K., COBEY, S., GRENFELL, B. and PASCUAL, M., "Epochal evolution shapes the phylodynamics of interpandemic influenza A (H3N2) in humans," Science, vol. 314(5807): pp. 1898-1903, 2006.

[69] BONI, M.F., GOG, J.R., ANDREASEN, V. and CHRISTIANSEN, F.B., "Influenza drift and epidemic size: the race between generating and escaping immunity," Theoretical population biology, vol. 65(2): pp. 179-191, 2004.

[70] HAY, A.J., GREGORY, V., DOUGLAS, A.R. and LIN, Y.P., "The evolution of human influenza viruses," Philosophical Transactions of the Royal Society of London. Series B: Biological Sciences, vol. 356(1416): pp. 1861-1870, 2001.

[71] SCHWEIGER, B., BRUNS, L. and MEIXENBERGER, K., "Reassortment between human A (H3N2) viruses is an important evolutionary mechanism," Vaccine, vol. 24(44-46): pp. 6683-6690, 2006.

[72] CARRAT, F. and FLAHAULT, A., "Influenza vaccine: the challenge of antigenic drift," Vaccine, vol. 25(39-40): pp. 6852-6862, 2007.

[73] BARR, I.G., MCCAULEY, J., COX, N., DANIELS, R., ENGELHARDT, O.G., FUKUDA, K., GROHMANN, G., HAY, A., KELSO, A., et al., "Epidemiological, antigenic and genetic characteristics of seasonal influenza A (H1N1), A (H3N2) and B influenza viruses: basis for the WHO recommendation on the composition of influenza vaccines for use in the 2009–2010 Northern Hemisphere season," Vaccine, vol. 28(5): pp. 1156-1167, 2010.

[74] XIE, H., WAN, X.-F., YE, Z., PLANT, E.P., ZHAO, Y., XU, Y., LI, X., FINCH, C., ZHAO, N., et al., "H3N2 mismatch of 2014–15 northern hemisphere influenza vaccines and head-to-head comparison between human and ferret antisera derived antigenic maps," Scientific reports, vol. 5: pp. 15279, 2015.

[75] "CDC Seasonal Flu Vaccine Effectiveness Studies," 2019; Available from: https://www.cdc.gov/flu/vaccines-work/effectiveness-studies.htm?CDC_AA_refVal=https%3A%2F%2Fwww.cdc.gov%2Fflu%2Fprofessionals%2Fvaccination%2Feffectiveness-studies.htm.

[76] FUKUSHIMA, K., "Neocognitron: A self-organizing neural network model for a mechanism of pattern recognition unaffected by shift in position," Biological cybernetics, vol. 36(4): pp. 193-202, 1980.

[77] NAIR, V. and HINTON, G.E. "Rectified linear units improve restricted boltzmann machines," in Proceedings of the 27th international conference on machine learning (ICML-10), 2010.

[78] XU, B., WANG, N., CHEN, T. and LI, M., "Empirical evaluation of rectified activations in convolutional network," arXiv preprint arXiv:1505.00853, 2015.

[79] MARC'AURELIO RANZATO, F.-J.H., BOUREAU, Y.-L. and LECUN, Y. "Unsupervised learning of invariant feature hierarchies with applications to object recognition," in Proc. Computer Vision and Pattern Recognition Conference (CVPR'07). IEEE Press, 2007.

[80] YU, D., WANG, H., CHEN, P. and WEI, Z. “Mixed pooling for convolutional neural networks,” in International Conference on Rough Sets and Knowledge Technology: Springer, 2014.

[81] LAI, S., XU, L., LIU, K. and ZHAO, J. “Recurrent convolutional neural networks for text classification,” in Twenty-ninth AAAI conference on artificial intelligence, 2015.

[82] PU, Y., GAN, Z., HENAO, R., YUAN, X., LI, C., STEVENS, A. and CARIN, L. “Variational autoencoder for deep learning of images, labels and captions,” in Advances in neural information processing systems, 2016.

[83] CASTIGLIONE, F., “Agent based modeling,” Scholarpedia, vol. 1: pp. 1562, 2006.

[84] TADMOR, E., “A review of numerical methods for nonlinear partial differential equations,” Bulletin of the American Mathematical Society, vol. 49(4): pp. 507-554, 2012.

[85] LIU, F., ENANORIA, W.T., ZIPPRICH, J., BLUMBERG, S., HARRIMAN, K., ACKLEY, S.F., WHEATON, W.D., ALLPRESS, J.L. and PORCO, T.C., “The role of vaccination coverage, individual behaviors, and the public health response in the control of measles epidemics: an agent-based simulation for California,” BMC Public Health, vol. 15(1): pp. 447, 2015.

[86] MACAL, C.M., “Everything you need to know about agent-based modelling and simulation,” Journal of Simulation, vol. 10(2): pp. 144-156, 2016.

[87] FOLCIK, V.A., AN, G.C. and OROSZ, C.G., “The Basic Immune Simulator: an agent-based model to study the interactions between innate and adaptive immunity,” Theoretical Biology and Medical Modelling, vol. 4(1): pp. 39, 2007.

[88] CONWAY, S.R., “An agent-based model for analyzing control policies and the dynamic service-time performance of a capacity-constrained air traffic management facility,” 2006.

[89] BURSTEDDE, C., KLAUCK, K., SCHADSCHNEIDER, A. and ZITTARTZ, J., “Simulation of pedestrian dynamics using a two-dimensional cellular automaton,” Physica A: Statistical Mechanics and its Applications, vol. 295(3-4): pp. 507-525, 2001.

[90] BOTEA, A., BOUZY, B., BURO, M., BAUCKHAGE, C. and NAU, D. “Pathfinding in games,” Schloss Dagstuhl-Leibniz-Zentrum fuer Informatik, 2013.

[91] LI, H., TANG, W. and SIMPSON, D. “Behaviour based motion simulation for fire evacuation procedures,” in Proceedings Theory and Practice of Computer Graphics, 2004.: IEEE, 2004.

[92] CAZENAVE, T. “Optimizations of data structures, heuristics and algorithms for path-finding on maps,” in 2006 IEEE symposium on computational intelligence and games: IEEE, 2006.

[93] HARABOR, D. and BOTEA, A. “Breaking path symmetries on 4-connected grid maps,” in Sixth Artificial Intelligence and Interactive Digital Entertainment Conference, 2010.

[94] HARABOR, D.D. and GRASTIEN, A. “Online graph pruning for pathfinding on grid maps,” in Twenty-Fifth AAAI Conference on Artificial Intelligence, 2011.

[95] BOTEA, A., MÜLLER, M. and SCHAEFFER, J., “Near optimal hierarchical path-finding,” Journal of game development, vol. 1(1): pp. 7-28, 2004.

[96] HOOGENDOORN, S.P., BOVY, P.H. and DAAMEN, W., “Microscopic pedestrian wayfinding and dynamics modelling,” Pedestrian and evacuation dynamics, vol. 123: pp. 154,

[97] STUCKI, P. “Obstacles in pedestrian simulations,” in Diploma thesis, Swiss Federal Institute of Technology ETH: Citeseer, 2003.

[98] NASH, A., DANIEL, K., KOENIG, S. and FELNER, A. “Theta^*: Any-Angle Path Planning on Grids,” in AAAI, 2007.

[99] FERGUSON, D. and STENTZ, A., “Using interpolation to improve path planning: The Field D* algorithm,” Journal of Field Robotics, vol. 23(2): pp. 79-101, 2006.

[100] DANIEL, K., NASH, A., KOENIG, S. and FELNER, A., “Theta*: Any-angle path planning on grids,” Journal of Artificial Intelligence Research, vol. 39: pp. 533-579, 2010.

[101] THORPE, C. and MATTHIES, L. “Path relaxation: Path planning for a mobile robot,” in OCEANS 1984: IEEE, 1984.

[102] NASH, A., KOENIG, S. and LIKHACHEV, M. “Incremental Phi*: Incremental any-angle path planning on grids,” in Twenty-First International Joint Conference on Artificial Intelligence, 2009.

[103] REYNOLDS, C.W. “Steering behaviors for autonomous characters,” in Game developers conference, 1999.

[104] HEÏGEAS, L., LUCIANI, A., THOLLOT, J. and CASTAGNÉ, N., “A physically-based particle model of emergent crowd behaviors,” arXiv preprint arXiv:1005.4405, 2010.

[105] HELBING, D. and MOLNAR, P., “Social force model for pedestrian dynamics,” Physical review E, vol. 51(5): pp. 4282, 1995.

[106] ONDŘEJ, J., PETTRÉ, J., OLIVIER, A.-H. and DONIKIAN, S. "A synthetic-vision based steering approach for crowd simulation," in ACM Transactions on Graphics (TOG): ACM, 2010.

[107] VAN DEN BERG, J., LIN, M. and MANOCHA, D. "Reciprocal velocity obstacles for real-time multi-agent navigation," in Robotics and Automation, 2008. ICRA 2008. IEEE International Conference on: IEEE, 2008.

[108] VAN DEN BERG, J., GUY, S.J., LIN, M. and MANOCHA, D., *Reciprocal n-body collision avoidance*, in *Robotics research*. Springer. p. 3-19, 2011.

[109] SNAPE, J., VAN DEN BERG, J., GUY, S.J. and MANOCHA, D., "The hybrid reciprocal velocity obstacle*,"* IEEE Transactions on Robotics, vol. 27(4): pp. 696-706, 2011.

[110] PARIS, S., PETTRÉ, J. and DONIKIAN, S. "Pedestrian reactive navigation for crowd simulation: a predictive approach," in Computer Graphics Forum: Wiley Online Library, 2007.

[111] DUTRA, T., PRIEM, G., CAVALCANTE-NETO, J., VIDAL, C. and PETTRÉ, J. "Synthetic vision-based crowd simulation: reactive vs. reactive planning approaches," in Proceedings of the 27th Conference on Computer Animation and Social Agents (CASA 2014), 2014.

[112] GOLAS, A., NARAIN, R., CURTIS, S. and LIN, M.C., "Hybrid long-range collision avoidance for crowd simulation*,"* IEEE transactions on visualization and computer graphics, vol. 20(7): pp. 1022-1034, 2014.

[113] BORENSTEIN, J. and KOREN, Y., "The vector field histogram-fast obstacle avoidance for mobile robots*,"* IEEE transactions on robotics and automation, vol. 7(3): pp. 278-288, 1991.

[114] ULRICH, I. and BORENSTEIN, J. "VFH+: Reliable obstacle avoidance for fast mobile robots," in Proceedings. 1998 IEEE international conference on robotics and automation (Cat. No. 98CH36146): IEEE, 1998.

[115] FIORINI, P. and SHILLER, Z. "Motion planning in dynamic environments using the relative velocity paradigm," in [1993] Proceedings IEEE International Conference on Robotics and Automation: IEEE, 1993.

[116] CHAKRAVARTHY, A. and GHOSE, D., "Obstacle avoidance in a dynamic environment: A collision cone approach*,"* IEEE Transactions on Systems, Man, and Cybernetics-Part A: Systems and Humans, vol. 28(5): pp. 562-574, 1998.

[117] ABE, Y. and YOSHIKI, M. "Collision avoidance method for multiple autonomous mobile agents by implicit cooperation," in Proceedings 2001 IEEE/RSJ International Conference on Intelligent Robots and Systems. Expanding the

Societal Role of Robotics in the the Next Millennium (Cat. No. 01CH37180): IEEE, 2001.

[118] GUY, S.J., CHHUGANI, J., KIM, C., SATISH, N., LIN, M., MANOCHA, D. and DUBEY, P. "Clearpath: highly parallel collision avoidance for multi-agent simulation," in Proceedings of the 2009 ACM SIGGRAPH/Eurographics Symposium on Computer Animation: ACM, 2009.

[119] WILKIE, D., VAN DEN BERG, J. and MANOCHA, D. "Generalized velocity obstacles," in 2009 IEEE/RSJ International Conference on Intelligent Robots and Systems: IEEE, 2009.

[120] SNAPE, J., VAN DEN BERG, J., GUY, S.J. and MANOCHA, D. "Independent navigation of multiple mobile robots with hybrid reciprocal velocity obstacles," in 2009 IEEE/RSJ International Conference on Intelligent Robots and Systems: IEEE, 2009.

[121] LARGE, F., SCKHAVAT, S., SHILLER, Z. and LAUGIER, C. "Using non-linear velocity obstacles to plan motions in a dynamic environment," in 7th International Conference on Control, Automation, Robotics and Vision, 2002. ICARCV 2002.: IEEE, 2002.

[122] FULGENZI, C., SPALANZANI, A. and LAUGIER, C. "Dynamic obstacle avoidance in uncertain environment combining PVOs and occupancy grid," in Proceedings 2007 IEEE International Conference on Robotics and Automation: IEEE, 2007.

[123] HELBING, D., BUZNA, L., JOHANSSON, A. and WERNER, T., "Self-organized pedestrian crowd dynamics: Experiments, simulations, and design solutions," Transportation science, vol. 39(1): pp. 1-24, 2005.

[124] VERMUYTEN, H., BELIËN, J., DE BOECK, L., RENIERS, G. and WAUTERS, T., "A review of optimisation models for pedestrian evacuation and design problems," Safety science, vol. 87: pp. 167-178, 2016.

[125] SCHADSCHNEIDER, A., KLINGSCH, W., KLÜPFEL, H., KRETZ, T., ROGSCH, C. and SEYFRIED, A., *Evacuation dynamics: Empirical results, modeling and applications*, in *Encyclopedia of complexity and systems science*. Springer. p. 3142-3176, 2009.

[126] HELBING, D. and JOHANSSON, A., "Pedestrian, crowd and evacuation dynamics. 2009: Springer.

[127] HELBING, D., JOHANSSON, A. and AL-ABIDEEN, H.Z., "Dynamics of crowd disasters: An empirical study," Physical review E, vol. 75(4): pp. 046109, 2007.

[128] DURUPINAR, F., GÜDÜKBAY, U., AMAN, A. and BADLER, N.I., "Psychological parameters for crowd simulation: From audiences to mobs," IEEE

transactions on visualization and computer graphics, vol. 22(9): pp. 2145-2159, 2016.

[129] DURUPINAR, F., PELECHANO, N., ALLBECK, J., GUDUKBAY, U. and BADLER, N.I., "How the ocean personality model affects the perception of crowds," IEEE Computer Graphics and Applications, vol. 31(3): pp. 22-31, 2009.

[130] MEHRABIAN, A., "Pleasure-arousal-dominance: A general framework for describing and measuring individual differences in temperament," Current Psychology, vol. 14(4): pp. 261-292, 1996.

[131] MEHRABIAN, A., "Analysis of the big‐five personality factors in terms of the PAD temperament model," Australian journal of Psychology, vol. 48(2): pp. 86-92, 1996.

[132] FU, L., SONG, W., LV, W. and LO, S., "Simulation of emotional contagion using modified sir model: A cellular automaton approach," Physica A: Statistical Mechanics and its Applications, vol. 405: pp. 380-391, 2014.

[133] WANG, X., ZHANG, L., LIN, Y., ZHAO, Y. and HU, X., "Computational models and optimal control strategies for emotion contagion in the human population in emergencies," Knowledge-Based Systems, vol. 109: pp. 35-47, 2016.

[134] DING, A.W., "Implementing real-time grouping for fast egress in emergency," Safety Science, vol. 49(10): pp. 1404-1411, 2011.

[135] CEPOLINA, E.M., "Phased evacuation: An optimisation model which takes into account the capacity drop phenomenon in pedestrian flows," Fire Safety Journal, vol. 44(4): pp. 532-544, 2009.

[136] ABDELGHANY, A., ABDELGHANY, K., MAHMASSANI, H. and ALHALABI, W., "Modeling framework for optimal evacuation of large-scale crowded pedestrian facilities," European Journal of Operational Research, vol. 237(3): pp. 1105-1118, 2014.

[137] JOHANSSON, A. and HELBING, D., *Pedestrian flow optimization with a genetic algorithm based on boolean grids*, in *Pedestrian and evacuation dynamics 2005*. Springer. p. 267-272, 2007.

[138] TARKESH, H., ATIGHEHCHIAN, A. and NOOKABADI, A.S., "Facility layout design using virtual multi-agent system," Journal of Intelligent Manufacturing, vol. 20(4): pp. 347, 2009.

[139] SOLMAZ, G., AKBAŞ, M.İ. and TURGUT, D., "A mobility model of theme park visitors," IEEE Transactions on Mobile Computing, vol. 14(12): pp. 2406-2418, 2015.

[140] HUERRE, S. “Agent-based crowd simulation tool for theme park environments,” in Proc. 23rd Internat. Conf. Comput. Animation Soc. Agents, Saint-Malo, France, 2010.

[141] ZEESHAN-UL-HASSAN USMANI, F.A. and KIRK, D., “Intelligent agents in extreme conditions–modeling and simulation of suicide bombing for risk assessment,” Web Intelligence and Intelligent Agents: pp. 463, 2010.

[142] DUNHAM, C.M., HILEMAN, B.M., HUTCHINSON, A.E., CHANCE, E.A. and HUANG, G.S., “Perioperative hypoxemia is common with horizontal positioning during general anesthesia and is associated with major adverse outcomes: a retrospective study of consecutive patients,” BMC anesthesiology, vol. 14(1): pp. 43, 2014.

[143] CHENG, Q., ZHANG, J., WANG, H., ZHANG, R., YUE, Y. and LI, L., “Effect of Acute Hypercapnia on Outcomes and Predictive Risk Factors for Complications among Patients Receiving Bronchoscopic Interventions under General Anesthesia,” PloS one, vol. 10(7): pp. e0130771, 2015.

[144] LIU, S.S., STRODTBECK, W.M., RICHMAN, J.M. and WU, C.L., “A comparison of regional versus general anesthesia for ambulatory anesthesia: a meta-analysis of randomized controlled trials,” Anesthesia & Analgesia, vol. 101(6): pp. 1634-1642, 2005.

[145] OMOTE, K., NAMIKI, A. and IWASAKI, H., “Epidural administration and analgesic spread: comparison of injection with catheters and needles,” Journal of anesthesia, vol. 6(3): pp. 289-293, 1992.

[146] GAMBLING, D., BERKOWITZ, J., FARRELL, T.R., PUE, A. and SHAY, D., “A randomized controlled comparison of epidural analgesia and combined spinal-epidural analgesia in a private practice setting: pain scores during first and second stages of labor and at delivery,” Anesthesia & Analgesia, vol. 116(3): pp. 636-643, 2013.

[147] CESUR, M., ALICI, H.A., ERDEM, A.F., SILBIR, F. and YUKSEK, M.S., “Administration of local anesthetic through the epidural needle before catheter insertion improves the quality of anesthesia and reduces catheter-related complications,” Anesthesia & Analgesia, vol. 101(5): pp. 1501-1505, 2005.

[148] HUSAIN, F., HERMAN, N., KARUPARTHY, V., KNAPE, K. and DOWNING, J., “A comparison of catheter vs needle injection of local anesthetic for induction of epidural anesthesia for cesarean section,” International journal of obstetric anesthesia, vol. 6(2): pp. 101-106, 1997.

[149] YUN, M., YONG-CHUL, K., LIM, Y. and CHOI, G., “The differential flow of epidural local anaesthetic via needle or catheter: a prospective randomized double-blind study,” Anaesthesia and intensive care, vol. 32(3): pp. 377, 2004.

[150] RISTEV, G., SIPES, A.C., MAHONEY, B., LIPPS, J., CHAN, G. and COFFMAN, J.C., "Initiation of labor analgesia with injection of local anesthetic through the epidural needle compared to the catheter," Journal of pain research, vol. 10: pp. 2789, 2017.

[151] "MATLAB and Statistics Toolbox Release 2012b." 2012, The MathWorks, Inc: Natick, Massachusetts, United States.

[152] LEE, E.K., "Large-scale optimization-based classification models in medicine and biology," Annals of biomedical engineering, vol. 35(6): pp. 1095-1109, 2007.

[153] LEE, E.K., YUAN, F., HIRSH, D.A., MALLORY, M.D. and SIMON, H.K. "A clinical decision tool for predicting patient care characteristics: patients returning within 72 hours in the emergency department," in AMIA Annual Symposium Proceedings: American Medical Informatics Association, 2012.

[154] LEE, E.K., GALLAGHER, R.J. and PATTERSON, D.A., "A linear programming approach to discriminant analysis with a reserved-judgment region," INFORMS Journal on Computing, vol. 15(1): pp. 23-41, 2003.

[155] LEE, E.K. and WU, T.-L., *Classification and disease prediction via mathematical programming*, in *Handbook of optimization in medicine*. Springer. p. 1-50, 2009.

[156] LEE, E.K., *Machine learning framework for classification in medicine and biology*, in *Integration of AI and OR Techniques in Constraint Programming for Combinatorial Optimization Problems*. Springer. p. 1-7, 2009.

[157] BROOKS, J.P. and LEE, E.K., "Analysis of the consistency of a mixed integer programming-based multi-category constrained discriminant model," Annals of Operations Research, vol. 174(1): pp. 147-168, 2010.

[158] BROOKS, J.P. and LEE, E.K., "Solving a multigroup mixed-integer programming-based constrained discrimination model," INFORMS Journal on Computing, vol. 26(3): pp. 567-585, 2014.

[159] LEE, E.K., WU, T.-L., GOLDSTEIN, F. and LEVEY, A., *Predictive Model for Early Detection of Mild Cognitive Impairment and Alzheimer's Disease*, in *Optimization and Data Analysis in Biomedical Informatics*. Springer. p. 83-97, 2013.

[160] ECKER, J.L., CHEN, K.T., COHEN, A.P., RILEY, L.E. and LIEBERMAN, E.S., "Increased risk of cesarean delivery with advancing maternal age: indications and associated factors in nulliparous women," Am J Obstet Gynecol, vol. 185(4): pp. 883-7, 2001.

[161] ELEDJAM, J.J., RIPART, J. and VIEL, E., "Clinical application of ropivacaine for the lower extremity," Curr Top Med Chem, vol. 1(3): pp. 227-31, 2001.

[162] PAN, P., BOGARD, T. and OWEN, M., "Incidence and characteristics of failures in obstetric neuraxial analgesia and anesthesia: a retrospective analysis of 19,259 deliveries," International journal of obstetric anesthesia, vol. 13(4): pp. 227-233, 2004.

[163] PAECH, M., GODKIN, R. and WEBSTER, S., "Complications of obstetric epidural analgesia and anaesthesia: a prospective analysis of 10 995 cases," International Journal of Obstetric Anesthesia, vol. 7(1): pp. 5-11, 1998.

[164] EAPPEN, S., BLINN, A. and SEGAL, S., "Incidence of epidural catheter replacement in parturients: a retrospective chart review," Int J Obstet Anesth, vol. 7(4): pp. 220-5, 1998.

[165] CRAWFORD, J.S., "The second thousand epidural blocks in an obstetric hospital practice," Br J Anaesth, vol. 44(12): pp. 1277-87, 1972.

[166] THANGAMUTHU, A., RUSSELL, I.F. and PURVA, M., "Epidural failure rate using a standardised definition," International Journal of Obstetric Anesthesia, vol. 22(4): pp. 310-315, 2013.

[167] VALLEJO, M.C., PHELPS, A.L., SINGH, S., OREBAUGH, S.L. and SAH, N., "Ultrasound decreases the failed labor epidural rate in resident trainees," International Journal of Obstetric Anesthesia, vol. 19(4): pp. 373-378, 2010.

[168] NORRIS, M.C., GRIECO, W.M., BORKOWSKI, M., LEIGHTON, B.L., ARKOOSH, V.A., HUFFNAGLE, H.J. and HUFFNAGLE, S., "Complications of labor analgesia: epidural versus combined spinal epidural techniques," Anesth Analg, vol. 79(3): pp. 529-37, 1994.

[169] SPRIGGE, J. and HARPER, S., "Accidental dural puncture and post dural puncture headache in obstetric anaesthesia: presentation and management: A 23‐year survey in a district general hospital," Anaesthesia, vol. 63(1): pp. 36-43, 2008.

[170] VAN DE VELDE, M., SCHEPERS, R., BERENDS, N., VANDERMEERSCH, E. and DE BUCK, F., "Ten years of experience with accidental dural puncture and post-dural puncture headache in a tertiary obstetric anaesthesia department," International Journal of Obstetric Anesthesia, vol. 17(4): pp. 329-335, 2008.

[171] VERSTRAETE, S., WALTERS, M.A., DEVROE, S., ROOFTHOOFT, E. and VAN DE VELDE, M., "Lower incidence of post-dural puncture headache with spinal catheterization after accidental dural puncture in obstetric patients," Acta Anaesthesiologica Scandinavica, vol. 58(10): pp. 1233-1239, 2014.

[172] SADASHIVAIAH, J., WILSON, R., MCLURE, H. and LYONS, G., "Double-space combined spinal-epidural technique for elective caesarean section: a review of 10 years' experience in a UK teaching maternity unit," International Journal of Obstetric Anesthesia, vol. 19(2): pp. 183-187, 2010.

[173] JENKINS, J.G., "Some immediate serious complications of obstetric epidural analgesia and anaesthesia: a prospective study of 145 550 epidurals," International Journal of Obstetric Anesthesia, vol. 14(1): pp. 37-42, 2005.

[174] ROUT, C., AKOOJEE, S., ROCKE, D. and GOUWS, E., "Rapid administration of crystalloid preload does not decrease the incidence of hypotension after spinal anaesthesia for elective caesarean section," British Journal of Anaesthesia, vol. 68(4): pp. 394-397, 1992.

[175] CASCIO, M., PYGON, B., BERNETT, C. and RAMANATHAN, S., "Labour analgesia with intrathecal fentanyl decreases maternal stress," Can J Anaesth, vol. 44(6): pp. 605-9, 1997.

[176] KLÖHR, S., ROTH, R., HOFMANN, T., ROSSAINT, R. and HEESEN, M., "Definitions of hypotension after spinal anaesthesia for caesarean section: literature search and application to parturients," Acta anaesthesiologica Scandinavica, vol. 54(8): pp. 909-921, 2010.

[177] KOPACZ, D.J., SHARROCK, N.E. and ALLEN, H.W., "A comparison of levobupivacaine 0.125%, fentanyl 4 μg/mL, or their combination for patient-controlled epidural analgesia after major orthopedic surgery," Anesthesia & Analgesia, vol. 89(6): pp. 1497, 1999.

[178] CAMPBELL, D.C., ZWACK, R.M., CRONE, L.A. and YIP, R.W., "Ambulatory labor epidural analgesia: bupivacaine versus ropivacaine," Anesth Analg, vol. 90(6): pp. 1384-9, 2000.

[179] CAMPBELL, D.C., BANNER, R., CRONE, L.-A., GORE-HICKMAN, W. and YIP, R.W., "Addition of epinephrine to intrathecal bupivacaine and sufentanil for ambulatory labor analgesia," The Journal of the American Society of Anesthesiologists, vol. 86(3): pp. 525-531, 1997.

[180] MEISTER, G.C., D'ANGELO, R., OWEN, M., NELSON, K.E. and GAVER, R., "A comparison of epidural analgesia with 0.125% ropivacaine with fentanyl versus 0.125% bupivacaine with fentanyl during labor," Anesth Analg, vol. 90(3): pp. 632-7, 2000.

[181] SIA, A.T.H., CHONG, J.L., TAY, D.H.B., LO, W.K., CHEN, L.H. and CHIU, J.W., "Intrathecal sufentanil as the sole agent in combined spinal-epidural analgesia for the ambulatory parturient," Canadian journal of anaesthesia, vol. 45(7): pp. 620-625, 1998.

[182] BREEN, T.W., SHAPIRO, T., GLASS, B., FOSTER-PAYNE, D. and ORIOL, N.E., "Epidural anesthesia for labor in an ambulatory patient," Anesth Analg, vol. 77(5): pp. 919-24, 1993.

[183] MAAYAN-METZGER, A., SCHUSHAN-EISEN, I., TODRIS, L., ETCHIN, A. and KUINT, J., "Maternal hypotension during elective cesarean section and short-

term neonatal outcome," American journal of obstetrics and gynecology, vol. 202(1): pp. 56. e1-56. e5, 2010.

[184] WARD, R.J., BONICA, J.J., FREUND, F.G., AKAMATSU, T., DANZIGER, F. and ENGLESSON, S., "Epidural and subarachnoid anesthesia: cardiovascular and respiratory effects," Jama, vol. 191(4): pp. 275-278, 1965.

[185] LUNDBERG, S.M., ERION, G.G. and LEE, S.-I., "Consistent individualized feature attribution for tree ensembles," arXiv preprint arXiv:1802.03888, 2018.

[186] FRANK, S.G. and LALONDE, D.H., "How acidic is the lidocaine we are injecting, and how much bicarbonate should we add?," Canadian Journal of Plastic Surgery, vol. 20(2): pp. 71-73, 2012.

[187] HAMILTON, B.E., MARTIN, J.A., OSTERMAN, M.J.K., CURTIN, S.C. and MATHEWS, T.J., "Births: Final Data for 2014." 2015, National Center for Health Statistics.

[188] ATTANASIO, L., KOZHIMANNIL, K.B., JOU, J., MCPHERSON, M.E. and CAMANN, W., "Women's experiences with neuraxial labor analgesia in the listening to mothers II survey: a content analysis of open-ended responses," Anesthesia and analgesia, vol. 121(4): pp. 974, 2015.

[189] CHAN, C.-M., CHU, H., ZHANG, A.J., LEUNG, L.-H., SZE, K.-H., KAO, R.Y.-T., CHIK, K.K.-H., TO, K.K.-W., CHAN, J.F.-W., et al., "Hemagglutinin of influenza A virus binds specifically to cell surface nucleolin and plays a role in virus internalization," Virology, vol. 494: pp. 78-88, 2016.

[190] LEES, W.D., MOSS, D.S. and SHEPHERD, A.J., "A computational analysis of the antigenic properties of haemagglutinin in influenza A H3N2," Bioinformatics, vol. 26(11): pp. 1403-1408, 2010.

[191] LEE, M.-S., CHEN, M.-C., LIAO, Y.-C. and HSIUNG, C.A., "Identifying potential immunodominant positions and predicting antigenic variants of influenza A/H3N2 viruses," Vaccine, vol. 25(48): pp. 8133-8139, 2007.

[192] NEHER, R.A., BEDFORD, T., DANIELS, R.S., RUSSELL, C.A. and SHRAIMAN, B.I., "Prediction, dynamics, and visualization of antigenic phenotypes of seasonal influenza viruses," Proceedings of the National Academy of Sciences, vol. 113(12): pp. E1701-E1709, 2016.

[193] VELJKOVIC, V., PAESSLER, S., GLISIC, S., PRLJIC, J., PEROVIC, V.R., VELJKOVIC, N. and SCOTCH, M., "Evolution of 2014/15 H3N2 Influenza Viruses Circulating in US: Consequences for Vaccine Effectiveness and Possible New Pandemic," Frontiers in microbiology, vol. 6, 2015.

[194] QIU, J., QIU, T., YANG, Y., WU, D. and CAO, Z., "Incorporating structure context of HA protein to improve antigenicity calculation for influenza virus A/H3N2," Scientific Reports, vol. 6, 2016.

[195] WHO. "A Description of the Process of Seasonal and H5N1 Influenza

Vaccine Virus Selection and Development " 2007; Available from: http://www.who.int/influenza/resources/documents/influenza_vaccine-virus_selection/en/.

[196] KRIZHEVSKY, A., SUTSKEVER, I. and HINTON, G.E. "Imagenet classification with deep convolutional neural networks," in Advances in neural information processing systems, 2012.

[197] SIMARD, P.Y., STEINKRAUS, D. and PLATT, J.C. "Best practices for convolutional neural networks applied to visual document analysis," in ICDAR, 2003.

[198] KARPATHY, A., TODERICI, G., SHETTY, S., LEUNG, T., SUKTHANKAR, R. and FEI-FEI, L. "Large-scale video classification with convolutional neural networks," in Proceedings of the IEEE conference on Computer Vision and Pattern Recognition, 2014.

[199] JI, S., XU, W., YANG, M. and YU, K., "3D convolutional neural networks for human action recognition," IEEE transactions on pattern analysis and machine intelligence, vol. 35(1): pp. 221-231, 2013.

[200] KIM, Y., "Convolutional neural networks for sentence classification," arXiv preprint arXiv:1408.5882, 2014.

[201] ABDEL-HAMID, O., MOHAMED, A.-R., JIANG, H. and PENN, G. "Applying convolutional neural networks concepts to hybrid NN-HMM model for speech recognition," in Acoustics, Speech and Signal Processing (ICASSP), 2012 IEEE International Conference on: IEEE, 2012.

[202] WANG, T., WU, D.J., COATES, A. and NG, A.Y. "End-to-end text recognition with convolutional neural networks," in Pattern Recognition (ICPR), 2012 21st International Conference on: IEEE, 2012.

[203] CIREŞAN, D.C., GIUSTI, A., GAMBARDELLA, L.M. and SCHMIDHUBER, J. "Mitosis detection in breast cancer histology images with deep neural networks," in International Conference on Medical Image Computing and Computer-assisted Intervention: Springer, 2013.

[204] WANG, H., CRUZ-ROA, A., BASAVANHALLY, A., GILMORE, H., SHIH, N., FELDMAN, M., TOMASZEWSKI, J., GONZALEZ, F. and MADABHUSHI, A., "Mitosis detection in breast cancer pathology images by combining handcrafted

and convolutional neural network features," Journal of Medical Imaging, vol. 1(3): pp. 034003-034003, 2014.

[205] CRUZ-ROA, A., BASAVANHALLY, A., GONZÁLEZ, F., GILMORE, H., FELDMAN, M., GANESAN, S., SHIH, N., TOMASZEWSKI, J. and MADABHUSHI, A. "Automatic detection of invasive ductal carcinoma in whole slide images with convolutional neural networks," in SPIE medical imaging: International Society for Optics and Photonics, 2014.

[206] DOU, Q., CHEN, H., YU, L., ZHAO, L., QIN, J., WANG, D., MOK, V.C., SHI, L. and HENG, P.-A., "Automatic detection of cerebral microbleeds from MR images via 3D convolutional neural networks," IEEE transactions on medical imaging, vol. 35(5): pp. 1182-1195, 2016.

[207] GHAFOORIAN, M., KARSSEMEIJER, N., HESKES, T., VAN UDER, I., DE LEEUW, F.-E., MARCHIORI, E., VAN GINNEKEN, B. and PLATEL, B. "Non-uniform patch sampling with deep convolutional neural networks for white matter hyperintensity segmentation," in Biomedical Imaging (ISBI), 2016 IEEE 13th International Symposium on: IEEE, 2016.

[208] SARRAF, S. and TOFIGHI, G., "Classification of alzheimer's disease using fmri data and deep learning convolutional neural networks," arXiv preprint arXiv:1603.08631, 2016.

[209] QUANG, D. and XIE, X., "DanQ: a hybrid convolutional and recurrent deep neural network for quantifying the function of DNA sequences," Nucleic acids research, vol. 44(11): pp. e107-e107, 2016.

[210] KIM, J., "Detecting Influenza Outbreaks in United States by Analyzing Climatic Heat Maps Using Convolutional Neural Network,"

[211] ZHONG, S. and BIAN, L. "Predicting Influenza Dynamics using a Deep Learning Approach," in International Conference on GIScience Short Paper Proceedings, 2016.

[212] GARRO, B.A. and VÁZQUEZ, R.A., "Designing artificial neural networks using particle swarm optimization algorithms," Computational intelligence and neuroscience, vol. 2015: pp. 61, 2015.

[213] ZOPH, B. and LE, Q.V., "Neural architecture search with reinforcement learning," arXiv preprint arXiv:1611.01578, 2016.

[214] ALBELWI, S. and MAHMOOD, A., "A Framework for Designing the Architectures of Deep Convolutional Neural Networks," Entropy, vol. 19(6): pp. 242, 2017.

[215] BERGSTRA, J.S., BARDENET, R., BENGIO, Y. and KÉGL, B. "Algorithms for hyper-parameter optimization," in Advances in Neural Information Processing Systems, 2011.

[216] KARABOGA, D., AKAY, B. and OZTURK, C., "Artificial bee colony (ABC) optimization algorithm for training feed-forward neural networks," MDAI, vol. 7: pp. 318-319, 2007.

[217] BERGSTRA, J. and BENGIO, Y., "Random search for hyper-parameter optimization," Journal of Machine Learning Research, vol. 13(Feb): pp. 281-305, 2012.

[218] SNOEK, J., LAROCHELLE, H. and ADAMS, R.P. "Practical bayesian optimization of machine learning algorithms," in Advances in neural information processing systems, 2012.

[219] SAXENA, S. and VERBEEK, J. "Convolutional neural fabrics," in Advances in Neural Information Processing Systems, 2016.

[220] MENDOZA, H., KLEIN, A., FEURER, M., SPRINGENBERG, J.T. and HUTTER, F. "Towards automatically-tuned neural networks," in Workshop on Automatic Machine Learning, 2016.

[221] YAO, X., "Evolving artificial neural networks," Proceedings of the IEEE, vol. 87(9): pp. 1423-1447, 1999.

[222] YU, J., XI, L. and WANG, S., "An improved particle swarm optimization for evolving feedforward artificial neural networks," Neural Processing Letters, vol. 26(3): pp. 217-231, 2007.

[223] YOUNG, S.R., ROSE, D.C., KARNOWSKI, T.P., LIM, S.-H. and PATTON, R.M. "Optimizing deep learning hyper-parameters through an evolutionary algorithm," in Proceedings of the Workshop on Machine Learning in High-Performance Computing Environments: ACM, 2015.

[224] BEDFORD, T., SUCHARD, M.A., LEMEY, P., DUDAS, G., GREGORY, V., HAY, A.J., MCCAULEY, J.W., RUSSELL, C.A., SMITH, D.J., et al., "Integrating influenza antigenic dynamics with molecular evolution," Elife, vol. 3: pp. e01914, 2014.

[225] SMITH, D.J., LAPEDES, A.S., DE JONG, J.C., BESTEBROER, T.M., RIMMELZWAAN, G.F., OSTERHAUS, A.D. and FOUCHIER, R.A., "Mapping the antigenic and genetic evolution of influenza virus," science, vol. 305(5682): pp. 371-376, 2004.

[226] BAO, Y., BOLOTOV, P., DERNOVOY, D., KIRYUTIN, B., ZASLAVSKY, L., TATUSOVA, T., OSTELL, J. and LIPMAN, D., "The influenza virus resource at

the National Center for Biotechnology Information," Journal of virology, vol. 82(2): pp. 596-601, 2008.

[227] ZHANG, Y., AEVERMANN, B.D., ANDERSON, T.K., BURKE, D.F., DAUPHIN, G., GU, Z., HE, S., KUMAR, S., LARSEN, C.N., et al., "Influenza Research Database: An integrated bioinformatics resource for influenza virus research," Nucleic acids research, vol. 45(D1): pp. D466-D474, 2016.

[228] ELBE, S. and BUCKLAND‐MERRETT, G., "Data, disease and diplomacy: GISAID's innovative contribution to global health," Global Challenges, vol. 1(1): pp. 33-46, 2017.

[229] EDGAR, R.C., "MUSCLE: multiple sequence alignment with high accuracy and high throughput," Nucleic acids research, vol. 32(5): pp. 1792-1797, 2004.

[230] ASHKENAZY, H., EREZ, E., MARTZ, E., PUPKO, T. and BEN-TAL, N., "ConSurf 2010: calculating evolutionary conservation in sequence and structure of proteins and nucleic acids," Nucleic acids research, vol. 38(suppl_2): pp. W529-W533, 2010.

[231] KAWASHIMA, S., POKAROWSKI, P., POKAROWSKA, M., KOLINSKI, A., KATAYAMA, T. and KANEHISA, M., "AAindex: amino acid index database, progress report 2008," Nucleic acids research, vol. 36(suppl_1): pp. D202-D205, 2007.

[232] CHOLLET, FRANÇOIS and OTHERS. "Keras," 2015; Available from: https://github.com/fchollet/keras.

[233] LEE, E.K., NAKAYA, H.I., YUAN, F., QUEREC, T.D., BUREL, G., PIETZ, F.H., BENECKE, B.A. and PULENDRAN, B., "Machine learning for predicting vaccine immunogenicity," Interfaces, vol. 46(5): pp. 368-390, 2016.

[234] QUEREC, T.D., AKONDY, R.S., LEE, E.K., CAO, W., NAKAYA, H.I., TEUWEN, D., PIRANI, A., GERNERT, K., DENG, J., et al., "Systems biology approach predicts immunogenicity of the yellow fever vaccine in humans," Nature immunology, vol. 10(1): pp. 116, 2009.

[235] KENNEDY, J. and MENDES, R., "Neighborhood topologies in fully informed and best-of-neighborhood particle swarms," IEEE Transactions on Systems, Man, and Cybernetics, Part C (Applications and Reviews), vol. 36(4): pp. 515-519, 2006.

[236] KENNEDY, J., *Particle swarm optimization*, in *Encyclopedia of machine learning*. Springer. p. 760-766, 2011.

[237] DENNIS, J. and WOODS, D.J., "Optimization on microcomputers: The Nelder-Mead simplex algorithm," New computing environments: microcomputers in large-scale computing, vol. 11: pp. 116-122, 1987.

[238] POWELL, M.J., "An efficient method for finding the minimum of a function of several variables without calculating derivatives," The computer journal, vol. 7(2): pp. 155-162, 1964.

[239] STRAETER, T.A., "On the extension of the davidon-broyden class of rank one, quasi-newton minimization methods to an infinite dimensional hilbert space with applications to optimal control problems," 1971.

[240] FLETCHER, R., "Practical methods of optimization. 2013: John Wiley & Sons.

[241] BYRD, R.H., LU, P., NOCEDAL, J. and ZHU, C., "A limited memory algorithm for bound constrained optimization," SIAM Journal on Scientific Computing, vol. 16(5): pp. 1190-1208, 1995.

[242] MARTENS, J. "Deep learning via Hessian-free optimization," in ICML, 2010.

[243] CONN, A.R., SCHEINBERG, K. and TOINT, P.L., "On the convergence of derivative-free methods for unconstrained optimization," Approximation theory and optimization: tributes to MJD Powell: pp. 83-108, 1997.

[244] NOCEDAL, J. and WRIGHT, S.J., "Sequential quadratic programming. 2006: Springer.

[245] GEORGIEV, A.G., "Interpretable numerical descriptors of amino acid space," Journal of Computational Biology, vol. 16(5): pp. 703-723, 2009.

[246] VAN WESTEN, G.J., SWIER, R.F., CORTES-CIRIANO, I., WEGNER, J.K., OVERINGTON, J.P., IJZERMAN, A.P., VAN VLIJMEN, H.W. and BENDER, A., "Benchmarking of protein descriptor sets in proteochemometric modeling (part 2): modeling performance of 13 amino acid descriptor sets," Journal of cheminformatics, vol. 5(1): pp. 42, 2013.

[247] LEE, M.-S. and CHEN, J.S.-E., "Predicting antigenic variants of influenza A/H3N2 viruses," Emerging infectious diseases, vol. 10(8): pp. 1385, 2004.

[248] CDC. "2000-2001 INFLUENZA SEASON SUMMARY," 2001; Available from: https://www.cdc.gov/flu/weekly/weeklyarchives2000-2001/00-01summary.htm.

[249] NORTH, M.J. and MACAL, C.M., "Managing business complexity: discovering strategic solutions with agent-based modeling and simulation. 2007: Oxford University Press.

[250] ŁUKSZA, M. and LÄSSIG, M., "A predictive fitness model for influenza," Nature, vol. 507(7490): pp. 57, 2014.

[251] RIESSELMAN, A.J., INGRAHAM, J.B. and MARKS, D.S., "Deep generative models of genetic variation capture the effects of mutations," Nat. Methods, vol. 15: pp. 816-822, 2018.

[252] HELBING, D., FARKAS, I. and VICSEK, T., "Simulating dynamical features of escape panic," Nature, vol. 407(6803): pp. 487, 2000.

[253] YUAN, W. and TAN, K.H., "Cellular automata model for simulation of effect of guiders and visibility range," Current Applied Physics, vol. 9(5): pp. 1014-1023, 2009.

[254] HOU, L., LIU, J.-G., PAN, X. and WANG, B.-H., "A social force evacuation model with the leadership effect," Physica A: Statistical Mechanics and its Applications, vol. 400: pp. 93-99, 2014.

[255] ZHENG, Y., JIA, B., LI, X.-G. and ZHU, N., "Evacuation dynamics with fire spreading based on cellular automaton," Physica A: Statistical Mechanics and its Applications, vol. 390(18-19): pp. 3147-3156, 2011.

[256] MA, Y., YUEN, R.K.K. and LEE, E.W.M., "Effective leadership for crowd evacuation," Physica A: Statistical Mechanics and its Applications, vol. 450: pp. 333-341, 2016.

[257] WANG, J., ZHANG, L., SHI, Q., YANG, P. and HU, X., "Modeling and simulating for congestion pedestrian evacuation with panic," Physica A: Statistical Mechanics and its Applications, vol. 428: pp. 396-409, 2015.

[258] LAWRENCE, C.T. and TITS, A.L., "A computationally efficient feasible sequential quadratic programming algorithm," Siam Journal on optimization, vol. 11(4): pp. 1092-1118, 2001.